Realization and optimization of plasmonic structures for directional control of light

Quanbo Jiang

▶ **To cite this version:**

Quanbo Jiang. Realization and optimization of plasmonic structures for directional control of light. Other [cond-mat.other]. Université Grenoble Alpes, 2016. English. NNT : 2016GREAY086 . tel-01693753

HAL Id: tel-01693753
https://theses.hal.science/tel-01693753

Submitted on 26 Jan 2018

HAL is a multi-disciplinary open access archive for the deposit and dissemination of scientific research documents, whether they are published or not. The documents may come from teaching and research institutions in France or abroad, or from public or private research centers.

L'archive ouverte pluridisciplinaire **HAL**, est destinée au dépôt et à la diffusion de documents scientifiques de niveau recherche, publiés ou non, émanant des établissements d'enseignement et de recherche français ou étrangers, des laboratoires publics ou privés.

Communauté
UNIVERSITÉ Grenoble Alpes

THÈSE

Pour obtenir le grade de

DOCTEUR DE LA COMMUNAUTE UNIVERSITE GRENOBLE ALPES

Spécialité : **PHYSIQUE / PHYSIQUE DE MATIERE CONDENSEE & RAYONNEMENT**

Arrêté ministériel : 7 août 2006

Présentée par

Quanbo JIANG 姜全博

Thèse dirigée par **Aurélien DREZET** et
co-dirigée par **Joël BELLESSA**

préparée au sein de l'**Institut Néel (CNRS)**
dans **l'École Doctorale de Physique de Grenoble**

Réalisation et optimisation de structures plasmoniques pour le couplage directionnel de la lumière

Thèse soutenue publiquement le **jeudi 8 décembre 2016**,
devant le jury composé de :

Pr. Patricia SEGONDS
Professeur, Institut Néel, Président du jury
Pr. Elizabeth BOER-DUCHEMIN
Professeur, Institut des Sciences Moléculaires d'Orsay, Rapporteur
Dr. Nicolas BONOD
Chargé de recherche, Institut Fresnel, Rapporteur
Pr. Gerard COLAS DES FRANCS
Professeur, Laboratoire interdisciplinaire Carnot de Bourgogne, Examinateur
Dr. Cyriaque GENET
Directeur de recherche, Institut de Science et d'Ingénierie Supramoleculaire, Examinateur
Dr. Aurélien DREZET
Chargé de recherche, Institut Néel, Directeur de thèse
Pr. Joël BELLESSA
Professeur, Institut Lumière Matière, Co-directeur de thèse

To my family: my parents, grandparents

and

my girlfriend

知之真切笃实处即是行, 行之明觉精察处即是知。知行功夫, 本不可离。

—— 王阳明

Ce qui est le plus pitoyable pour l'homme, c'est de ne pas avoir la connaissance et de ne pas pouvoir se contraindre.

—— Michel Eyquem de Montaigne

Acknowledgements

First and foremost, I would like to express my sincere gratitude to my two advisors, Dr. Aurélien Drezet and Prof. Joël Bellessa for their continuous support of my PhD study and related research, for their patience, motivation, and immense knowledge. Aurélien, now the team leader of the Nano-Optics and Force (NOF) group at Institute Néel in Grenoble, inspires me by his passion, kindness and patience throughout my three-year study. I still remember the first time we met during the interview. After the long discussion, he decided to bring me in this project and showed the confidence on me. During my Ph.D work, he offered me help both in routine life and in scientific issue. His guidance helped me all the time on my research and writing of this thesis. I could not have imagined having a better advisor for my Ph.D study. Joël, the head of the Material and Nanostructures for Optics group at Institute Light and Matter (ILM) in Lyon, affects me by his conscientious attitude to academic research. I am lucky to have practiced my final internship of bachelor in his group 7 years ago. Thanks to this internship, the topic plasmonics came to my mind and attracted me all the time. When he told me that he had a Ph.D open position co-advised by Aurélien, I decided to take it even without any hesitation after my two-year master study at EPFL. During the days with collaboration in his group, I received his support all the time from renting the apartment to aligning the experimental setup. I really enjoy working with him and could not have imagined having a better co-advisor for my Ph.D study.

Besides my two advisors, I would like to thank the rest of my thesis committee: Prof. Elizabeth Boer-Duchemin, Dr. Nicolas Bonod, who accepted as the reporters of my thesis, Prof. Patricia Segonds, who accepted as the president of my jury, Prof. Gerard Colas des Francs and Dr. Cyriaque Genet, who accepted as the committees of my jury, not only for their insightful comments and encouragement, but also for their constructive questions during my defense which incented me to widen my research from various perspectives.

My sincere thanks also goes to Dr. Serge Huant, who is the director of our department PLUM. When I came to Grenoble for the interview, he picked me up from the train station and showed me the dynamic city and the marvelous institute. During the following three years, his kindness is always around me and brings me a feeling of home. Many thanks also extend to the other colleagues in our NOF group. They are Dr. Guillaume Bachelier,

who provided me every valuable help either for experiments or for suggestions on my slides for my public defense, Dr. Martin Berthel, who gave me all the possible help during his Ph.D study in our group, Aline Pham, who supported me a lot for working both on the experimental and paper work, Nicolas Chauvet, Maeliss Ethis de Corny, Guillaume Laurent, who are the Ph.D students in our group, and so forth. Although I can not list everyone in our group, I will remember all of you. Without you, my research would go slowly and lonely.

Moreover, I wish to express my special appreciation to Jean-Francois Motte and Gwénaëlle Julie. They provided me lots of precious supports on the sample fabrication. With their skillful help on Focused Ion Beam (FIB) and E-Beam Lithography (EBL), I managed to develop over 15 batches of samples during the three years. Even though we had to work until very late sometimes, to be honest, I really enjoy the time working with them in the clean room.

I thank my fellow office-mates for the stimulating discussions, for the sleepless nights at which we were working together before deadlines, and for all the fun we have had in the last three years. Also, I thank my friends met in the institute Néel and in Grenoble. In particular, I am grateful to all the people in our football team for winning the internal football tournament of our institute. I never forget how tough the final match was and how excited we were after this match. Thanks to all of you, my life was filled with colorful memory.

Last but not the least, I would like to thank my family: my parents, grandparents, uncle, aunt and my girlfriend for supporting me spiritually throughout writing this thesis and my life in general. Without them, I am not sure whether I could finish this tough project.

Of course, I also gratefully acknowledge the funding sources ARC 6 (Technologies de l'Information et de la Communication et Usages Informatiques Innovants) from the region Rhône-Alpes that made my Ph.D work possible.

My thesis is dedicated to Yannick Sonnefraud, who gave me the initial inspiration for the structures of nanoantennas. Even though he has passed away, we will keep his work continued.

Abstract

In this project, two contributions are reported. Firstly, the directional and singular generation of Surface Plasmon Polaritons (SPPs) in the nanoapertures is investigated using the Leakage Radiation Microscopy (LRM). We demonstrate experimentally spin-driven directional coupling as well as singularity (inward) and vortex (outward radial coupling) of SPPs by nanostructures built with T-shaped and Λ-shaped apertures. To support our experimental findings, we develop an analytical model based on a multidipolar representation of Λ- and T-shaped plasmonic couplers, allowing a theoretical explanation of both directionality and singular SPP formation. The optimal apex angle of Λ-shaped apertures shows the possibility to maximize the directiviy and extinction ratio for both directional coupling and singular SPP generation in the far field. Besides, our method based on LRM detection, allows quantitative analysis and is proven to be a sophisticated characterization technique for mapping the SPP vortex field. It provides several new possibilities for polarization-controlled SPP sub-wavelength focusing.

Secondly, the spin-orbit coupling of light into a photonic waveguide and its reciprocal effect are realized and confirmed both experimentally and theoretically. Coupler and decoupler gratings on the waveguide are firstly developed and investigated. The radiation of the guided light from the decoupler provides us a possibility to detect the confined waves. The fluorescence of nanocrystals deposited on the sample surface shows another possibility to directly visualize the light propagation in the waveguide. The spin-driven directional coupling of guided modes is achieved by Λ-shaped antennas and is certified by the dark field images with decouplers and the fluorescence images. Furthermore, the reverse effect is observed with an imperfection of output polarization which is explained that the diffraction orders by the Λ-shaped apertures influence the final polarization states based on an analytical model. By selecting the specific diffraction region on the Fourier plane, the reciprocal effect is realized. We believe that the quantitative characterization of spin-orbit interactions will pave the way for developing new directional couplers in the field of nanophotonics such as quantum information processing and so forth.

Key words: Surface plasmon polaritons, Leakage radiation microscopy, Spin-controlled directional coupling, Optical singularity and vortex, Waveguide couplers, Reciprocal effect of spin-orbit coupling, Nanophotonics.

Résumé

Le projet de thèse est divisé en deux parties. D'une part, la génération directionnelle et singulière de plasmons de surface (SPPs) par des ouvertures nanométriques a été réalisé et optimisé par le biais de microscopie à fuites radiatives (LRM). Nous démontrons expérimentalement qu'une structure plasmonique composée de nano-ouvertures en forme de T et Λ permet de contrôler le couplage unidirectionnel et radial des SPPs grâce au spin de la lumière incidente. Pour confirmer nos résultats expérimentaux, nous développons un modèle analytique qui décrit les coupleurs plasmoniques constitués de nano-ouvertures par représentation multidipolaire, permettant ainsi une explication théorique de la directionalité et de la formation de vortex plasmonique. L'optimisation des paramètres géométriques tels que l'angle au sommet des ouvertures en forme de Λ montre la possibilité de maximiser la directivité et le taux d'extinction à la fois pour le couplage directionnel et la génération des vortex dans le champ lointain. Par ailleurs, notre méthode basée sur la détection LRM, permet une analyse quantitative et est avérée être une technique de caractérisation sophistiquée pour cartographier le champ plasmonique. Il fournit également plusieurs nouvelles possibilités pour la focalisation de SPP contrôlée en polarisation.

D'autre part, le couplage spin-orbite de la lumière dans un guide et son effet réciproque sont réalisées et confirmées expérimentalement et théoriquement. Les coupleurs et découpleurs réseaux sur le guide d'ondes sont d'abord développés et étudiés. La sortie parfaite de la lumière confinée par le découpleur nous offre la possibilité de détecter les ondes guidées. La fluorescence des nanocristaux déposés sur la surface de l'échantillon montre une autre possibilité de visualiser directement la propagation de la lumière dans le guide d'onde. Le couplage directionnel contrôlé par spin est réalisé par des antennes en forme de Λ et est confirmé par des images en champ sombre avec des découpleurs et des images de fluorescence. En outre, l'effet réciproque est observé avec une imperfection de polarisation de sortie qui est expliqué théoriquement par le fait que les ordres de diffraction par les antennes en forme de Λ influent sur les états de polarisation finaux. Ainsi, l'effet réciproque est parfaitement réalisé par la sélection d'une région spécifique de diffraction dans le plan de Fourier. La caractérisation quantitative des interactions spin-orbite nous permet d'envisager le développement de nouveaux coupleurs directionnels dans le domaine de la nanophotonique tels que le traitement quantique de l'information.

Mots clés: Plasmons de surface, Microscope de fuites radiatives, Spin-orbite couplage directionnel, Singularité optique et vortex, Coupleurs du guide , L'effet réciproque du spin-orbite couplage, Nanophotonique.

Table of contents

List of figures

Introduction

Light can be coupled into propagating electromagnetic waves in a dielectric waveguide or at a metal-dielectric interface. The former, called guided waves, are known as indispensable ingredients in the development of integrated optical devices which enable an optical signal to propagate with minimal loss of energy. The latter, called Surface Plasmon Polaritons (SPPs), are considered as collective oscillations of electrons at the surface of metals which can confine the light energy at the subwavelength scale [1]. The strong confined properties of these two waves lead to many advances in the control of light at the nano-scale which offer a promising way for device development in the field of nanophotonics such as quantum information processing [2], optical trapping [3] etc.

In order to realize the directional control of light at the nano-scale, a large number of plasmonic structures are highly proposed and demonstrated such as the use of the Yagi-Uda antennas [4–7], tilted-angle illumination of slit [8], single V-antenna [9], asymmetric grooves [10] and so forth. However, in most of the methods, the propagating direction is limited by the structures or the incident positions. Thus, a direction tunable device is highly demanded. Recently, a series of spin-driven plasmonic structures have emerged such as T-shaped subwavelength apertures [11], L-shaped slots [10] and V-shaped slot antennas [12, 13]. Specifically, the propagating direction can be controlled by the handness of circular polarization of the incident light. But the directionality is not as high as we expect in many cases because the mechanism about the spin-based directional coupling still remain unclear in some parts.

Motivated by fundamental questions as well as by their potentials ranging from highly integrated photonic circuits to quantum optics, we developed our plasmonic structures called Λ-shaped couplers for the two confined waves. Firstly, the spin-based directional coupling of SPPs has been investigated including the side directional and radial directional (singular) generation of SPPs. Secondly, the same structures were applied on the waveguide in order to control the propagating direction of the guided light. During my 3-year PhD study, I worked at Institute Néel in Grenoble for the project about the directional and singular SPP generation.

Each year I spent three or four months at Institute Lumière Matière (ILM) in Lyon for the project about the directional coupling of light into the waveguide.

In my manuscript, the presentation is divided into 5 chapters including a general introduction about all the necessary knowledge, a description about the sample preparation, a presentation about the imaging systems for the experiment and two chapters about the explanation and discussion of results. Now, a short introduction about each chapter will be listed below:

1. **General consideration** The basic knowledge about the dielectric waveguide and the SPPs is thoroughly introduced in this chapter. The properties of waveguides are explained in both geometric and wave optics. The understanding of the guided modes and the coupling techniques helps us to design our coupler structures. Subsequently, another confined waves, SPPs, are presented. The optical properties of noble metals are firstly described as the preliminary knowledge for the SPPs. The dispersion relation of SPPs propagating at the metal-dielectric interface is deduced followed by solving the Maxwell equations and boundary conditions for two media. The properties of SPPs concluded from the dispersion relation provide us several possibilities for exciting and detecting SPPs. Lastly, a state of arts about the directional control of light is briefly reviewed.

2. **Sample preparation** The methods and processes of waveguide and nanostructure fabrication are explained in this chapter. The waveguide fabrication contains three steps which are the sol-gel process, the thin film deposition and the characterization of the TiO_2 waveguides. We show the optimal process for TiO_2 solution preparation and thin film deposition which is proven by characterizing the waveguide quality. Then, the nanopatterning of metals is presented by two methods which are the Focused Ion Beam (FIB) milling and Electron Beam Lithography (EBL). The FIB is ideal for engraving the nanostructures such as slits, grooves and so forth on the metal film, while the EBL is a precise way for deposition of metals on the substrate such as strips, ridges and so on. Then, a sample gallery with all the structures during my PhD study is shown at the end and some preliminary results are mentioned.

3. **Imaging systems** The Leakage Radiation Microscopy (LRM), dark field and fluorescence imaging and the methods for polarization analysis are described in this chapter. As a far-field method for direct imaging of SPP propagation, LRM is a powerful tool allowing a precise mapping and quantitative analysis. The principle of SPP detection on the direct plane and Fourier plane is explained and the experimental setup is displayed. Then, the dark field imaging system is introduced for observing the

directional coupling of light into the waveguide by filtering the incident excitation light. Furthermore, the fluorescence imaging serves as an efficient method for visualizing the propagation of guided modes because nanocrystals deposited on the sample surface can be excited by the confined waves in the waveguide. Lastly, the polarization generation and analysis used in our experiment are explained.

4. **Spin-controlled directional and singular SPP generation** The results of spin-driven directional and singular generation of SPPs are shown in this chapter. Firstly, the side unidirectional coupling of SPPs in the array of T-shaped and Λ-shaped apertures is experimentally realized and theoretically simulated by a multidipolar model. We introduce a parameter called directivity to quantify the capacity of the directionality. Subsequently, we optimize the directivity by the theoretical model and the experimental results confirm our expectation. Secondly, the radial directional coupling of SPPs called singular (inward) or vortex (outward) generation in the circle of T-shaped and Λ-shaped apertures is extended to study. The handedness of the structures is classified with the experimental results at the beginning. Then, we define another parameter called extinction ratio to characterize the capacity of the SPP singular generation. Lastly, the previous analytical model is adapted for the circle of apertures, which helps us to support the experimental findings and to optimize the extinction ratio of SPP singularity.

5. **System of emitters, nanostructures and waveguides** In this chapter, the coupler and decoupler systems for the waveguide are firstly introduced and tested. The coupler and decoupler gratings are proven for converting the free-space light to the confined wave or reversely, which is the first method to detect the guided wave. In addition, with the method of fluorescence imaging, the propagation of guided modes can be directly visualized by the strong beam, which provides us more details for the analysis of the directional coupling of light into the waveguide. Secondly, the optical spin-orbit coupling is demonstrated by the Λ-shaped antennas and evidenced by the dark field and fluorescence imaging. Thirdly, the reciprocal effect of spin-orbit coupling is proposed and investigated both experimentally and theoretically. Finally, the reciprocal effect is realized by filtering the specific region on the Fourier plane.

Chapter 1

General consideration

Abstract: In the first section, the basic knowledge about the dielectric waveguides is introduced. The dispersion relation of guided modes is described by both the ray and wave optics and the four kinds of coupling techniques are followed to present. In the second section, another confined waves, Surface Plasmon Polaritons (SPPs), are explained including the optical response of the noble metal, the dispersion relation of SPPs and the methods for excitation of SPPs. Lastly, a state of arts about the directional control of light is briefly reviewed.

Contents

1.1 Dielectric optical waveguides

The field of photonics, sometimes referred as optical electronics, has strongly evolved during the last decade [14]. Since optical waves are employed as carriers of information in

communication technology, the next step for developing integrated devices is to search for a suitable transmission medium. The early stages were dominated by attempting to utilize lens systems and mirrors to build light waveguides. Of the several problems that arise with such waveguides, the cost factor appears at present the most serious limitation for the actual use of lens waveguides in optical communication systems [15]. With the large demands and the rapid growth of integrated optics especially for optical interconnects [16], a promising type of transmission medium, which is dielectric optical waveguides, attracts a huge number of interest because of its smaller losses and lower costs.

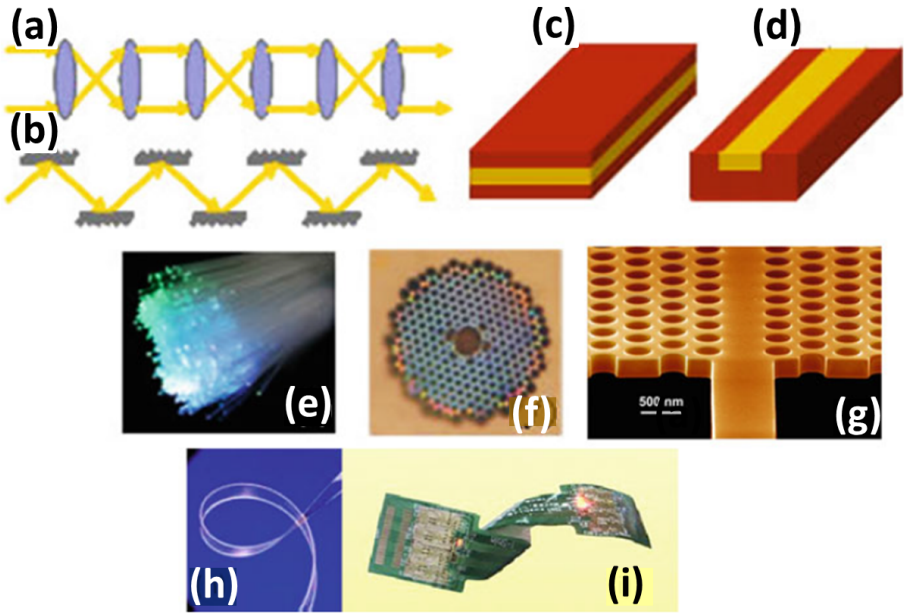

Fig. 1.1 Geometric classification of optical waveguides. (a), (b) Conventional lens and mirror waveguides. (c) Slab waveguide. (d) Strip waveguide. (e) Standard optical fibers. (f) Microstructured fiber. (g) Photonic cystal waveguide. (h) Flexible film waveguide and (i) its application in the flexible circuit board.

Until now, a large variety of optical waveguides has been developed depending on different application requirements. The classification based on the geometry is sketched in Figure 1.1 [17]. Dielectric slabs are the simplest and most widely used optical waveguides for both researches and typical integrated optical applications. It is shown schematically in Fig1.2, which used three different media. The core region with thickness d is assumed to have refractive index n_1 and is deposited on the substrate with refractive index n_2 which is glass substrate during our study. The refractive index n_3 above the core region might be unity since the superstratum is air in our case. It is necessary that n_1 is larger than n_2 and n_3. If n_2 is not equal to n_3, this is called the asymmetric waveguide which will be thoroughly

introduced in this section. We have to note that the dielectric mediums are considered to be isotropic and homogeneous. In order to better understand the mechanism of propagation of guided waves, we will start from both geometrical and wave optics.

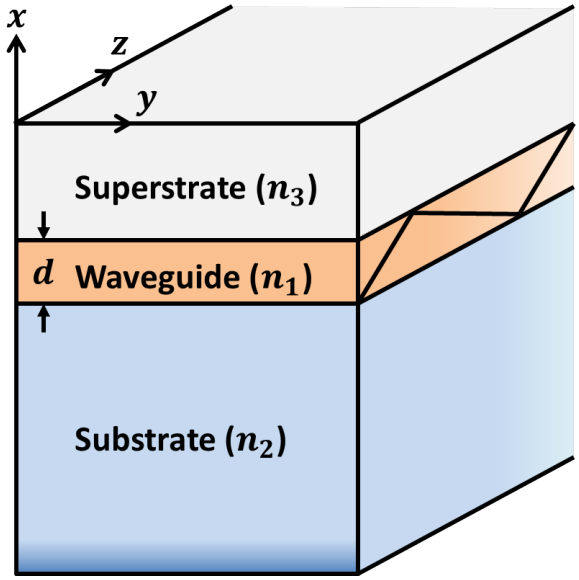

Fig. 1.2 Schematic of a basic planar waveguide. The guided light propagates in the core region with the highest refractive index (n_1).

1.1.1 Geometrical optics of planar waveguides

Geometrical (or ray) optics describes the propagation of light fields by defining rays as the lines that cross the surfaces of constant phase of the light field at right angles. Light rays have intuitive appeal since a narrow beam of light is a good approximation to the more abstract notion of light rays. Therefore, the schematic guided ray can be illustrated in Figure 1.3. If no light beam emerges on the opposite side of the dielectric interface, all the light is totally reflected inside medium 1 (n_1). Based on the Snell's law, the upward and downward critical angles (θ_{3c} and θ_{2c}) of the total internal reflection between two interface can be defined as:

$$\theta_{3c} = \arcsin\frac{n_3}{n_1}, \quad \theta_{2c} = \arcsin\frac{n_2}{n_1}. \tag{1.1}$$

In our case, $\theta_{3c} < \theta_{2c}$ because $n_3 < n_2$. If $\theta_{2c} < \theta < \pi/2$, at least one guided mode propagates within the "zigzag" trajectory along the waveguide.

If $\theta_{3c} < \theta < \theta_{2c}$ or $\theta \leq \theta_{3c}$, then the light cannot be confined in the waveguide because at least a radiation or a leaky mode occurs on the substrate part with energy dissipation.

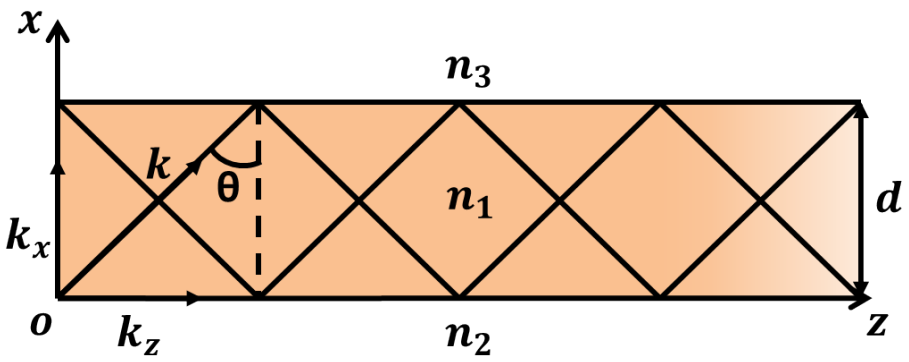

Fig. 1.3 Sketch of a basic slab waveguide in the plane Oxz. k_x and k_z respectively represent the projection of wave vector k on the axis Ox and Oz. The angle θ indicates the incident angle with respect to the dashed line normal to the interface.

The wave vector k perpendicular to the wavefront represents the direction of the wave propagation. It is defined as:

$$k = \frac{2\pi}{\lambda} = \frac{2\pi}{\lambda_0} n_1 = k_0 n_1, \tag{1.2}$$

where λ is the wavelength in the waveguide; λ_0 is the wavelength in the vacuum; k_0 is the wave vector in the vacuum. To better characterize the guided modes in the waveguide, an important parameter called the propagation constant is introduced as:

$$\beta = k_z = k_0 n_1 \sin\theta = \frac{\omega}{v_p}, \tag{1.3}$$

where ω is the angular frequency and v_p is the phase velocity of guided modes. The normalized propagation constant N_m so-called effective index of the mode m is defined as:

$$N_m = \frac{\beta}{k_0} = n_1 \sin\theta, \tag{1.4}$$

with the condition of $n_2 < N_m < n_1$ for the guided modes, in which m stands for the different propagation modes in the waveguide [18]. The guided modes correspond to several discrete values of θ. In order to obtain the complete description of these eigenvalues of the guided modes (dispersion relation), the Maxwell equations and boundary conditions have to be taken into consideration.

1.1.2 Electromagnetic solution for the guided modes

In the ray optics, the effect of wavelength is neglected in the propagation modes. But if the waveguide thickness is the same order of magnitude as the wavelength (λ_0), the Maxwell equations serve as a more accurate method for the investigation of the guided modes. Maxwell equations without the external charge ($p = 0$) and current densities ($J = 0$) can be written in the form:

$$\begin{aligned} rot\,\overrightarrow{E} &= -\mu_0 \frac{\partial \overrightarrow{H}}{\partial t}, \qquad & div\,\overrightarrow{E} &= 0, \\ rot\,\overrightarrow{H} &= -\varepsilon_0 n^2 \frac{\partial \overrightarrow{E}}{\partial t}, \qquad & div\,\overrightarrow{H} &= 0. \end{aligned} \tag{1.5}$$

$\overrightarrow{E}$ and $\overrightarrow{H}$ are the electric and magnetic field vectors, and ε_0 and μ_0 are the dielectric permittivity and magnetic permeability of vacuum. Magnetic materials are not considered in this thesis so that the use of the vacuum constant μ_0 is sufficient. The refractive index of the medium is designated by n.

We consider only strictly time harmonic fields whose time dependence and the z dependency of the mode fields since we are interested in obtaining the normal modes of the slab waveguide along the z direction. In complex notation, the electric and magnetic field vectors can be expressed as:

$$\begin{aligned} \overrightarrow{E}(xyz) &= \overrightarrow{E}(xy)\exp^{i(\beta z-\omega t)}, \\ \overrightarrow{H}(xyz) &= \overrightarrow{H}(xy)\exp^{i(\beta z-\omega t)}. \end{aligned} \tag{1.6}$$

The modes of the slab waveguide can be classified as TE and TM modes shown in Figure 1.4. TE or transverse electric modes do not have a component of the electric field in the direction of wave propagation (E_y, H_x, H_z), while TM or transverse magnetic modes do not have a longitudinal magnetic field component (E_x, E_z, H_y). We consider TE and TM modes separately.

We simplify the description of the slab waveguide by assuming that there is no variation in the y direction (in the plane Oxz), which we express symbolically by the equation $\frac{\partial f}{\partial y} = 0$, $f = E, H$. Thus we obtain from the Maxwell equation (1.5) for the TE mode:

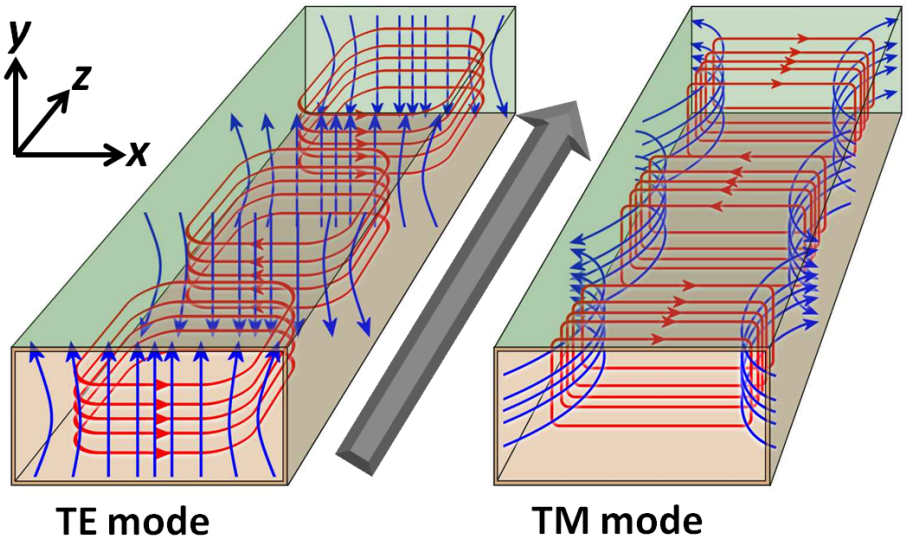

Fig. 1.4 Two types of propagation modes in slab waveguides. The grey arrow indicates the direction of wave propagation. The blue line and red line represent the electric field and magnetic field respectively.

$$\begin{aligned} Hx &= -\frac{\beta}{\omega\mu_0}E_y, \\ Hz &= \frac{1}{i\omega\mu_0}\frac{\partial E_y}{\partial x}, \\ \frac{\partial^2 E_y}{\partial x^2} &+ (k_0^2 n^2 - \beta^2)E_y = 0, \end{aligned} \tag{1.7}$$

and for the TM mode:

$$\begin{aligned} Ex &= \frac{\beta}{\omega\varepsilon_0 n^2}H_y, \\ Ez &= -\frac{1}{i\omega\varepsilon_0 n^2}\frac{\partial H_y}{\partial x}, \\ \frac{\partial^2 H_y}{\partial x^2} &+ (k_0^2 n^2 - \beta^2)H_y = 0, \end{aligned} \tag{1.8}$$

with $k_0^2 = \omega^2\varepsilon_0\mu_0 = (\frac{2\pi}{\lambda_0})^2$. Now, if $E_y(x)$ and $H_y(x)$ are determined, the rest of field components can be easily deduced. Fortunately, equation of $E_y(x)$ and $H_y(x)$ have the same form for the two modes TE or TM. A common equation can be expressed as:

$$\frac{\partial^2 \psi}{\partial x^2} + \Omega^2 \psi = 0, \tag{1.9}$$

where ψ represents $E_y(x)$ or $H_y(x)$ and $\Omega^2 = (k_0^2 n^2 - \beta^2)$. Based on the general solution for the above equation, we derive a propagative solution and an evanescent solution, which are written respectively:

$$\begin{aligned} \psi(x) &= A\exp(ik_0 px) + B\exp(-ik_0 px), \qquad if \;\; n > \frac{\beta}{k_0} = N_m, \\ \psi(x) &= C\exp(k_0 qx) + D\exp(-k_0 qx), \qquad if \;\; n < \frac{\beta}{k_0} = N_m, \end{aligned} \tag{1.10}$$

with $p = \sqrt{n^2 - (\frac{\beta}{k_0})^2}$ and $q = \sqrt{(\frac{\beta}{k_0})^2 - n^2}$. Apparently, β plays a critical role for the solutions of the above equations. Now we just consider the case TE in detail. Solutions, which satisfy these conditions for the electric or magnetic field and vanish at $x = \pm\infty$, are deduced according to the equation (1.7):

- In the medium n_3: $x > d$, $n_3 < N_m$:

$$\begin{aligned} E_y(x) &= D\exp(-k_0 q_3 (x-d)), \\ H_x(x) &= -\frac{\beta D}{\omega\mu_0}\exp(-k_0 q_3 (x-d)), \\ H_z(x) &= -\frac{k_0 q_3 D}{i\omega\mu_0}\exp(-k_0 q_3 (x-d)), \\ with \;\; q_3 &= \sqrt{(\frac{\beta}{k_0})^2 - n_3^2}. \end{aligned} \tag{1.11}$$

- In the medium n_2: $x < 0$, $n_2 < N_m$:

$$\begin{aligned} E_y(x) &= C\exp(k_0 q_2 x), \\ H_x(x) &= -\frac{\beta C}{\omega\mu_0}\exp(-k_0 q_2 x), \\ H_z(x) &= \frac{k_0 q_2 C}{i\omega\mu_0}\exp(-k_0 q_2 x), \\ with \;\; q_2 &= \sqrt{(\frac{\beta}{k_0})^2 - n_2^2}. \end{aligned} \tag{1.12}$$

- In the medium n_1: $0 < x < d$, $n_1 > N_m$:

$$\begin{aligned} E_y(x) &= A\exp(ik_0p_1x) + B\exp(-ik_0p_1x), \\ H_x(x) &= -\frac{\beta}{\omega\mu_0}(A\exp(ik_0p_1x) + B\exp(-ik_0p_1x)), \\ H_z(x) &= \frac{k_0p_1}{\omega\mu_0}(A\exp(ik_0p_1x) - B\exp(-ik_0p_1x)), \\ with \;\; p_1 &= \sqrt{n_1^2 - (\frac{\beta}{k_0})^2}. \end{aligned} \tag{1.13}$$

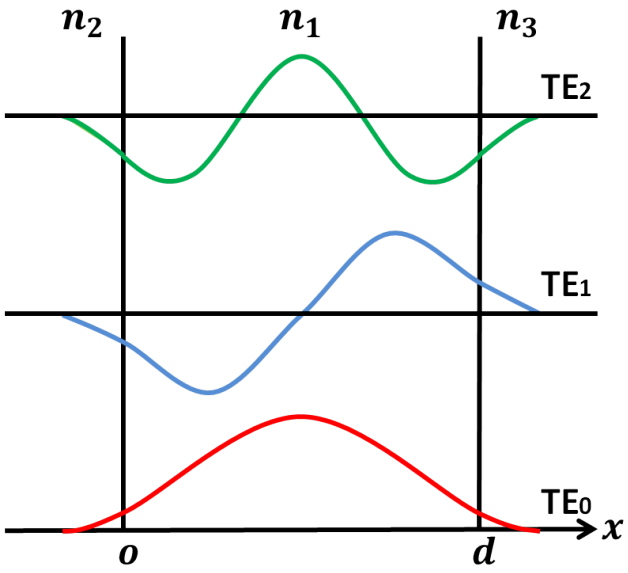

Fig. 1.5 Illustration of transverse electric field distributions and the first three guided modes in a slab waveguide.

The Figure 1.5 illustrates the first three TE modal field patterns according to the three equations above. The higher-order mode dissipates more energy into the n_2 and n_3 regions than lower-order modes [17]. After a quick glance on the intuitive field distribution in the waveguide, the only remaining complication requires that the solutions must satisfy the boundary conditions at two dielectric interfaces which is to say that E_y, H_x and H_z must be continuous at $x = 0$ and $x = d$. Thus, the coefficients A, B, C and D are derived:

- At the interface of n_1 and n_2, $x = 0$:

$$\begin{aligned} C &= A + B, \\ Cq_2 &= ip_1(A - B). \end{aligned} \tag{1.14}$$

- At the interface of n_1 and n_3, $x = d$:

$$\begin{aligned} D &= A\exp(ik_0p_1d) + B\exp(-ik_0p_1d), \\ -q_3D &= ip_1(A\exp(ik_0p_1d) - B\exp(-ik_0p_1d)). \end{aligned} \tag{1.15}$$

In order to have solutions for these 4 coefficients, the 4 x 4 determinant has to be equal to 0. It is expressed as:

$$p_1(q_2+q_3)\cos(k_0p_1d) = -(q_2q_3 - p_1^2)\sin(k_0p_1d). \tag{1.16}$$

It is further simplified as:

$$\tan(k_0p_1d) = \frac{\frac{q_2}{p_1} + \frac{q_3}{p_1}}{1 - \frac{q_2q_3}{p_1^2}} = \frac{\tan\Phi_2 + \tan\Phi_3}{1 - \tan\Phi_2\tan\Phi_3} = \tan(\Phi_2 + \Phi_3), \tag{1.17}$$

with $\tan\Phi_2 = \frac{q_2}{p_1}$ and $\tan\Phi_3 = \frac{q_3}{p_1}$. The more general equation is deduced as:

$$(k_0p_1d) - \Phi_2 - \Phi_3 = m\pi, \qquad m = 0,1,2... \tag{1.18}$$

The equation above is called dispersion relation of TE guided modes because it indicates the relation between ω and β. If we take a quick look at this equation in geometrical optics, the physical significations are easily found in Figure 1.6. Since all points on the same wave front of a plane wave must be in phase, the light traveling from A to B must be in phase with the ray going from C to D. The difference of optical path lengths between AB and CD is required to be a multiple of 2π. The ray AB is assumed to have encountered no reflection but the ray CD has encountered two internal reflections at point E and point F which resulted in the phase change of $2\Phi_3$ and $2\Phi_2$. The rest phase difference results from the deviation of lengths between the path EF and GH which corresponds to the term $2k_0p_1d$.

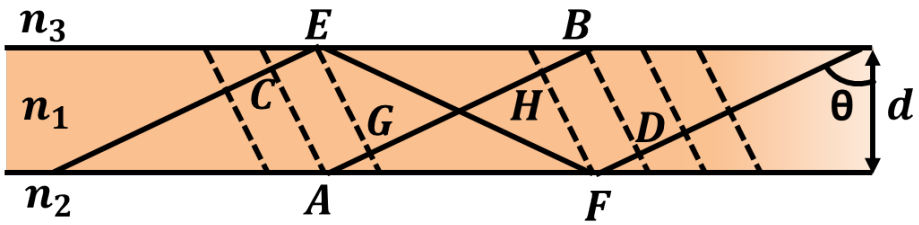

Fig. 1.6 Illustration of phase conditions that lead to the eigenvalue equation. All rays in solid line that travel in the same dierection belong to the same plane wave. The phase fronts of the plane waves is depicted as dashed lines.

When we use the effective index of the mode m (N_m) to replace $\frac{\beta}{k_0}$, the dispersion relation of TE modes is expressed as:

$$\frac{2\pi}{\lambda_0} d\sqrt{n_1^2 - N_m^2} = \arctan\left(\sqrt{\frac{N_m^2 - n_2^2}{n_1^2 - N_m^2}}\right) + \arctan\left(\sqrt{\frac{N_m^2 - n_3^2}{n_1^2 - N_m^2}}\right) + m\pi. \tag{1.19}$$

With the similar method, the dispersion relation of TM modes is established:

$$\frac{2\pi}{\lambda_0} d\sqrt{n_1^2 - N_m^2} = \arctan\left(\frac{n_1^2}{n_2^2}\sqrt{\frac{N_m^2 - n_2^2}{n_1^2 - N_m^2}}\right) + \arctan\left(\frac{n_1^2}{n_3^2}\sqrt{\frac{N_m^2 - n_3^2}{n_1^2 - N_m^2}}\right) + m\pi. \tag{1.20}$$

So far, the discrete values of θ corresponding to guided modes have been determined and well investigated. If the incident wavelength and the waveguide media are fixed, the possible mode m is associated with the thickness of the waveguide. This equation will serve us for characterization of the waveguide such as the thickness and the effective index in the chapter 2. If the thickness is small enough, only one possible mode is allowed to propagate in the waveguide. It is called monomode regime and the other cases are called multimode regime. With developing the thin film deposition technology, the thinner dielectric waveguide is available for the monomode in different applications [19].

1.1.3 Coupling techniques for waveguides

After understanding the guided mode propagation in the waveguide system, we need a good coupling method for inserting an incident light into the waveguide or reversely transmitting the light out of the waveguide to the receiver. It is an important step for the energy transfer because the laser beam belongs to a radiation mode which needs to be effectively confined and coupled into the waveguide. Several techniques have been used for carrying out such coupling requirements, including prism coupling, end coupling, tapered coupling and grating coupling [20].

Prism coupling is highly efficient and is mode selective, but requires placement of a prism on top of the waveguide with a carefully adjusted gap between the prism and the waveguide. This makes the prism coupling technique unsuitable for fast, alignment tolerant coupling to a disposable waveguide system [21]. Since this method serves as the characterization of our waveguides, the brief principle is explained here. As shown in Figure 1.7(c), a prism with a high refractive index n_p is put close to the waveguide with a thin gap layer of n_2 (here $n_2 = 1$ because it is air) [22]. When the light beam is launched into the bottom of the prism at an

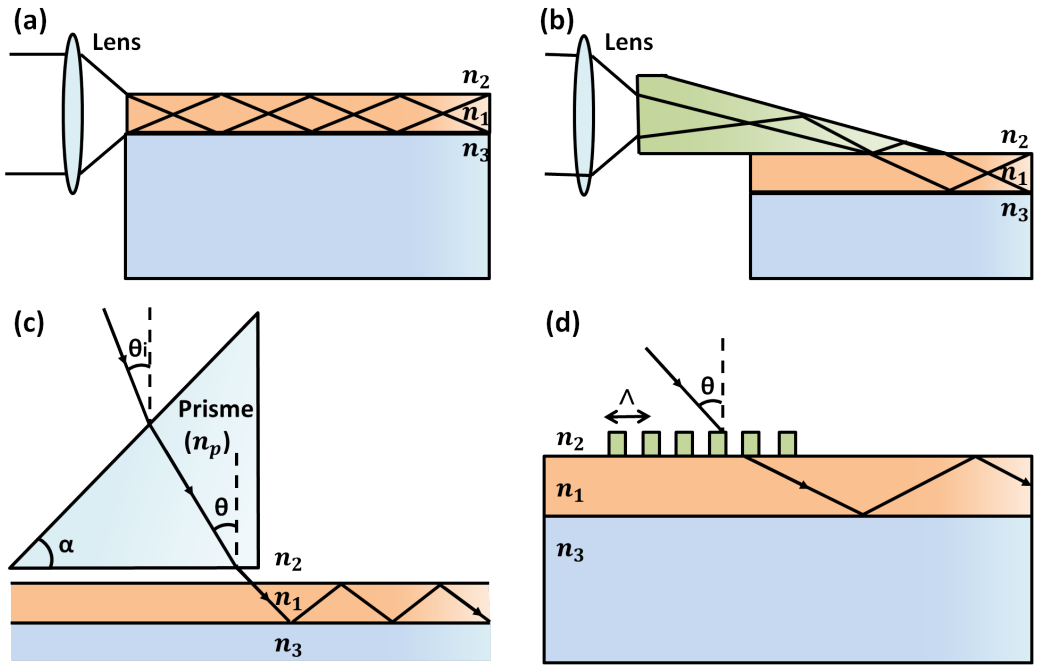

Fig. 1.7 Schematic illustration of four general coupling techniques. (a) End coupling technique. The light is focused into one end of the waveguide by using a lens. (b) Tapered coupling technique. The lens like in the (a) serves the light beam to focus into a taper and the tapered side is then placed on the waveguide surface. (c) Prism coupling technique. A prism with a high refractive index n_p and an apex angle α is placed close to the waveguide. The incident angle with respect to the vertical dashed line is expressed as θ_i. The refractive angle on the bottom of the prism with respect to the vertical dashed line is expressed as θ. (d) Grating coupling technique. The period of the grating and the incident angle are indicated as Λ and θ.

angle θ, the propagation constant of prism β_p along the waveguide plan (the z-direction) is given by [23]:

$$\beta_p = k_0 n_p \sin\theta. \tag{1.21}$$

The incident light angle θ_i with respect to the same vertical dashed line has the relation below according to the Snell's law:

$$n_2 \sin(\alpha - \theta_i) = n_p \sin(\alpha - \theta). \tag{1.22}$$

When β_p is consistent with the propagation constant of a guided mode β_g ($N_m = n_1 \sin\theta_m = n_p \sin_\theta$), the guided wave is excited through the distributed coupling resulting from phase matching between the evanescent wave and the guided mode. This energy transfer

is effectuated through the evanescent wave created in the intermediate air gap between prism and waveguide, which is called the optical tunneling effect [22, 23].

Under the condition of matching phase, the effective refraction index of mth mode N_m can be expressed by combining with the equation (1.22) as:

$$N_m = n_p \sin(\alpha + \arcsin(\frac{\sin\theta_i}{n_p})). \tag{1.23}$$

This equation is an important principle for characterization of the waveguide and will be used in the chapter 2. From the equation (1.23), a value of the effective refraction index N_m of the mth mode can be inferred as long as one θ_i is measured, since the values of n_p and α are known from the prism chosen.

The end coupling method shown in Figure 1.7(a) is simple and efficient, but the input beam from the source needs to be directed into the end of waveguide, requiring alignment accuracy at least as small as the thickness of the guide. Therefore, this method works well for thick waveguides (thicknesses greater than about 1 mm) and is simple in design, but its coupling efficiency drops for thinner guides [17].

On the contrary, the tapered coupling shown in Figure 1.7(b) gives better efficiency for the thinner waveguides, but fabricating the tapered end is more difficult and makes this method very sensitive to operating conditions [24].

The grating coupling shown in Figure 1.7(d) is relatively easy to fabricate by e-beam lithography once the size is defined. The coupling efficiency of the grating coupler is not as high as the tapered coupling, probably due to imperfections in the replication process. The grating coupler is mode selective however, and would be a better choice than the tapered coupler for a thin film, few-mode guide.[25]

This grating method will be used for coupling and out-coupling in our experiments thanks to the period-dependence and no need for strict alignments. The principle is also very similar to the prism coupling method which has to respect a phase matching condition. When a laser beam with propagation constant β_0 impinges on the grating, the diffracted light can couple as a guide mode as long as it satisfies the condition $\beta_g = \beta_0 + n\frac{2\pi}{\Lambda}$ where the integers n and $\wedge$ represent the order of diffraction and the period of the grating respectively. This condition is alternatively expressed as:

$$n_2 \sin\theta + n\frac{\lambda_0}{\Lambda} = N_m. \tag{1.24}$$

In brief, the advantage and disadvantage of some coupling methods are summarized in Table 1.1 [25].

Table 1.1 Comparison of four coupling techniques for waveguide.

Coupling Techniques	Advantages	Disadvantages
Prism coupling	High efficiency; mode selective	Complex; difficult to align
End coupling	High efficiency for thick waveguides	Difficult to align for thin waveguides
Tapered coupling	Tolerant of alignment	Long, thin taper required for thin waveguides
Grating coupling	Tolerant of alignment; mode selective	Lower efficiency

1.2 Surface plasmons

Surface plasmon, which is a kind of electromagnetic waves propagating along the interface between a metal and a dielectric caused by collective free electron oscillations [1], hold much research interest in the past decades on the field of optical information technology, biological sensing, microscopy imaging and photonic device [2, 26, 27].

Actually, plasmon resonances have been used without a clear understanding to create various colors in glass goblets and in stained-glass windows of churches as shown in Figure 1.8 from the very old era. This feature was firstly described due to the doping metal particles in dielectrics by Maxwell Garnett [28] at the beginning of the twentieth century. Almost at the same period, Robert Williams Wood noticed unexplained features in optical reflection measurements on metallic gratings [29, 30] and the first theoretical treatment of these anomalies was presented by Lord Rayleigh [31], which was later refined by Fano [32]. In 1908, Gustav Mie, who firstly connected the plasmon resonance to optical properties of metal particles, developed his now widely used theory of light scattering by spherical particles [33]. Fifty years later, more experimentation was proven that the electron energy losses by passing thorough thin metal films were attributed to the collective oscillation of free electrons near the surface of metals [34] and this oscillation was defined as surface plasmons. One year later, the concept "Surface Plasmon Polaritons" (SPPs) was introduced by David Pimes and David Bohm for the coupled oscillation of bound electrons and light inside the transparent medium [35, 36]. Afterwards, optical excitation methods of SPPs were introduced by Andreas Otto and Erich Kretschmann [37, 38], so that it is possible to easily control SPPs for researches and to transfer it into applications. With the dramatic growth of nanoscale fabrication techniques such as Focused Ion Beam (FIB) and Electron Beam (E-Beam) lithography and the rapid development of computational methods for modeling, SPPs are nowadays being deeply investigated and are highly implemented into useful technologies such as Surface Enhanced

Raman Scattering (SERS) biosensors [39, 40], subwavelength-apertures perfect lens beyond the diffraction limit [41, 42], plasmonic resonator [43, 44], etc. The mechanism and basic properties of SPPs are discussed in the following section.

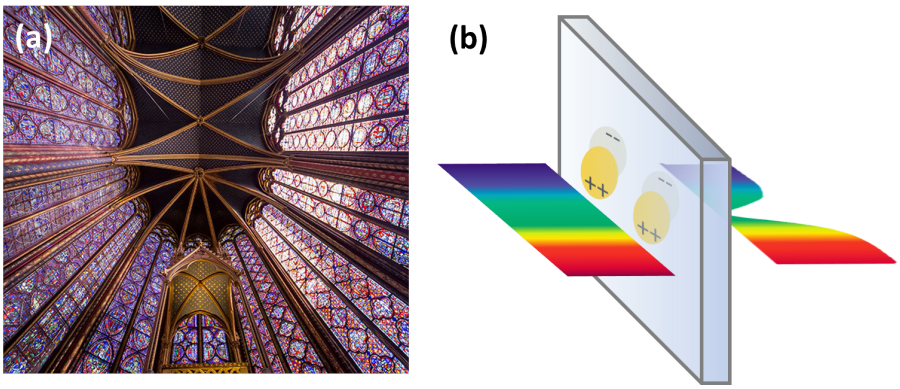

Fig. 1.8 (a) The photo taken in the church Sainte-Chapelle in Paris shows the amazing set of stained-glass windows. The vibrant colors of windows is taken advantage of the plasmon effect by incorporating small metallic or metallic-oxide particles in the glass. For example, the red color is attributed to the doped gold particles. Yellow from silver particles and blue from cobalt particles etc. (b) Gold, like many metals, has a high electron density, and the electrons effectively comprise a plasma within each particle. When light shines through the stained glass, some wavelengths are plasmonically absorbed and others pass through. The red color for gold is due to the absorption of the mostly green part.

1.2.1 The properties of noble metals

In the previous section, the dielectric permittivity ε was less discussed and assumed to be a real number because we neglected the relatively small loss and wavelength-dependency in dielectrics. Technically, the dielectric permittivity of metals is confirmed to be a complex number instead of a real number because it is highly dependent on the incident wavelength and strong absorption was found for the certain wavelengths as well. The optical properties of metals can be described by a free electron gas and the metal interband transitions. Thus two models were built to describe these two phenomena. The Drude model is well adapted especially for alkali metals to describe the free electron gas but is not sufficient for the description of noble metals such as gold and silver. If the incident energy is larger than the energy of transitions from the valence band to the conduction band, the Drude model is not valid any more. Thus a model of interband transitions is introduced to complete the inaccuracy of the Drude model. Now, let's start with the classic Drude model. The electric induction ($\vec{D}$) and the electric field ($\vec{E}$) are linked via the polarization ($\vec{P}$) in this way:

$$\overrightarrow{D} = \varepsilon_0 \overrightarrow{E} + \overrightarrow{P}. \tag{1.25}$$

The polarization ($\overrightarrow{P}$) describes the electric dipole moment per unit of volume inside the material, caused by the alignment of dipoles with the electric field [1]. The relationship between $\overrightarrow{P}$ and $\overrightarrow{E}$ is defined as:

$$\overrightarrow{P} = \varepsilon_0 \chi \overrightarrow{E}, \tag{1.26}$$

where χ represents the dielectric susceptibility (particularly in quantum mechanical treatments of the optical response [45]). By combining eq. 1.25 and eq. 1.26, the dielectric constant of materials or relative permittivity (ε) is introduced as:

$$\overrightarrow{D} = \varepsilon_0(1+\chi)\overrightarrow{E} = \varepsilon_0 \varepsilon \overrightarrow{E}. \tag{1.27}$$

In the Drude model, the free electrons in the metal are considered to oscillate around the equilibrium position as a spring in response to the applied electromagnetic field. The damping motion can be well described with a characteristic collision frequency $\gamma = 1/\tau$. τ is known as the relaxation time of the free electron gas, which is typically on the order of 10^{-14} s at room temperature, corresponding to $\gamma = 100$ THz [46]. If the incident light is assumed to be a harmonic time-dependence driving field with a frequency ω ($\overrightarrow{E}(t) = \overrightarrow{E}_0 \exp^{-i\omega t}$), a differential equation describing the oscillation displacement of the electron gas ($\overrightarrow{x}$) is defined as:

$$m_e \frac{\partial^2 \overrightarrow{x}}{\partial t^2} + m_e \gamma \frac{\partial \overrightarrow{x}}{\partial t} = -e \overrightarrow{E}_0 \exp^{-i\omega t}, \tag{1.28}$$

where m_e and $-e$ denote the effective mass of the electron and its charge respectively. The particular solution of this equation is expressed as:

$$\overrightarrow{x}(t) = \frac{e}{m_e(\omega^2 + i\gamma\omega)} \overrightarrow{E}(t). \tag{1.29}$$

The complex coefficient in front of $\overrightarrow{E}(t)$ can be physically explained as a phase shift between the driving field and the response of metals. According to the definition of macroscopic polarization ($\overrightarrow{P} = -en\overrightarrow{x}$, here n is the number of displaced electrons), the polarization induced by displaced electrons can be written as:

$$\overrightarrow{P}(t) = -\varepsilon_0 \frac{ne^2}{\varepsilon_0 m_e(\omega^2 + i\gamma\omega)} \overrightarrow{E}(t) = -\varepsilon_0 \frac{\omega_p^2}{\omega^2 + i\gamma\omega} \overrightarrow{E}(t), \tag{1.30}$$

where $\omega_p^2 = \frac{ne^2}{m_e \varepsilon_0}$ denotes the plasma frequency of the free electron gas described as the natural frequency of a free oscillation of electrons. Combining Equation 1.30 with Equation 1.25, it is derived as:

$$\overrightarrow{D}(t) = \varepsilon_0 (1 - \frac{\omega_p^2}{\omega^2 + i\gamma\omega}) \overrightarrow{E}(t). \tag{1.31}$$

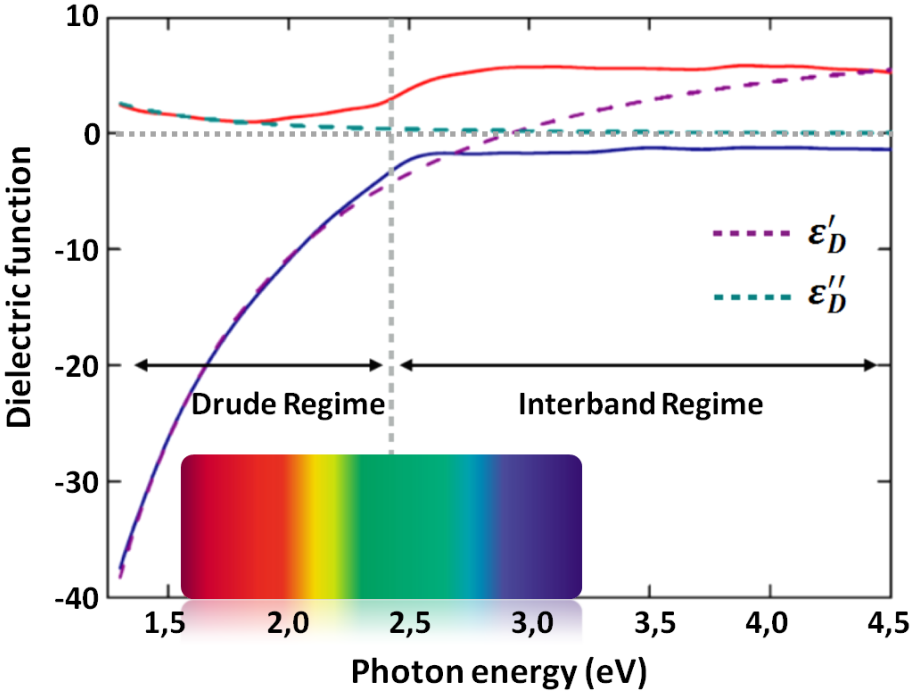

Fig. 1.9 The dielectric function of gold as the function of incident photon energy. The blue and red solid lines indicate the real and imaginary part dielectric function fitted by experimental data of Johnson and Christy [47]. The green and purple dashed lines represent the theoretical dielectric function based on Drude model. The discrepancy between Drude model and experimental results dramatically start from the vertical grey dashed line corresponding to the visible green light. It results from the interband transitions of electrons excited by higher photon energies.

Thus the dielectric function of free electron gas according to the Drude model is expressed as:

$$\varepsilon_D(\omega) = 1 - \frac{\omega_p^2}{\omega^2 + i\gamma\omega} = \varepsilon'_D(\omega) + i\varepsilon''_D(\omega). \tag{1.32}$$

The real and imaginary part of this complex dielectric function are separately expressed as with replacing $\gamma = \frac{1}{\tau}$:

$$\varepsilon'_D(\omega) = 1 - \frac{\omega_p^2 \tau^2}{1+\omega^2\tau^2}, \qquad \varepsilon''_D(\omega) = \frac{\omega_p^2 \tau}{\omega(1+\omega^2\tau^2)}, \tag{1.33}$$

where the real part of the dielectric function contributes the refractive index (n) and the imaginary part determines the absorption of the energy in the medium. As mentioned before, the Drude model describes well the optical response of metals with a driving field in the low-frequency regime but it is not valid any longer for the higher energy based on experimental measurements of noble metals (for example the discrepancy of gold starts from the visible light 520nm [48]). This phenomenon results from the interband transition which means electrons from the filled band below the Fermi lever are excited to higher energy lever bands due to the influence of photons with high energy [49, 50] depicted in Figure 1.10.

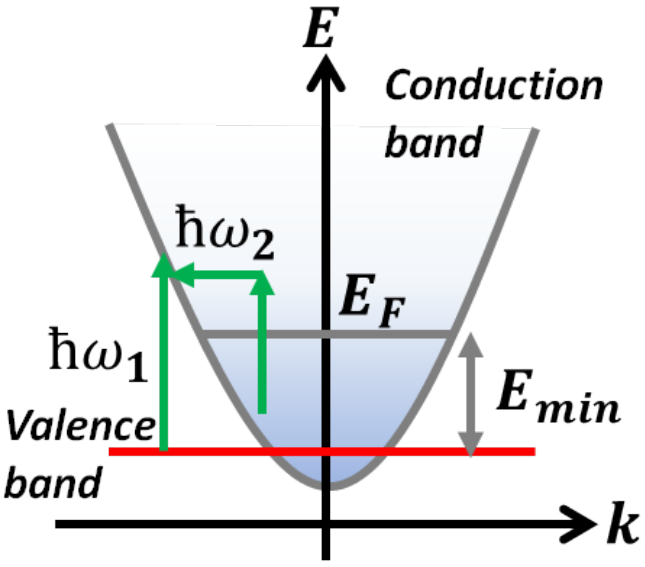

Fig. 1.10 Interband transitions between two energy levels of electrons in metal. Above a threshold energy (E_{min}), photons are very efficient in inducing electron transition from the lower energy levels to the levels above Fermi level (E_F). Two transitions involved which include intraband and interband transitions indicated by the green arrows. Electrons in the conduction band (parabolic sp-band) can be transferred to the other place in the same band with energy $\hbar\omega_2$ known as intraband transition. Electrons from the valence band (red-line d-band) can also be excited to the conduction band with energy $\hbar\omega_1$ known as interband transition [51].

Therefore, an additional term was introduced into the former oscillation model so as to compensate the inadequacy of the Drude model. Equation 1.28 can be modified as:

$$m_e \frac{\partial^2 \overrightarrow{x}}{\partial t^2} + m_e \gamma \frac{\partial \overrightarrow{x}}{\partial t} + m_e \omega_0^2 \overrightarrow{x} = -e \overrightarrow{E}_0 \exp(-i\omega t), \tag{1.34}$$

where ω_o describes bound electrons with a resonance frequency during interband transitions. For the similar method, the solution of the dielectric function of interband transitions ($\varepsilon_I(\omega)$) can be deduced. Thus the total dielectric function ($\varepsilon(\omega)$) is accurately expressed as:

$$\varepsilon(\omega) = \varepsilon_D(\omega) + \varepsilon_I(\omega). \tag{1.35}$$

1.2.2 Surface plasmon polaritons at the interface

Volume plasmon is known as the quanta of the charge density oscillation inside the metal. While in the case of two media, the charge oscillations at the interface of two media were observed and named surface plasmons. The surface plasmons naturally coupled with electromagnetic wave (photons) were designated as surface plasmon polaritons (SPPs). SPPs attract a lot of interest since they can propagate at the interface between a dielectric and a conductor and are evanescently confined in the perpendicular direction.

Now, let's start to understand the SPPs propagating along a plane interface between two media. We consider a general non-absorbing dielectric with a positive real dielectric function ε_2 at the half space ($z > 0$) and a metal medium with a complex frequency-dependent dielectric function ε_1 at the adjacent half space ($z < 0$). The schematic image is shown in Figure 1.11. Ψ denotes the electric or magnetic field along y E_y or H_y like in the first section. If we consider a TE mode, there are only E_y, H_x, H_z and Ψ stands for E_y. If we consider a TM mode, there are only H_y, E_x, E_y and Ψ represents H_y. By definition of surface plasmons, the wave can propagate along the x axis and be confined along the z axis. Thus the SP field Ψ can be expressed as:

$$\begin{aligned} \Psi_1 &= A_1 \exp^{k_{1z} z} \exp^{i(k_x x - \omega t)}, \qquad z < 0 \\ \Psi_2 &= A_2 \exp^{-k_{2z} z} \exp^{i(k_x x - \omega t)}, \qquad z > 0 \end{aligned} \tag{1.36}$$

where A_1 and A_2 represent the arbitrary amplitudes of two waves in different media. k_{1z} and k_{2z} are defined as positive wave numbers. According to the Maxwell equations, the field equations have been derived as Equation (1.7) and Equation (1.8) in the previous section. By introducing the boundary conditions at interface (Z=0), the continuity of E_y, H_x and H_z in TE mode has to be respected

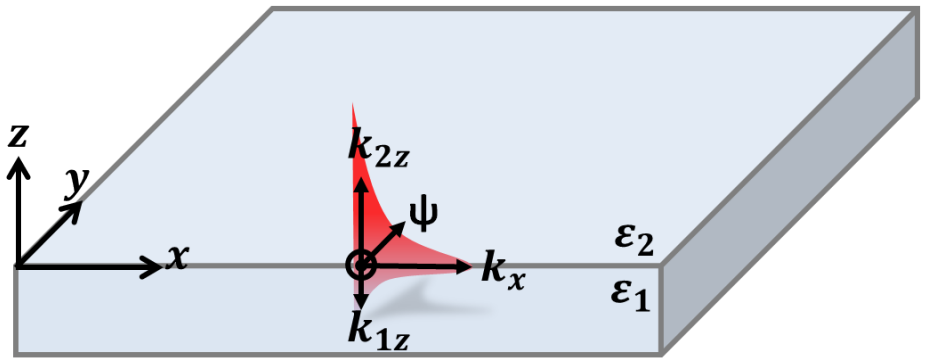

Fig. 1.11 Schematic of SPPs propagating at the interface between a dielectric and a metal. The components of the surface plasmon polariton (SPP) field are defined as Ψ, k_x and k_z.

$$\begin{aligned} A_1 &= A_2, \\ \frac{k_{2z}}{k_{1z}} &= -\frac{A_1}{A_2}. \end{aligned} \tag{1.37}$$

Since the convention of signs was defined that k_{1z} and k_{2z} were both positive number, the condition is only fulfilled if $A_1 = A_2 = 0$. It means that no surface plasmon modes exist for TE polarization. By the same method, the condition of the continuity of H_y, E_x and E_z in TM mode requires that:

$$\begin{aligned} A_1 &= A_2, \\ \frac{k_{2z}}{k_{1z}} &= -\frac{\varepsilon_2 A_1}{\varepsilon_1 A_2}, \end{aligned} \tag{1.38}$$

and

$$\begin{aligned} k_{1z}^2 &= k_x^2 - k_0^2 \varepsilon_1, \\ k_{2z}^2 &= k_x^2 - k_0^2 \varepsilon_2, \end{aligned} \tag{1.39}$$

where $k_0 = \frac{\omega}{c}$ is the wave vector of the incident excitation. Note that the real part of metal dielectric function ε_1' is negative and ε_2 is positive. The self-consistent condition can be satisfied and by combining Equation (1.38) and Equation (1.39), we achieve the most important result, which is the dispersion relation of SPPs propagating at the interface between two half spaces:

$$k_x = k_{spp} = \pm\frac{\omega}{c}\sqrt{\frac{\varepsilon_1\varepsilon_2}{\varepsilon_1+\varepsilon_2}}, \tag{1.40}$$

and

$$\begin{aligned} k_{1z} &= \pm\frac{\omega}{c}\sqrt{\frac{\varepsilon_1^2}{\varepsilon_1+\varepsilon_2}}, \\ k_{2z} &= \pm\frac{\omega}{c}\sqrt{\frac{\varepsilon_2^2}{\varepsilon_1+\varepsilon_2}}. \end{aligned} \tag{1.41}$$

From the above equations, several additional conditions for the surface plasmon mode can be deduced. First of all, only TM polarization mode can excite SPPs. Second, in order to obtain a bound mode along the z axis, the normal wave vectors (k_{1z}, k_{2z}) have to be imaginary for exponentially decaying solutions. Thus, $\varepsilon_1+\varepsilon_2$ must be negative based on equation (1.41). Thirdly, in order to obtain the propagating mode along the interface, the horizontal wavevector (k_x) has to be real. Thus, $\varepsilon_1\varepsilon_2$ must be negative as well based on equation (1.40).

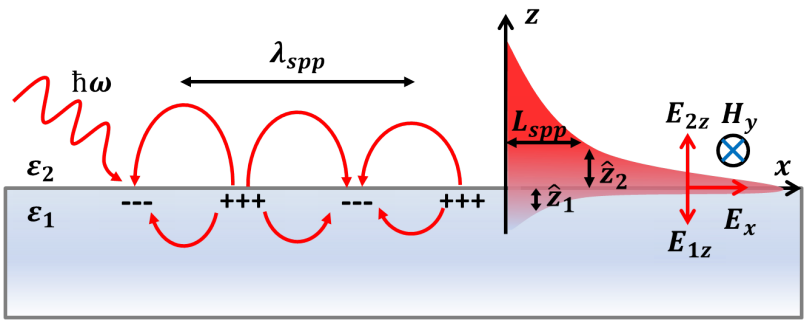

Fig. 1.12 The scheme of SPPs propagating along the interface with some important parameters. The oscillation of density states at the metal surface results in the propagating SPPs with a wavelength λ_{spp} which has three components of field E_x, H_y, E_z. The energy loss of this evanescence wave has three parameters to quantify, which are propagation length L_{spp} and penetration lengths $\widehat{z}_1$ and $\widehat{z}_2$.

Now we will discus some properties of SPPs by using the above results. As we known, for noble metals, the losses associated with electron scattering (ohmic losses) [52] results from the imaginary part of $\varepsilon_1 = \varepsilon_1' + i\varepsilon_1''$. Assuming that $\mid \varepsilon_1' \mid \gg \varepsilon_1''$ and ε_2 is a real number, the real part k_x' and the imaginary part k_x'' in the complex parallel wave number $k_x = k_x' + ik_x''$, which propagates along the positive direction of x axis, can be expressed as:

$$
\begin{aligned}
k_x' = k_{spp}' &= \frac{\omega}{c}\sqrt{\frac{\varepsilon_1'\varepsilon_2}{\varepsilon_1'+\varepsilon_2}}, \\
k_x'' = k_{spp}'' &= \frac{\omega}{c}\left(\sqrt{\frac{\varepsilon_1'\varepsilon_2}{\varepsilon_1'+\varepsilon_2}}\right)^3 \frac{\varepsilon_1''}{2\varepsilon_1'^2}.
\end{aligned}
\tag{1.42}
$$

The real part k_x' determines the SPP effective index n_{spp} and the SPP wavelength λ_{spp} which are expressed as:

$$
\begin{aligned}
n_{spp} &= \frac{k_{spp}'}{k_0}, \\
\lambda_{spp} &= \frac{2\pi}{k_{spp}'} = \frac{2\pi}{k_0 n_{spp}}.
\end{aligned}
\tag{1.43}
$$

According to the previous measurement of the properties of noble metals [47], these two parameters of SPPs at the air/gold interface with the excitation wavelength $\lambda_0 = 633$ nm were determined as $n_{spp} \simeq 1.05$ and $\lambda_{spp} \simeq 603$ nm. These values here are important for the SPP observation and analysis because this excitation wavelength (He-Ne red laser) is mainly used in our experiment. The SPP propagation length L_{spp} which defines the exponential damping distance of the electric field amplitude can be determined by the imaginary part k_{spp}'' as:

$$
L_{spp} = \frac{1}{2k_{spp}''}. \tag{1.44}
$$

The SPP propagation length is measured around 10 μm at the air/gold interface with the same incident 633 nm wavelength. The last thing to mention here is the SPP decay length or penetration length along z axis $\widehat{z} = 1/k_z$ which defines the capacity of energy confinement along the normal direction. The expressions of the decay length in two media are deduced as:

$$
\begin{aligned}
\widehat{z_1} = 1/k_{1z} &= \frac{c}{\omega}\sqrt{\frac{|\,\varepsilon_1'+\varepsilon_2\,|}{\varepsilon_1'^2}}, \qquad z<0 \\
\widehat{z_2} = 1/k_{2z} &= \frac{c}{\omega}\sqrt{\frac{|\,\varepsilon_1'+\varepsilon_2\,|}{\varepsilon_2^2}}. \qquad z>0
\end{aligned}
\tag{1.45}
$$

As known $|\,\varepsilon_1'\,| \gg \varepsilon_2$, the decay of SPP into the noble metal is much shorter than into the dielectric such as air and glass which could be observed directly in using a scanning

tunneling optical microscope [53]. Thus, the decay length in the air part and in the gold part are measured as 421 nm and 23 nm respectively for $\lambda_0 = 633$ nm. The decay length in air part gives the distance at which SPPs may interact with their environment and particularly with optical emitters such as quantum dots [54–56], or nanodiamonds [57–59], placed close to the metal surface. The decay length in gold part indicates that if the gold film is thinner than 20 nm, SPPs may react with SPPs at the interface on the other side of the film. What if the three dimensions of the metal are all closed to 20 nm i.e. nanoparticles, it shows several unusual effects called localized surface plasmons [60–62]. The electric fields near the particles' surface are dramatically enhanced and the optical absorption of particles has a maximum peak occurred at visible wavelength. In our experiment, the major part is focused on delocalized or propagating surface plasmons depicted in Figure 1.12.

1.2.3 Excitation of surface plasmon polaritons

After understanding the properties of SPPs, we have to find an efficient way to excite SPPs to fulfill both energy and momentum conservation. Now we plot the SPP dispersion relation based on Equation (1.40) in Figure 1.13. However, the SPP dispersion curve always lies to the right of the light line of the dielectric. It means that the direct excitation with light is not possible unless some special coupling techniques are employed for the phase-matching. Like coupling in conventional dielectric waveguides, some techniques are very similar such as prism coupling, grating coupling etc.

Prism coupling is a very efficient way to excite SPPs by introducing a three-layer system. The light cone of prism has shifted to the right (multiply by $1/n_{prism}$) because the prism layer has a dielectric constant $\varepsilon_{prism} > \varepsilon_{air}$. A beam reflected at the interface between the prism and metal will generate an in-plane momentum $k_x = k_0 n_{prism} \sin\theta$ associated with a leaky wave, which is sufficient to excite SPPs at the metal/air interface. The SPP wavevector between two light lines under the green arrow can be excited. Here we mention that no SPPs are excited at the metal/prism interface because the SPP dispersion at metal/prism still stay on the right of the light line of prism which is not plotted in Figure 1.13.

Two classic geometries for prism coupling methods introduced by Kretschmann and Otto are depicted in Figure 1.14. The Kretschmann configuration [38] is a contact method which means that a thin metal film is evaporated on top of a glass prism. If a laser impinges from the prism side on the interface with an incident angle larger than the critical angle of the total internal reflection, a tunneling effect [63] of the field involves and pass through the metal thin film. Therefore the attenuated photons excite SPPs at the metal/air interface. Another configuration was proposed as a non-contact method by Otto [37]. A thin air gap separates the metal film and the glass prism. Similarly, total internal reflection occurs at the prism/air

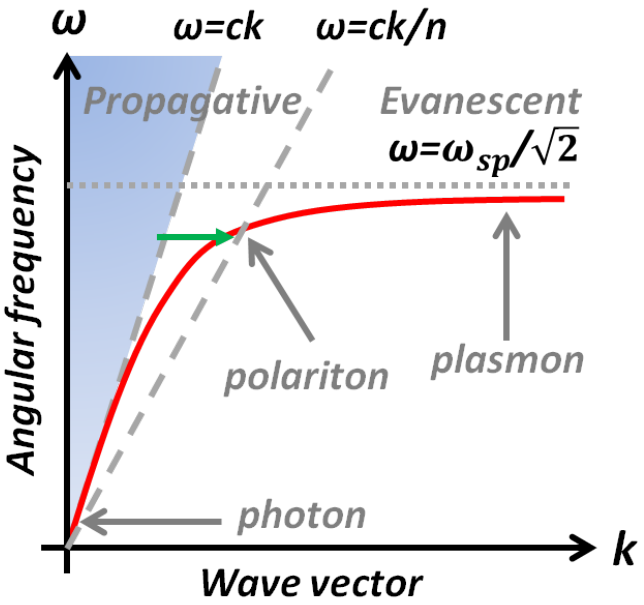

Fig. 1.13 SPP dispersion relation at air/gold interface indicated by the red curve. At the beginning of this curve, SPPs are similar the photon and they show more properties like polaritons with increasing the frequency. Once the frequency almost reaches the limit indicated by horizontal grey dashed line, they work like plasmon in the bulk. The grey dashed line on the left represents the light line of air and the propagative light exist only on the left side. The grey dashed line on the right represents the light line of the prism. The prism light cone shifts to the right which means it exist the suitable propagation constant k to excite SPPs below the intersection of two curves pointed by the green arrow.

interface instead of the prism/metal interface. But the same tunneling effect take places and the leaky wave excites SPPs at the air/metal interface. The Kretschmann geometric provides a precise way to determine the dispersion relation by observing the reflected light with changing the incident angle. The Otto geometric provides a possibility to excite SPPs without undesirable direct contact.

Grating coupling respects the same principle as coupling the light into waveguides which provides an additional reciprocal vector of the grating indicated as the green arrow in Figure 1.14. The grating pattern can include either slits, ridges, protrusions or holes with an appropriate period under the condition $k_{spp} = k_0 \sin\theta \pm n\frac{2\pi}{\Lambda}$, where n is an integer and Λ is the period. Note that the reverse process also works which means that the grating is used to couple out SPPs as a radiated light. The grating geometric such as depth, shaped asymmetric groove, etc. can influence the coupling efficiency [64, 65] and even the propagation direction which we will be quickly reviewed in the next section. Besides, some other coupling techniques depicted in Figure 1.14 like surface imperfection excitation [66] (a particle or

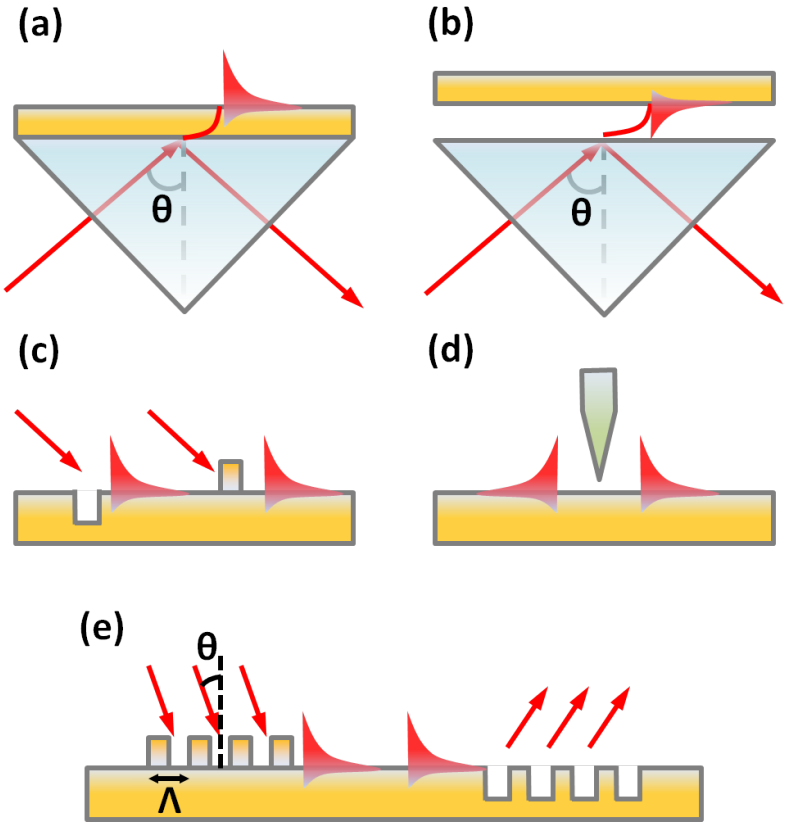

Fig. 1.14 Configurations of SPP coupling techniques. Two configuration of SPP excitation by prism couplings of Kretschmann (a) and Otto (b). The angle θ determines the SPP propagation constant k_{spp}. (c) The surface imperfection such as holes, ridges, protrusions, slits or grooves can excite SPPs due to the diffraction. (d) Near field excitation such as scanning near field microscope (SNOM), scanning tunneling microscope (STM) is also possible to excite SPPs by generating evanescence waves from the apex of a extremely fine tip. (e) Grating coupling is an alternative method for exciting SPPs which has a large number of applications by shaping the grating geometric. θ and Λ denote the incident angle and the period of the grating.

a hole in nanometer) and near field excitation (SNOM, STM) [67, 68] can be both excited SPPs as well based on the different requirements.

1.3 Directionality of scattering and SPP launching

In this section, I specifically present state of the art in directional scattering and directional SPP lauching. As we known, by shaping the structure of a metallic surface, the properties of surface plasmon polaritons can be tailored by light-matter interaction which offers the poten-

tial for developping new types of photonic devices in various domains such as subwavelength optics, data storage, light generation, high resolution microscopy, bio-photonics, etc. [26]. Thus, how to efficiently steer and control the flow of SPPs became a key issue in the research of SPP circuitry [27]. In order to enhance the signal propagation while reducing the energy injected in the unwanted direction, the directional scattering of light and directional SPP launching attracts a lot of interest. There are two kinds of directionality assorted as out-plane and in-plane control in Figure 1.15. The out-plane directional control aims at concentrating the light emission with a narrow beaming angle by transmission via a metal patterning surface [69]. The extraordinary transmission through a sub-wavelength hole array [42] paved a way to this research. The apertures such as a slit surrounded by parallel grooves [70–72] or a single circular aperture surrounded by concentric rings [73, 69, 74] have realized the beam focusing as a consequence of SPPs re-emitted angle governed by the aperture period. On the contrary, the in-plane directional control has more various configurations which lead unidirectional scattering on the sample plane with a normal illumination. The advantage is to direct the signal to a specific region so as to get rid of the noise of the source. In the following two sections, two methods of in-plane directional control will be introduced.

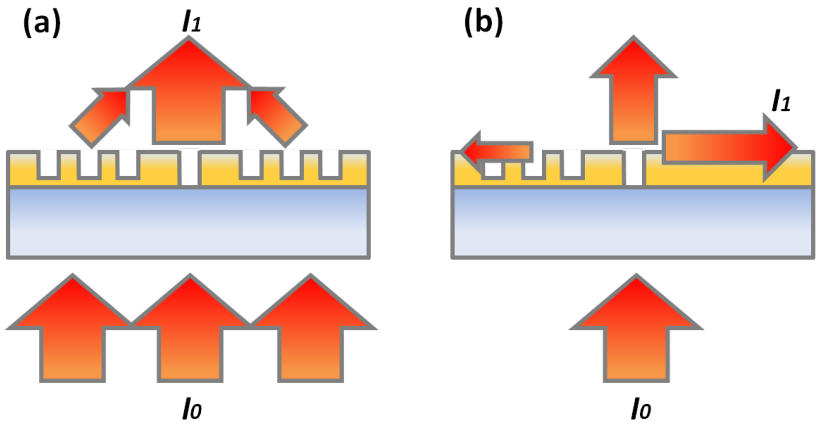

Fig. 1.15 Out-plane and in-plane directional cotrol of light. Light illuminates the back side of metal structures deposited on the glass substrate. (a) After tunneling through the aperture, the energy in the SPP field is scattered into the far field with a convergent beam (I_1) on the other side so called out-plane control. (b) The intensity of scatted light propagates along a specific direction on the film surface (I_1) called in-plane control.

1.3.1 Unidirectional scattering by the metal structuration

At the first stage, the directional propagation was realized by using in-plane Bragg mirrors [75, 26]. The corrugated structure leads SPPs to pass or to be reflected depending on

its periodic distance. When the period of the nanostructure is half that of the effective wavelength of the SPP mode, SPPs may be prevented from travelling in this direction called SPP photonic bandgap [75]. The explanation can be understood by the Bragg scattering conditions [76]. Destructive or constructive interference should take place for the total phase difference ($\Phi = 2k_{spp}\Lambda$) equal to odd or even multiples of π. Once the period of the reflector corresponding to a phase for the destructive interference, SPPs will be mainly backscattered. Many successful nanostructures serving as Bragg reflectors were reported in ref. [77–79]. According to the phase-matching of patterned structures, a variety of methods such as Yagi-Uda antennas [4–7], tilted-angle illumination of slit [8], single V-antenna [9], asymmetric grooves (different depth or different length) [80, 10] etc. depicted in Figure 1.16 have been developed in the last ten years.

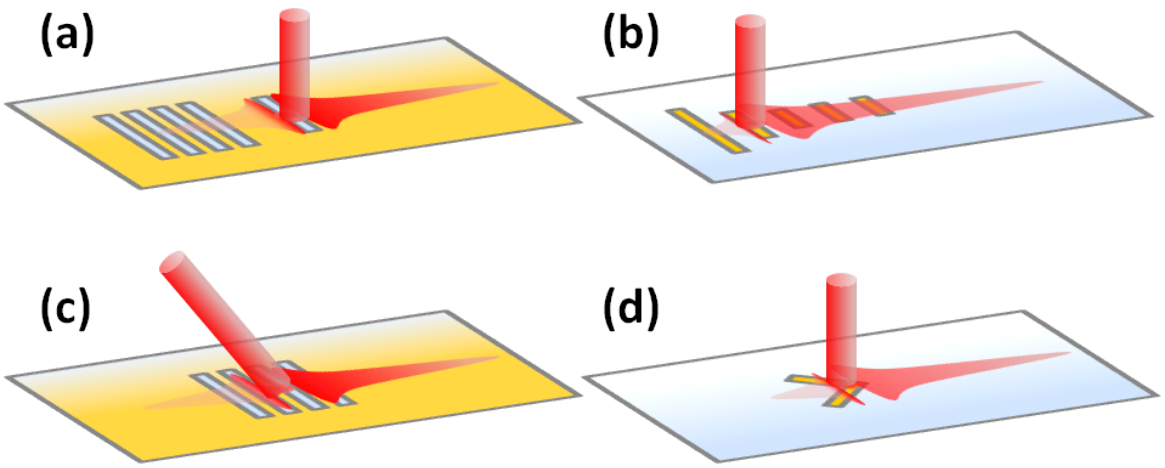

Fig. 1.16 Configurations of 4 methods for unidirectional scattering. (a) A simple Bragg reflector consists a slit to excite SPPs propagating to left and right sides of it and the slit array serves as the Bragg mirror. (b) Yagi-Uda antennas works when the second ridge called the feed is excited by the laser. The longest ridge called reflector lead the light to the right side. (c) If the illumination on the slit array has a tilted angle with the normal incident light, the unidirectional scattering occurs. (d) V-shaped metallic antenna shows high unidirectional side scattering with a broadband of incident wavelength.

1.3.2 Spin-controlled tunable directional coupling of SPPs

Owing to the limit for a fixed direction which is determined by the structures, the tunable directional coupling of SPPs controlled by the spin states of light (circular polarization) is subsequently being developed such as spin-controlled incident tilted angle on the slit [81], T-shaped subwavelength apertures [11], L-shaped slots [10] and V-shaped slot antennas

[12, 13]. Two types of spin-based directional coupling of SPPs will be reported in this thesis. One is unidirectional coupling which means that SPPs propagate to the left or right side depending on the spin states of light (Fig 1.17 (a)). The other one is radial directional coupling which means that SPPs propagate to the center of a ring-like structure controlled by the spin states (Fig 1.17 (b)). In this case, optical vortex beams can be generated which is shown in Fig 1.17 (d) as an example.

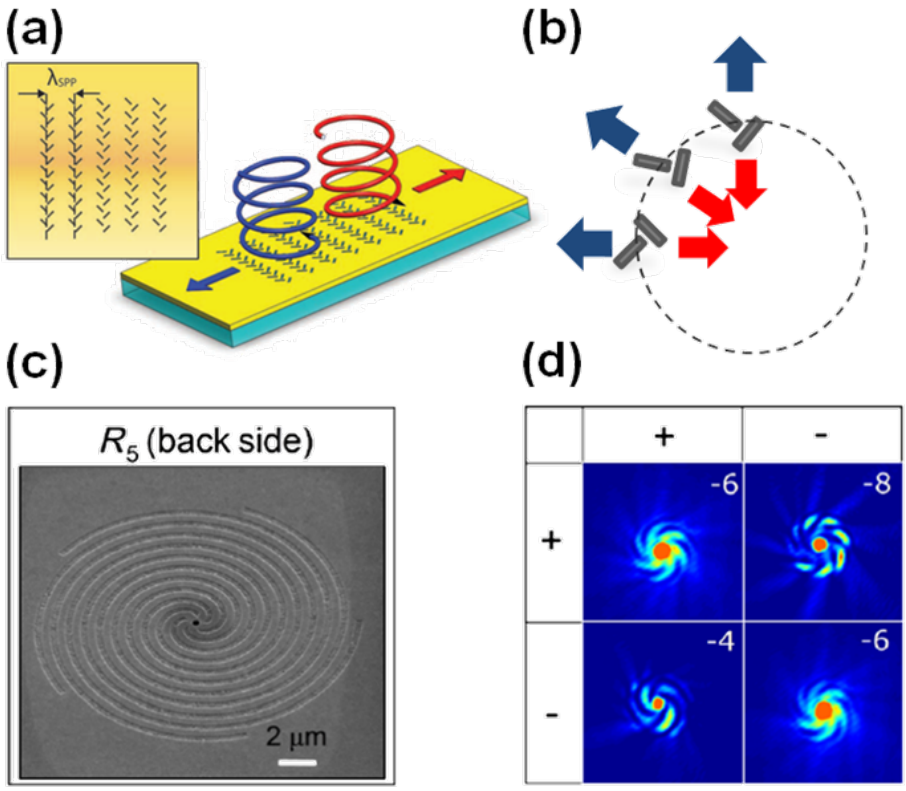

Fig. 1.17 Spin-controlled directional coupling and vortex generation. (a) One type of subwavelength aperture which provides controllable spin-direction coupling between light and SPPs [11]. (b) One type of ring-like aperture which realizes the inward or outward directional coupling controlled by spin states of light. (c) Spiral structures with 5 arms provides the spin-based generation of optical vortex beams. (d) Intensity distributions measured through the structure in (c) [82]. + and − represent two spin states of input and output signals. Four images show the vortex beams with different number of orbital angular momentum.

The mechanism results from the spin-orbit interactions within SPP scattering by nanostructures. Light carries both spin and orbital angular momentum. Spin angular momentum (SAM) reflects the handness of circular light polarization. Orbital angular momentum (OAM) is associated to the helical wave fronts of light beam. As we known, spin Hall effect leads to

the separation of electrons with opposite spins in different trajectories perpendicular to the electric current flow. As an optical analogue, spin and orbital properties become strongly coupled with each other when passing through a structured surface. The spatial symmetric break may result that the opposite spins separate in two opposite directions after interacting with metasurfaces [83, 84]. However, the mechanism about spin-based directional SPP generation with different structures and the quantification of this effect still remain unclear in some part and we will thoroughly discuss it again in the chapter 4. With deep investigation, we believe this effect will offer an important link for optical information processing [85], quantum optical technology [86], topological surface metrology [87] and particle trapping [88, 89].

As a conclusion, the basic mechanism and properties about both the guided waves and SPPs are well explained in this chapter. The understanding of these two kinds of confined waves provides us the necessary parts for the future study about how to control them efficiently. Finally, we introduce several recent methods for the directional coupling of the light so as to find the current problems and to improve them. In the next chapter, we are going to describe the details of our sample preparation. The well-prepared sample will be used for our systematical investigation about the directional generation of two confined waves.

Chapter 2

Sample preparation

Abstract: Two parts about sample preparation are introduced in this chapter. The waveguide fabrication is firstly explained by three steps which contain the sol-gel process, thin film deposition and characterization of the TiO_2 waveguides. Then, we present the methods for patterning of nanostructures which are the Focused Ion Beam (FIB) milling for the slits on the gold film and the Electron Beam Lithography (EBL) for the gold strips on the waveguide. Lastly, the sample gallery shows all the structures developed during my PhD work and some preliminary results.

Contents

2.1 Waveguide fabrication and characterization

With the rapid development of fabrication techniques, optical waveguides can nowadays be fabricated using a large class of materials such as glass, polymers, metals or semiconductors. Aiming at investigating optical properties of plasmonic structures on waveguides, a planar thin film of titanium dioxide (TiO_2) was chosen as a good candidate for our research. Actually,

titanium dioxide has been widely used in several domains such as photocatalysis, optical coatings, solar cell applications and so forth [90–92]. In addition, thanks to its high refractive index and transparency at visible wavelengths, it becomes a promising dielectric waveguide for integrated optics [93]. In this section, the TiO_2 sol-gel process is firstly introduced. The dip-coating method for the thin film waveguide fabrication is then explained and it ends up with the characterization method for measuring the thickness and the effective refractive index of TiO_2 waveguides.

2.1.1 Sol-gel process

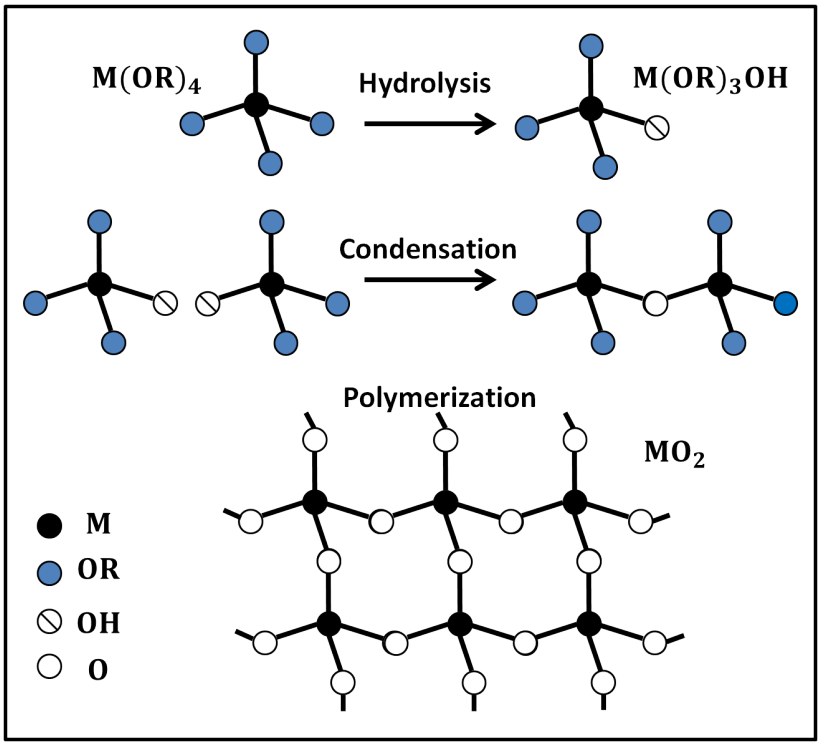

Fig. 2.1 Reactions involved in sol-gel process [94]. M represents a metal with 4 covalent bonds like titanium. OR is an organic group of an alcohol bonded with a negative charge. The hydrolysis leads metal alkoxides drop the group OR away by replacing the group OH. In acid or neutral environment, condensation and polymerization take place with the hydrolysis process.

The sol-gel process is a cheap and low-temperature method for producing solid metal oxides such as silica and titanium dioxide from small molecules [95]. It has several applications in optics, electronics, biosensors and medicine, since it allows us to produce different types of metal oxides such as monolithic, thin film, powder and so forth by corresponding processing [96]. The principle involves the conversion of a metal alkoxides (precursors) which is a

colloidal solution (sol) into a gel-like polymer network. The sol-gel process consists in a series of hydrolysis, condensation reaction of a metal alkoxide and polymerization [97]. These reactions are depicted in Figure 2.1 [94].

The experimental procedure of TiO_2 solution fabrication is summed up in Figure 2.2 [94]. Firstly, a small amount of isopropanol is added into the precursor Titanium isopropoxide to provide an alcoholic environment. Secondly, the chelating agent namely acetic acid is slowly dripped into the precursor and generates water with isopropanol while the hydrolysis and condensation start [98]. Thirdly, after adding the methanol solvent, the transparent TiO2 solution is formed and stays in a stable state for at least one day. Note that the TiO2 solution is filtered by the diameter smaller than 1 μm before the thin film deposition.

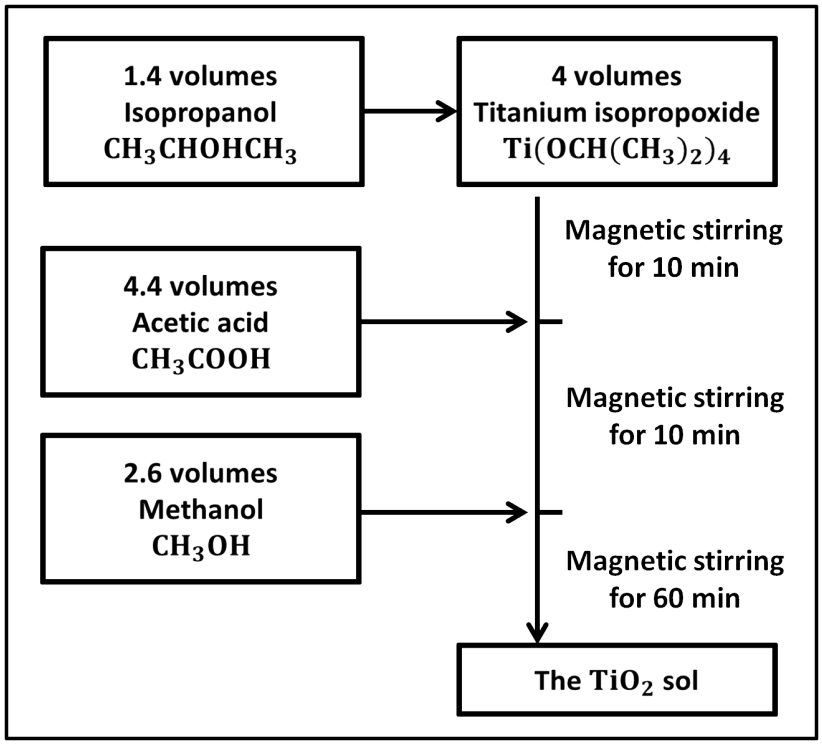

Fig. 2.2 Experimental process of TiO_2 solution fabrication. This chemical process refers from the thesis of Clément Bonnand [94] and is slightly modified for solution volumes in order to optimize the quality of solutions.

2.1.2 Thin film fabrication

After having the sol-gel solution of TiO_2, we will talk about the process of thin film deposition. In fact, a thin film serves as a layer of material with a thickness ranging from several nanometers to micrometers. The precise control of layer thicknesses allows us to

adapt thin films to different requirements. With the development of advanced deposition techniques during the 20th century, thin film broadens the application in various areas such as semiconductor devices, optical coatings, magnetic storage, pharmaceuticals and so forth [99–103]. The deposition techniques include thermal evaporation, sputtering, pulsed laser deposition, chemical vapor deposition, spin or dip coating and so forth. Here, dip coating is adopted to realize the fabrication of sol-gel thin film with high quality. Basically, the process of dip coating is separated into three stages:

1. Immersion and dwell time: the clean glass substrate is immersed into the filtered TiO_2 solution at a constant velocity (4.5 cm/min) and followed by a dwell time (5s) in order to leave sufficient interaction time of the substrate with the coating solution for a complete wetting.

2. Deposition and drainage: the thin film is entrained by capillary force once the substrate starts being pulled at the same velocity called drawing velocity (4.5 cm/min) out of the coating solution. The excess liquid will be drained from the surface back to the precursor solution. The drawing velocity, the viscosity of the solution and the concentration of TiO_2 are the main factors for controlling the thickness of the thin film.

3. Evaporation: the substrate is kept immobile for 1 min so that the solvent is evaporated. Subsequently, the substrate is heated at 350°C for 15 min in the furnace with Oxygen flow in order to burn out the residual organics and induce further polymerization [104].

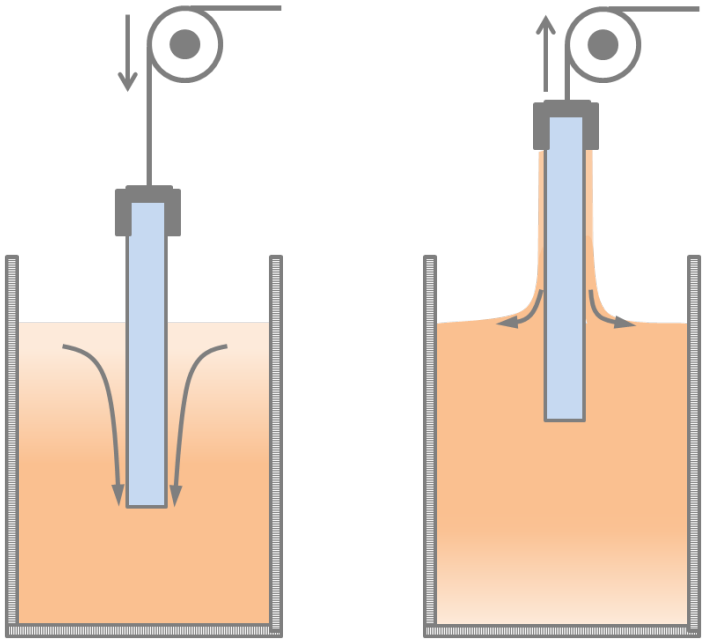

Fig. 2.3 Principle of the dip coating techniques. The left and the right images show separately the immersion step and drainage step during dip coating process.

These three stages can be repeated several times depending on the expected thickness of thin film waveguide. The thickness of each coating layer is only controlled by the drawing velocity because this factor is relatively easier to change than the others such as the concentration and the viscosity of the solutions. The higher velocity we have, the thicker film will be but with more defects in the coating layer. After trading off thickness and quality of films, the velocity of 4.5 cm/min is chosen. Similarly, heat-treatment procedure shows a strong influence on the flims' morphology [105]. The longer and higher heat treatment is taken, the higher refractive index the film has because the densification could be completely finished and organic residues could be better removed [106]. However, higher temperature and longer time also lead to generation of cracks. Eventually, the lower temperature at 350°C is fixed at 15 min to compromise quality and refractive index of films.

2.1.3 Characterization of waveguides

Light propagation in the waveguide layer strongly depends on optogeometric parameters such as refractive index and thickness of thin planar waveguide films. Therefore, both of these characteristics have to be carefully checked. M-lines spectroscopy is an accurate and nondestructive method for the measurement of these two parameters[21, 107, 108]. Prism coupling of the laser light to a planar waveguide is the core of this technique. Once the incident angle is equal to the angle of the m-th guided mode, a strong coupling appears as a back line appearing on the screen (see in Figure 2.4). Based on the equation (1.23) $N_m = n_p \sin(\alpha + \arcsin(\frac{\sin\theta_i}{n_p}))$, each incident angle corresponding to the excited guided mode leads us to determine a corresponding effective index with known the foot angle α and refractive index of prism n_p. Now let's remind the dispersion relations (1.19) and (1.20) in waveguides for TE and TM modes respectively:

$$\begin{aligned}
\frac{2\pi}{\lambda_0} d\sqrt{n_1^2 - N_m^2} &= \arctan\left(\sqrt{\frac{N_m^2 - n_2^2}{n_1^2 - N_m^2}}\right) + \arctan\left(\sqrt{\frac{N_m^2 - n_3^2}{n_1^2 - N_m^2}}\right) + m\pi, \\
\frac{2\pi}{\lambda_0} d\sqrt{n_1^2 - N_m^2} &= \arctan\left(\frac{n_1^2}{n_2^2}\sqrt{\frac{N_m^2 - n_2^2}{n_1^2 - N_m^2}}\right) + \arctan\left(\frac{n_1^2}{n_3^2}\sqrt{\frac{N_m^2 - n_3^2}{n_1^2 - N_m^2}}\right) + m\pi.
\end{aligned} \tag{2.1}$$

In our case, the superstrum is the air with index $n_3 = 1$ and the glass substrate with index $n_2 = 1.52$ is used for the thin film waveguide deposition. So far, as long as the film is thick enough to support more than two modes with the same polarization (TE or TM), the equations above allow us to determine two unknown parameters (thickness d and refractive index n_1 of waveguides).

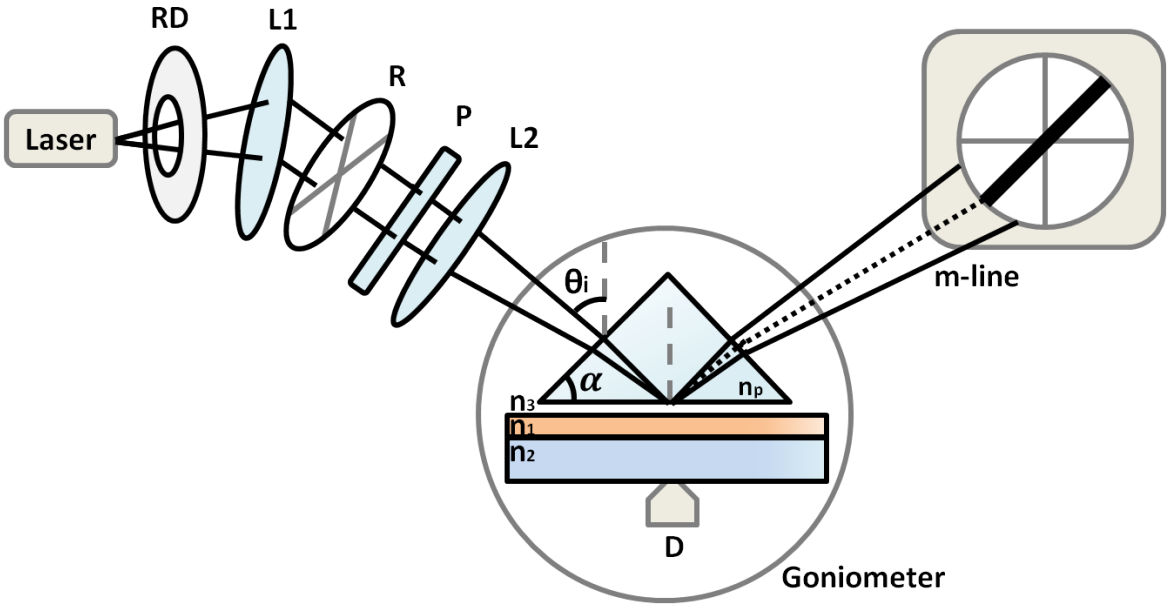

Fig. 2.4 M-lines spectroscopy set-up for characterizing optogeometric parameters of waveguides. The prism and waveguide sample is fixed on the grey circular stage of gonimeter. The angular position is measured by the superimposition of dark lines and the reticle image on the screen.

In the experimental measurement, an isosceles prism in rutile (TiO_2) with foot angle $\alpha = 59.92^\circ$ is used as indicated in Figure 2.1. The refractive index of the prism (n_p) has a slight variation with different incident wavelengths and polarization. The relation is shown below referring to [109].

$$\begin{aligned} n_p^2 &= 7.197 + 3.220 * 10^7/(\lambda^2 - 0.843 * 10^7), \qquad TE \quad mode \\ n_p^2 &= 5.913 + 2.441 * 10^7/(\lambda^2 - 0.803 * 10^7), \qquad TM \quad mode \end{aligned} \tag{2.2}$$

where the wavelength λ is in Angstroms. The Helium-Neon laser with $\lambda = 632.8$ nm is chosen for our measurement. Thus, the refractive index of prism can be determined and we get $n_p = 2.866$ for TE and $n_p = 2.584$ for TM mode respectively. Figure 2.4 describes the set-up for the m-lines spectroscopy. The laser beam passes firstly through a rotating polymer disk (RD) in order to reduce the speckle effect and suppress the polarization of the laser light. The collimated beam after the first lens (L1) passes a reticle which is used as the reference of laser beam and will be finally projected on the screen. The polarizer (P) on the way of the collimated beam works for controlling the polarization state for an appropriate TE or TM mode. The second lens (L2) focuses the beam into the prism with an incident angle θ_i so that

the beam spot coincides with a coupling spot, which is the point where the clamping screw (D) presses the film against the prism. The screw D helps to modify the air gap size between the prism and the waveguides to which the coupling efficiency is sensitive. Once two layers with different darkness on the screen corresponding to the interface between the film and the substrate has been seen, we stop screwing and mark the interface line. Note that the pressure has to be imposed gently to avoid deformations or cracks in the film. This superimposed point on the prism is fixed at the center of a circular stage attached to a precision goniometer (resolution $5''$) [110]. After calibration of the zero angle of the goniometer with the help of a normal incident beam, the goniometer starts to rotate and the θ_i is recorded when a dark line appears in the center of the reticle marker on the screen. A dark line appears on the screen only when the laser beam is coupled to the film and excites a propagative mode with $\theta_i = \theta_m$. In this situation, the images of dark lines attribute to the frustrated total internal reflection which correspond to the guided modes coupled in the waveguide.

According to the angles recorded by the goniometer, a program is used to solve the equation (2.1) with corresponding polarization modes. One of the experimental results is shown in Figure 2.5. Note that at least two modes for each polarization are necessary to solve the equations. That is to say the tested waveguide has to be thick enough and to make sure at least four modes inside. The sample shown in Figure 2.5 (a) is fabricated with 7 layers of dip-coating film. The thickness $d = 434$ nm and refractive index of TiO_2 $n_1 = 1.96$ are obtained which correspond to the grey solid line in Figure 2.5 (b). The existing modes in this waveguide are also plotted in Figure 2.5 (b) (effective refractive index versus thickness of waveguide) based on the dispersion relation (equation (2.1)). To illustrate the principle, two TE modes and two TM modes are shown with $N_{TE0} = 1.90$, $N_{TE1} = 1.70$, $N_{TM0} = 1.88$ and $N_{TM1} = 1.65$ respectively. Intuitively, TE modes always come firstly with increasing the thickness of waveguids and in the same order of modes, effective index of TE modes is always higher than TM modes for a given thickness. Besides, we observe only one mode for TE and TM if the waveguide is thinner than 300 nm and we can not directly measure the thickness. Thus, we calculate every layer thickness of the waveguide by measuring guided modes of 6, 7 and 8 layers assuming each dip-coating layer has the same thickness. As we known, if we need the results to be more precise, more modes have to be guided in the system but it means that we have to fabricate more than 10 layers of TiO_2 thin film. However, more time for the heating treatment generates a large number of cracks and thicker film is not necessary for the experiment. It is the reason why we decide to measure only the thickness from 6 to 8 layers.

The thickness of each layer is determined to be 61 nm in average with ± 5 nm tolerance. The 4-layer sample, which will be used for our study, is evaluated to be around 240 nm

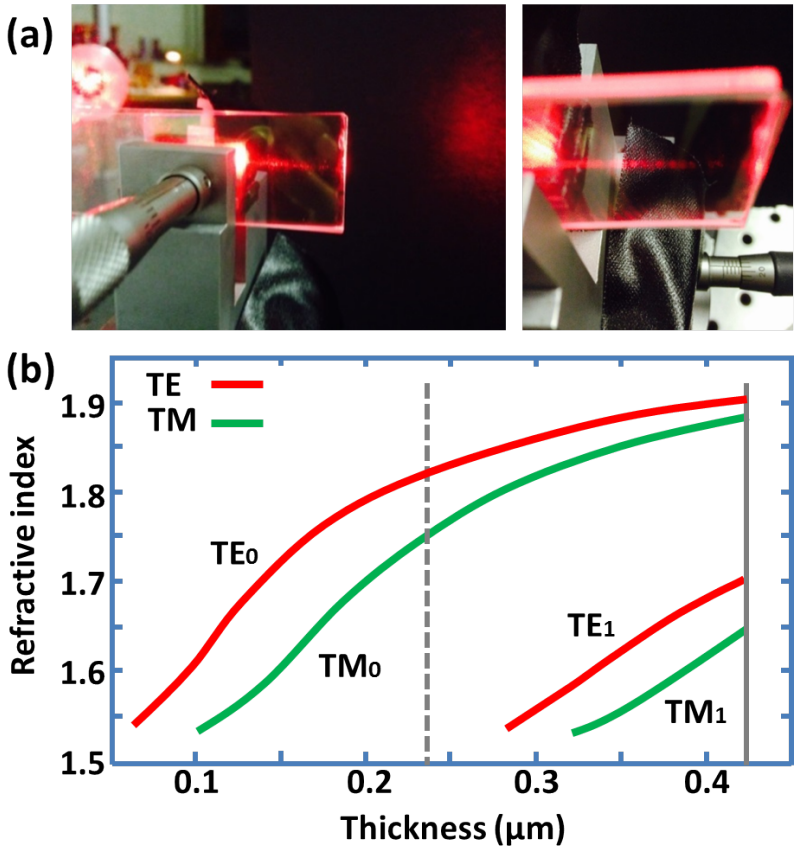

Fig. 2.5 Waveguide characterization results. (a) The laser light was coupled into the waveguide with 7 layers of TiO_2 film. The guided mode can be easily observed propagating until the end of waveguide. The screw is used to adjust the distance of air gap for coupling indicated as D in Figure 2.4. (b) The red and green curves are plotted according to the theoretical equation which shows the relation between effective refractive index and film thickness.

thick marked as the grey dashed line in Figure 2.5 (b). Only 1 TE and 1 TM modes were observed with $N_{TE0} = 1.83$ and $N_{TM0} = 1.75$. Here, we quickly discuss the uncertainty of the measured results. The uncertainty includes two parts which are the systematic error and the practical error during thickness measurement for each layer. The systematic error for effective refractive index measurement can be derived using the following equation:

$$\triangle N_m = (\frac{\partial N_m}{\partial \theta_i}) \triangle \theta_i + (\frac{\partial N_m}{\partial n_p}) \triangle n_p + (\frac{\partial N_m}{\partial \alpha}) \triangle \alpha, \tag{2.3}$$

where $\triangle\theta_i$, $\triangle n_p$, $\triangle\alpha$ denote uncertainties of angle measurement in goniometer, measurement of the refractive index and foot angle of the prism, which are all known as 1/100. Thus, the systematic uncertainties are 10^{-4} for N_m and 3 nm for the thickness. However, an error which comes from the thickness measurement of each layer has to be accounted. The

slightly different thicknesses of each layer result in this error. Finally, we deduce that the waveguide thickness of each layer is 61 nm $\pm$8 nm which is within the tolerance of our study.

2.2 Nanopatterning of metals

Thanks to a large number of researches on nanotechnology in the past decade, several powerful techniques have been widely developed for precise analysis of nanostructures and manipulation in nanoscale, such as scanning electron microscopy (SEM), transmission electron microscopy (TEM), atomic force microscopy (AFM) and focused ion beams (FIB). With huge demand of the miniaturization of structures, devices and systems down to the atomic scale, FIB and Electron beam lithography (EBL) have become good candidates as nanofabrication techniques especially for metals. FIB is considered as a very efficient tool for material milling due to its versatility and configurational flexibility [111]. EBL is an opposite process which means to deposit materials on the substrate at the nano scale. In our study, the nano-apertures on the gold film and nano-antennas on the waveguide are introduced to study the directionality. Thus, FIB and EBL are both used for our sample fabrication. Here, we introduce the principles of FIB and EBL as well as the procedure of sample fabrication. Finally, we will illustrate the tested samples fabricated by FIB and EBL in the sample gallery.

2.2.1 Focused ion beam milling

The focused ion beam (FIB) has gained widespread use in both fundamental material studies and technological applications over the last several years because it offers not only the high-resolution imaging [112] but also the flexible nanostructuration. The FIB instrument is quite similar to scanning electron microscopy (SEM), with the only difference that FIB contains an ion beam for rastering over the sample instead of an electron beam. The secondary electrons sputtered out by interaction with ion beam like electron beam imaging are used to obtain high-spatial-resolution images. Furthermore, ion beam can also remove materials from the sample so-called FIB milling or sputtering because the momentum of ions are much higher than electrons. On the contrary, if precursor-gas-injection sources are introduced, the FIB can also work for deposition. The versatility and multifunctionality of the FIB show the potentials in a large number of applications including TEM specimen preparation [113], defect tomographic analysis [114], micromaching for MEMs [115], nanostructuration for integrated device [116, 117], FIB-assisted chemical vapor deposition [118] and so forth.

Concerning the most important function of the FIB, milling is preferred for especially hard materials such as metals, glass, ceramics with hard substrates such as silicon, glass,

ceramics but it is not very precise for soft materials due to their distortion and damage during the strong beam focusing. Most modern FIB instruments are integrated with an additional SEM column depicted in Figure 2.6 (a) so that the instrument becomes a more versatile dual-beam platform for material removal and imaging at the same time.

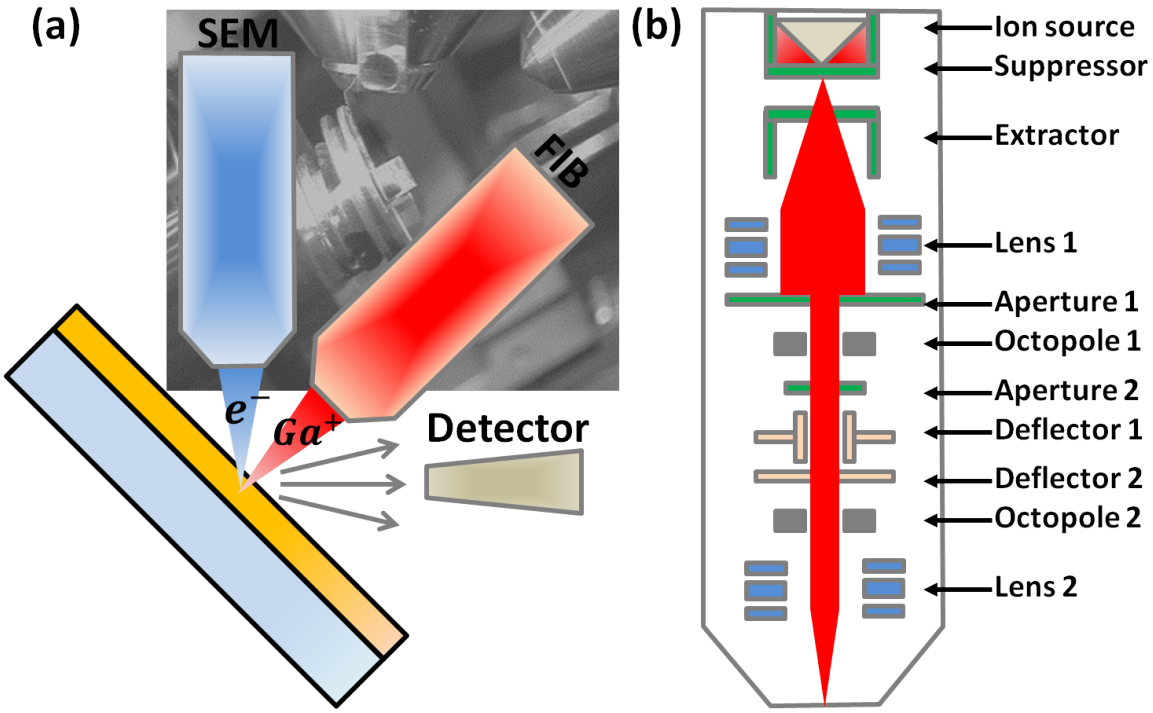

Fig. 2.6 Schematic illustration of the FIB instrument. (a) Two columns of SEM and FIB. The secondary electrons or secondary ions generated from the interaction between beam and sample materials can be collected by a biased detector for imaging. The background image is taken from the chamber camera for position inspection. (b) A schematic diagram of a FIB ion column. A vacuum of about 10^{-7} mbar is maintained inside the column.

In most commercial systems, Gallium (Ga) ions are used and the focused beam of Ga ions is generated from a liquid metal ion source [119] by the application of a strong electric field. A schematic illustration of the working principle of FIB is shown in Figure 2.6 (b). The positive charge of Ga ions on the tip of a tungsten needle excited by this electric field can be emitted through the suppressor and extractor system. A typical extraction voltage is 7000V and a normal extraction current is around $2\mu A$ [120]. The first three-element electrostatic lens focuses the emitted ions into a beam and determines the beam pattern. A refinement of the beam size has been done through the first aperture. The first octopole then adjusts the beam astigmatism in order to control the internal alignment of the beam. The ion beam energy is typically between 10 and 50keV, with currents varying between 1pA and 10nA [120]. The second aperture is a group of variable apertures with different

diameter sizes which is used to adjust the beam current for expected functions for example a narrow beam for high-resolution imaging and a strong beam for fast and rough milling. Beam blanking consists of a blanking deflector and an aperture deflector which is useful to protect specimens from constant milling [121]. The second octopole serves as scanning and shifting as well as astigmatism correction of the ion beam. Finally, with the presence of the second three-element electrostatic lens, the beam can be focused to a very small spot with a high resolution in the range of 10nm. Thus lines, circles, rectangles and stepped profiles can be milled by the consecutive beam spot shown in Figure 2.7.

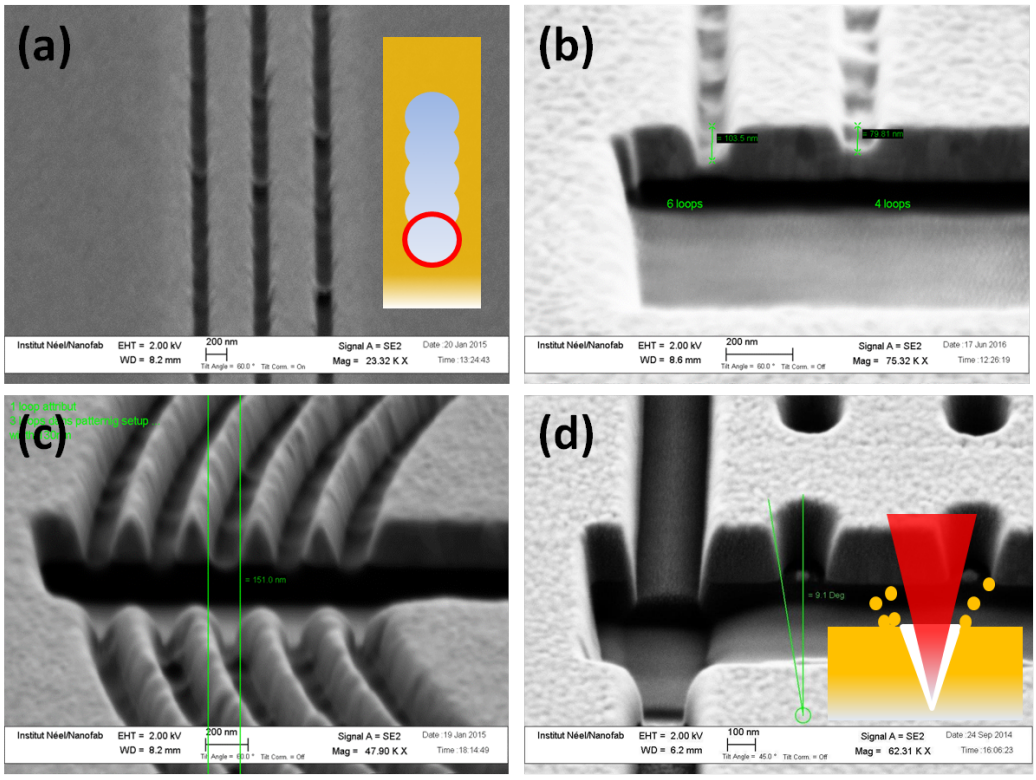

Fig. 2.7 SEM images of samples engraved by FIB. (a) Three slits were milled on the 50nm gold film. Inset briefly shows the procedure of line-milling from top to down with 5 consecutive spots indicated as the red circle. (b) Two grooves with different depths thanks to the different loop numbers were engraved on the 200nm gold film. (c) and (d) Corrugated structures and nano holes were realized by FIB on the 200nm gold film. The measurement of length and deformation angle were done in (c) and (d). The deformation angle is defined as the various angle from the top to the bottom of holes indicated by two green lines in (d).

We observe in Figure 2.7 (a), that the slits are not straight on each side because the beam shape is circular. If the slits need to be straighter on the side part, the step length may be reduced so as to increase the overlap or we may decrease the beam size determined by the beam current. If the groove depth needs to be precisely milled, the dwell time and loop

number have to be well adjusted. Thus, appropriate values for beam current, dwell time, step length and loop number on the different thicknesses of metal films play indispensable roles for the quality of structures. Besides, the direct measurement of lengths on SEM images is not exact anymore because the SEM column is tilted with respect to the normal position of the sample holder. The best way is to mill a test structure and then to engrave a cross section like in Figure 2.7 (b-d). The lengths measured on the cross section are more precise than the measurement on the surface. Meanwhile, it is a very efficient way to measure the depth and to inspect the variation of size with depths. The depth measurement makes sense especially when groove structures or stepped profiles are needed as shown in Figure 2.7 (b). Note that the diameters of holes or lengths between each structure gets smaller with increasing the depth in metals. The reason is that the beam size is restricted by the wall of holes and the accumulation of sputtered materials on the surface as indicated in the inset of Figure 2.7 (d). The maximum deformation angle of each structure is limited within 10° via strengthening beam current or increasing the number of loop. Certainly, the more precise structures we need, the longer time it costs. Thus, all the parameters such as dwell time, step length, loop number and beam current are set by compromising the milling time.

2.2.2 Electron beam lithography

Electron beam lithography (EBL) is the process of transferring a pattern onto the surface of a substrate based on the chemical modification of an electron sensitive organic resist film caused by electron beam irradiation. Opposite to the FIB, EBL is a major technique for deposition of metal structures in micro or nano scale instead of patterns on metal films. There are two indispensable advantages for EBL which are maskless and beyond the resolution limits of conventional photolithography. These advantages stem from the shorter wavelength of accelerated electrons compared to the wavelength of UV light used in photolithograpy, which allows to reach a much smaller diffraction limit (10nm instead of 1μm) [122]. Due to the negative charge of electrons, the electron beam can be easily controlled to directly write patterns by magnetic lens without the help of mask.

EBL was originally developed using SEM to which a pattern generator and beam blanker was added to control which areas of the viewing field are exposed [123–125]. The SEM column is quite similar to the FIB column shown in Figure 2.6 (b). In our study, a SEM Leo 1530 (FESEM) with a Elphy + Raith system with Orsay Physic FIB are used for both EBL and FIB. Elphy is a multifunctional software for pattern design, dose distribution and step size setting adapted for the Raith system which controls all the parameters for EBL or FIB such as beam scanning, stage position, imaging and so forth.

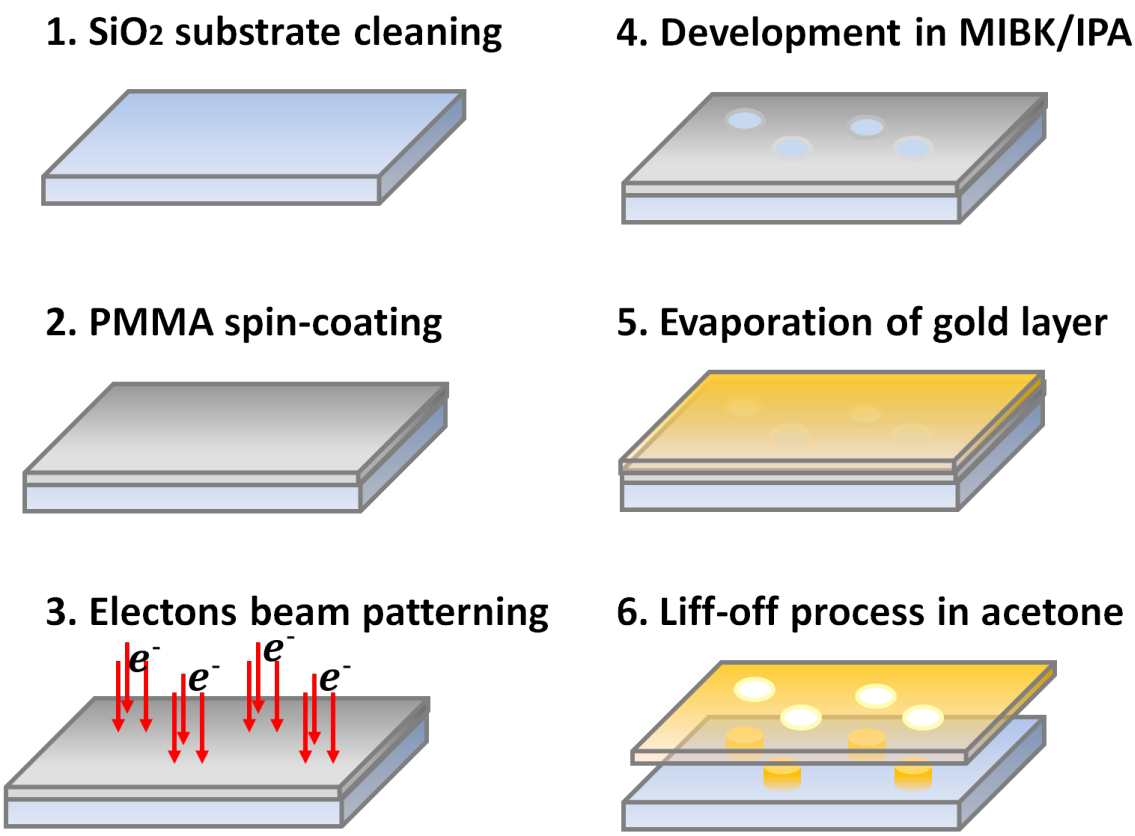

Fig. 2.8 Outline of electron beam lithography process for the positive resist.

The basic EBL procedure is schematically illustrated in Figure 2.8. The substrate is firstly cleaned separately by acetone and isopropanol in an ultrasonic bath for 1 min and 30 s. After drying with nitrogen, the substrate is further cleaned with reactive ion etching in Oxygen plasma so as to eliminate the residual organic molecules. Subsequently, the resist is deposited by spin-coating. Concerning the resists, there are mainly two classes which are positive and negative. Positive resists such as poly-methyl methacrylate (PMMA) consist of long polymer chains which are broken into smaller fragments under the exposure of high energy electron beams. Then the exposed parts dissolve in the e-beam developer solution due to a conversion from low to high solubility. On the contrary, the electrons in a negative resist convert the material to low solubility which undergoes a cross-linking reaction to combine smaller polymers into larger ones [126]. The thickness of resist depends on the speed of spin-coating and the concentration of resist solutions. For our case, positive 3% PMMA is chosen and the thickness is measured around 160 nm after 1 min spin-coating with 4000 RPM speed and 2000 RPM/s acceleration. Lastly, the PMMA is baked on a hot plate at 180° for 5 min so that the solution in PMMA can be completely evaporated.

The 10 nm layer of Al is evaporated on the PMMA resist so as to better conduct electrons during the electron illumination. The electron beam exposure on the desired patterns is then implemented inside the SEM and the quality of exposure resolutions depends on the electron beam current and the dose. Afterwards, the development is carried out. Firstly, Al layer is removed in MF (Megaposit MF-26A developer) solution for 30 s and the substrate is rinsed in the water flow for 1 min. The exposed parts are then removed in MIBK (Methyl isobutyl ketone)/IPA (isopropanol) (1:3) solution for 35 s. Subsequently, a rapid rinse in first isopropanol bath for 1 s and a normal rinse in the second isopropanol bath for 1min are used to get ride of the residual developer. After drying with nitrogen flow, the developed sample is then fed to the evaporation chamber and thin layer of Ti/Au (3/50 nm) layer is deposited. Lastly, the metallized sample is put in acetone for at least 12 hours or in NMP (N-Methyl-2-pyrrolidone) solution with a constant heating at 80°C for 1 hour so that the PMMA resist can be well removed during the lift-off process. If some part of PMMA still remains, we can gently rinse the sample in the acetone with pillar pipe or in the ultra sonic bath. After removing all the PMMA resist, the sample is rinsed in ethanol and dried up with nitrogen.

2.2.3 Sample gallery

In this part, I present all the samples fabricated by FIB and EBL during my PhD work. Some important structures and results will be discussed in detail in following chapters. Here, we focus on some preliminary results.

Structuration on the gold film by FIB

Concerning nanostructures on gold film milled by FIB, single slits are firstly developed aiming at studying structure parameters for exciting SPPs. The length of slits is fixed at 5 μm and the width varies from 100 nm, 150 nm, 200 nm, 250 nm, 300 nm and 350 nm as shown in Figure 2.9 (a). Once the laser spot is focused on the center of each slit, SPPs can be excited propagating along two sides perpendicular with the slit. The coupling efficiency of SPPs can be quantified with SPP intensities on back focal plane (Fourier plane) by leakage radiation microscopy (LRM). The details about experimental setups and back focal plane analysis will be introduced in the next chapter. After cross section analysis of SPP intensities in Figure 2.9 (b), 200 nm wide slit obtains the maximum SPP coupling efficiency for wavelength 633 nm.

Secondly, the SPP Bragg reflectors formed with several periodic slits in Figure 2.9 (c) are investigated. One slit with 5 μm long and 200 nm wide is milled in the center for exciting SPPs propagating along two sides. At each side around 5 μm away from the central slit, an

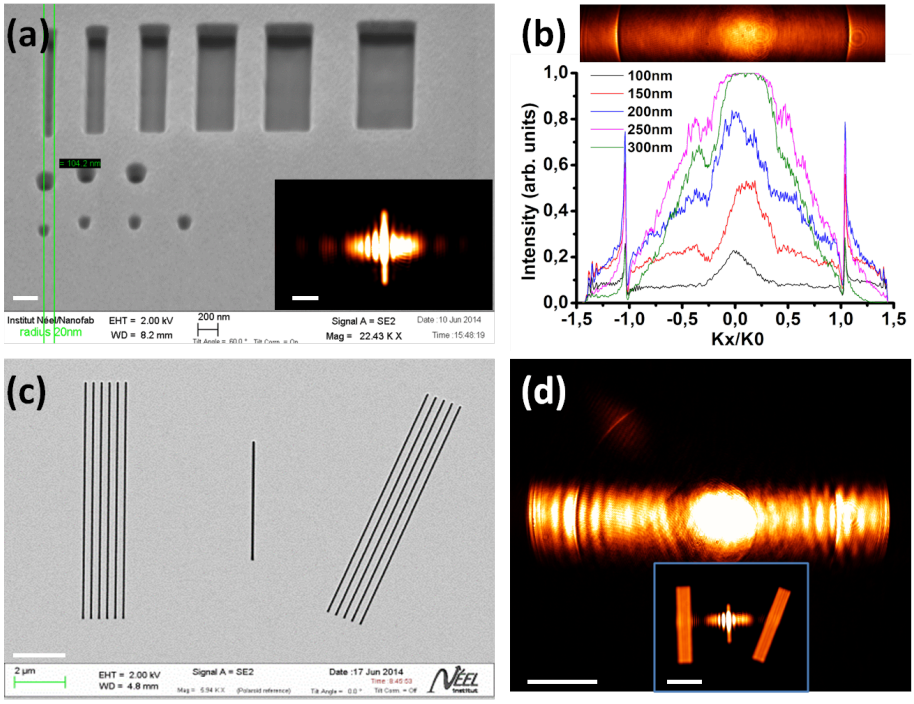

Fig. 2.9 (a) The slits milled by FIB are used to determine the best width for exciting SPPs. The inset is a leakage radiation microscope (LRM) image on direct plane. The scale bar is 200 nm for the SEM image and 2 μm for the inset. (b) The image on Fourier plane is shown on the top. Two bright rings correspond to leaked SPPs. Its cross section on the bottom is used to find the maximum SPP peak intensity. (c) SPP Bragg mirror system includes a slit in the center for exciting SPPs and two Bragg slit arrays for reflecting SPPs. The scale bar is 2 μm. (d) Back focal plane image associated with the direct plane image in the inset: excitation of the central slit of the structure depicted in (c). The image on Fourier plane shows that reflected SPPs on the top left achieved by the right tilted reflector. The intensity of this signal is used to optimize the period of slit-array reflectors. The scale bars are 0.5 k_0NA and 5 μm in the inset.

array of slits is designed including 5 slits with 200 nm wide and 10 μm long respectively. Three different periods 300 nm, 350 nm and 400 nm are studied. The array on left side is designed parallel to the central slit and the array on the right side is tilted 45° with respect to the central slit in order to reflect SPPs to a new direction so as to avoid incoming signals. Since SPPs are excited in the middle slit, propagating SPPs on the left side can be reflected back to the right side and they are further reflected to the 45° direction. The reflected SPP intensities can be visualized on Fourier plane in Figure 2.9 (d) and the period is finally optimized at 300 nm which exactly corresponds to the half SPP wavelength.

Thirdly, nano holes are introduced to form hole arrays aiming at exciting SPPs radially. The square arrays are designed with 4, 9 or 16 holes and their periods are fixed at 600 nm

corresponding to the SPP wavelength. Besides, three various diameters 100 nm, 150 nm and 200 nm are studied as well. By the analysis of SPP intensities on Fourier plane in Figure 2.10 (b), we observe that the number of holes don't change the SPP coupling efficiency and the 150 nm diameter shows slightly higher SPP intensity than the other two. Thus, 4-holes with 150nm diameter will be used for the following study.

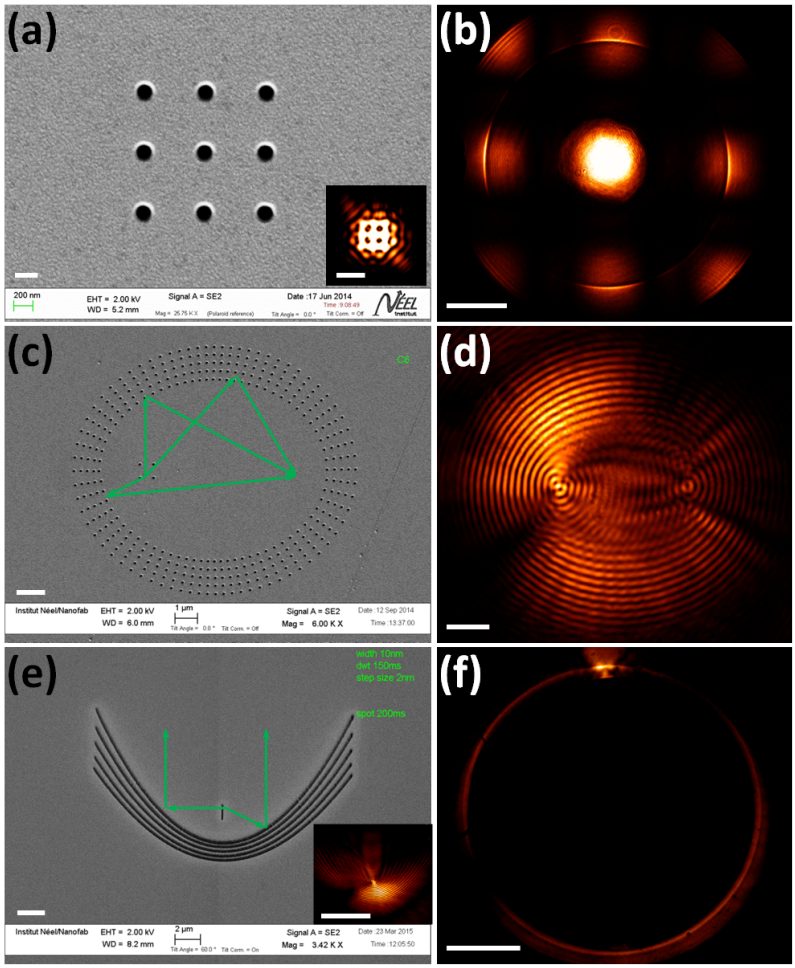

Fig. 2.10 (a) The 3 by 3 hole array is milled on 50 nm gold film. The inset is image taken by LRM on direct plane. The scale bars of the SEM image and the inset are 200 nm and 1 μm respectively. (b) The image on Fourier plane shows nano hole array generates SPPs propagating along four major-axis directions. The scale bar is $0.5k_0$N.A. (c) The elliptic reflector is made of holes. On one focus of the ellipse, a 4-holes array is designed on one focus of ellipse so as to excite SPPs. (d) The LRM image of the elliptic reflector on direct plane. The scale bars of (c) and (d) are 1 μm and 2 μm. (e) The parabolic reflector has a slit on the focus for exciting SPPs. The inset is the corresponding LRM image on direct plane. The scale bars are 2 μm and 5 μm in the inset. (f) The corresponding image on Fourier plane. The scale bar is 0.5 k_0NA.

Considering no obvious difference of hole size for SPP excitation, we tried to study whether diameters influence the SPP reflection. The elliptic Bragg reflector with holes in Figure 2.10 (c) is milled on 50 nm gold film and two degrees of freedom are involved which are the hole diameter and the period between two holes. Thus, 3 various values 100 nm, 150 nm and 200 nm involve for hole diameters and 250 nm, 300 nm and 350 nm for period between each hole. According to the geometric properties of ellipse, the elliptic reflector is supposed to reflect all the SPPs from the excited focus to another focus. A direct plane LRM image is presented in Figure 2.10 (d) while SPPs are now excited by an aperture optical tip which is placed in the near field of the film. Once the left focus is excited by the tip, a strong light spot on the right focus appears. It means that the elliptical reflector is suitable to directionally control SPPs from one focus to another focus. The optimal parameters are finally concluded as 200 nm for the hole diameter and 350nm for the period between each hole corresponding to the best parameters for hole-like reflectors.

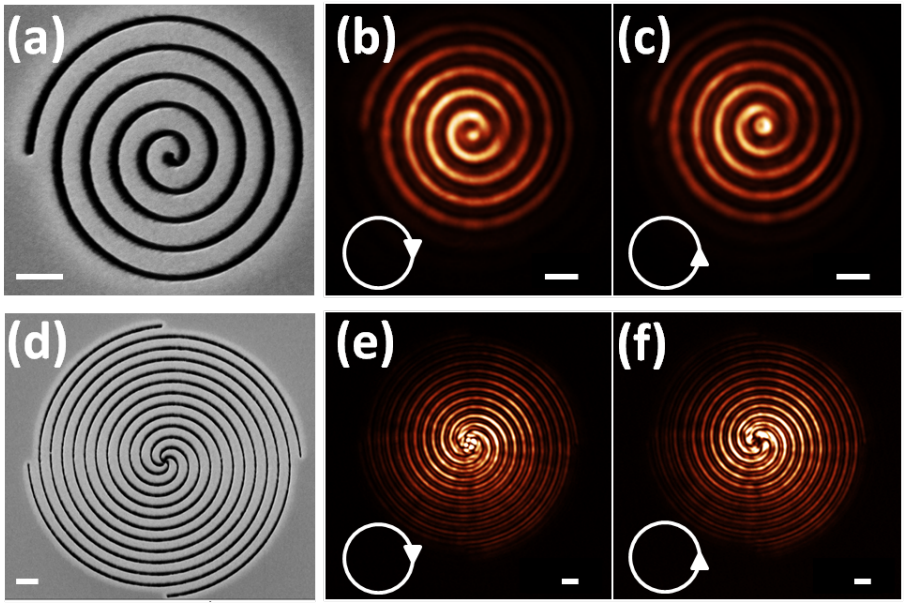

Fig. 2.11 (a) The Archimedes' spiral is milled by FIB on 50 nm gold film. (b), (c) The images on direct plane are taken by LRM. The laser spot with two circular polarization states is slightly defocalized in order to illuminate the whole structure. (d) The SEM image of 4-arms Archimedes' spirals. (e), (f) The 4-branches structure is illuminated by two circular polarization states. The white circles in (b), (e) indicate the right-handed circular polarization (RCP) and the white circles in (c), (f) indicate left-handed circular polarization (LCP). The scale bars are all 1 μm.

The parabolic reflector in Figure 2.10 (e) works in a similar way, in which the excited SPPs at the focus with a similar near field optical tip can be reflected by the milled parabolic

structure on 50 nm gold film and can collimately propagate to the other side. I present here both the direct and Fourier plane images which show a strong signal towards the upside. The Fourier plane image shows more evident SPP signals on the top and nearly nothing on the bottom as shown in Figure 2.10 (e). It is proven that the SPPs are efficiently reflected and collimated. More details can be found from the thesis of Martin Berthel [127].

Fourthly, the Archimedes' spiral attracts a lot of interest because it can generate vortex beams which consist of spiral wavefronts along the propagation direction via spin-orbit coupling. A simple Archimedes' spiral and a 4-arms spiral are fabricated as illustrated in Figure 2.11 (a) and (d) respectively. We observe that the chiral structure shows a different response for the right-handed circular polarization (RCP) and the left-handed circular polarization (LCP). A dark hole in the center called optical vortex is formed and shown in Figure 2.11 (b), (f). On the contrary, a bright spot is observed in Figure 2.11 (c), (e) with illuminating by the opposite circular polarization state. It further proves the selection rule for the spin-obit couping [128, 82] which is to say that the number of arms in the spiral decides the size of optical vortex. More details are investigated by Aline Pham during her PhD study.

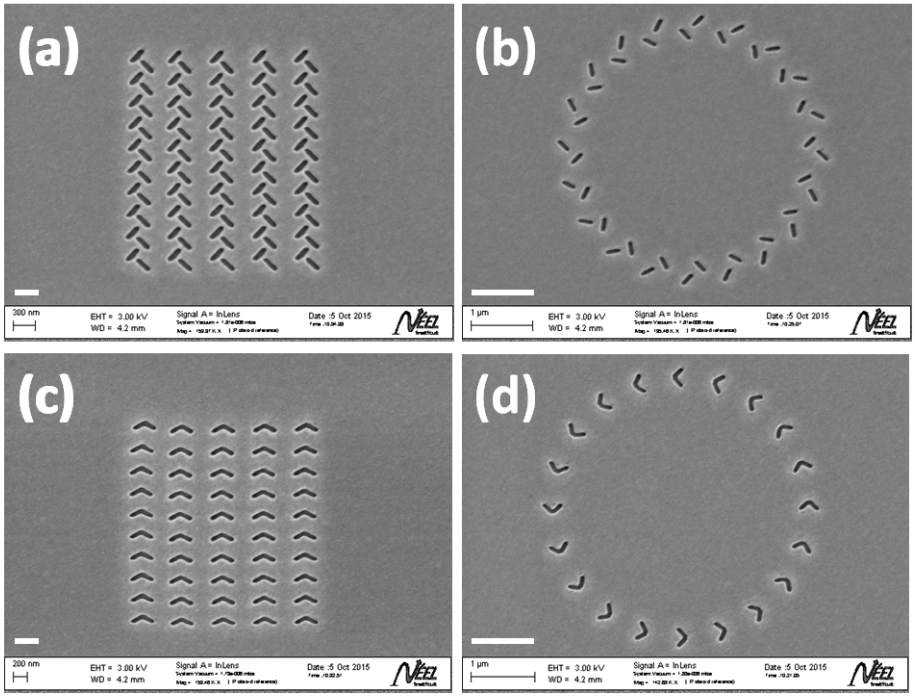

Fig. 2.12 (a), (b) SEM images of the array of T-shaped apertures and the circle of T-shaped apertures. (c), (d) SEM images of the array of Λ-shaped apertures and the circle of Λ-shaped apertures. The scale bars of (a) and (c) are both 300 nm. The scale bars of (b) and (d) are 1 μm.

Lastly, arrays of T-shaped and Λ-shaped apertures are milled aiming at studying the spin-controlled directional SPP generation. Then circles of T-shaped and Λ-shaped apertures shown in Figure 2.12 are designed to further study the SPP vortex generation. The results will be thoroughly reported in Chapter 4.

Structuration deposited on the waveguide by EBL

Let's now focus on the gold structures deposited on the waveguide. 50 nm thick gold structures are deposited on the TiO_2 waveguide via EBL to investigate the directional coupling of light into the waveguide. All the generations of gold structures are shown in Figure 2.13. At the beginning, we tried to develop the Yagi-Uda coupler system. A Yagi-uda antenna consists of 5 gold rods and each rod has the same width (50 nm) but various lengths. The longest rod served as reflector has 200 nm long and the 3 shortest served as directors have 145 nm long. The middle one served as feed has 160 nm long. The period between each rod was fixed at 200 nm. Considering that only one antenna can not provide enough signal for the far field test, an array of 9 Yagi-Uda antennas are designed with 1.2 μm period between each antenna. The array of antennas is surrounded by two simple decouplers apart from 4.5 μm from the center in order to couple out the guided light in the waveguide. Each decoupler contains 4 rods with 4 μm length, 190 nm width and 380 nm period, which will be specifically discussed in Chapter 5. The LRM image of this system and its cross-section profile in Figure 2.13 (b) don't show us the directionality as we expect because the same quantities of light get out from two decouplers.

Subsequently we developped a similar asymmetric antenna with more rods shown in Figure 2.13 (c). This time, 10 rods with different length are tried out. The width and the period are fixed at 50 nm and 200 nm as the same as Yagi-Uda antennas. The lengths of rods decrease from 4 μm to 3.65 μm with a coefficient 0.99 for each of the two adjacent rods. Unfortunately the couplers do not work and no light is coupled into the waveguide. The reasons why they do not work can be attributed to two problems which are size and phase effects. Firstly, if the total gold size is too big compared with the incident laser beam, the most part of light would be reflected and be scattered randomly. This leads almost to no light coupling into the waveguide in the second generation of coupler system. Secondly, the difference of phases between each adjacent rods is a critical factor for directional coupling but it is very sensitive to the rod dimension. In the first generation, the small inaccuracy for the rod size during the EBL process led to huge change of phases which might fail the directional coupling.

However, a lot of useful experiences for directional coupling light in the waveguide has been accumulated and is applied to our latest generation coupler system. The Λ-shaped

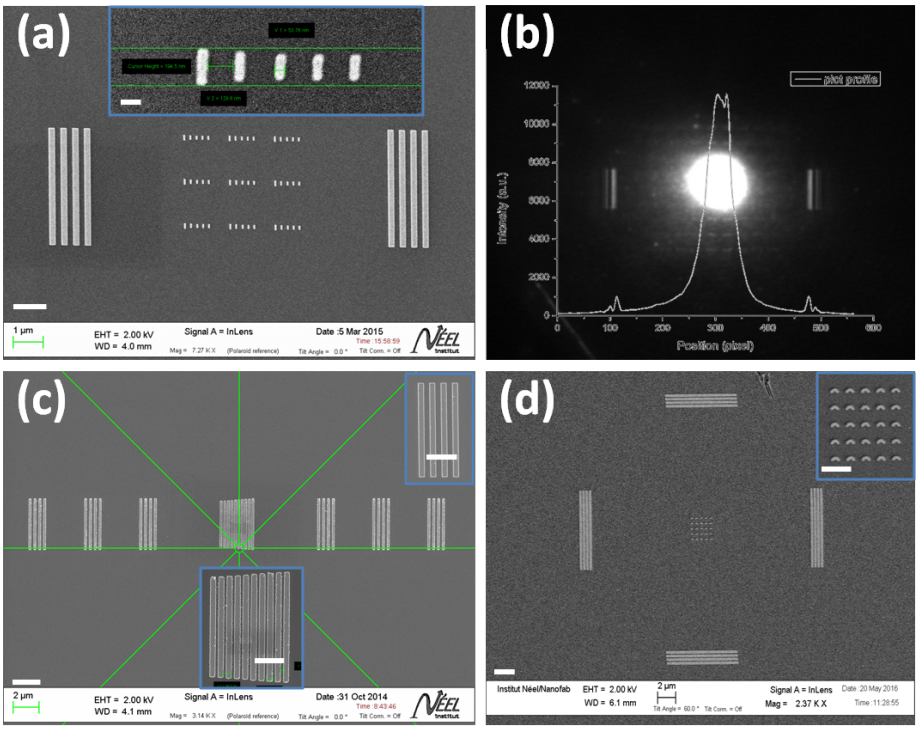

Fig. 2.13 Gold structures fabricated by EBL on the waveguide. (a) Yagi-Uda coupler system. The array of 9 Yagi-uda antennas in the center around by two decouplers. The scale bars are 1 μm and 100 nm in the inset. (b) The LRM direct plane image of the Yagi-uda coupler system with the cross-section profile. (c) The second generation of coupler system is made of one asymmetric rod array and 6 decouplers around it. The scale bars are 2 μm and 1 μm in the insets. (d) The latest generation of coupler system consists of an array of Λ-shaped rods and 4 decouplers around it. The scale bars are 2 μm and 1 μm in the inset respectively.

antennas are introduced as the coupler system in Figure 2.13 (d) and they showed a good spin-based directional coupling of light into the waveguide which will be discussed in detail in Chapter 5.

In brief, the sol-gel process and thin film deposition for the TiO_2 waveguides have been optimized by characterizing the properties of waveguides. The 240 nm thick waveguide is decided to be used in our future study and its refractive index of the TM mode is characterized at 1.75. Then, the two methods for nanostructuration are introduced. The process parameters in the FIB and EBL play an important role for the precision of the metal structures in the nano scale. Finally, the sample gallery shows all the structures which we developed and some preliminary results are discussed here. In the next chapter, the methods for observing and characterizing the structures of interest will be presented and the experimental setups of the imaging systems and polarization generation will be schematically described.

Chapter 3

Imaging systems

Abstract: In the first section, the leakage radiation microscopy is thoroughly described as the main imaging system for the detection of Surface Plasmon Polaritons (SPPs). The propagation directions of the SPP leaky modes can be distinguished on the Fourier plane, which is used for observing the directional coupling of SPPs. In the second section, the dark field and fluorescence imaging systems are introduced for visualizing the spin-orbit coupling of light into the waveguide. Nanocrystals deposited on the sample surface serve as an efficient method for displaying the propagation of the confined light in the waveguide. Lastly, the experimental methods for polarization generation and detection are explained.

Contents

3.1 Leakage radiation microscopy

After the presentation of several approaches for launching surface plasmon polaritons (SPPs) in Chapter 1, we will introduce here the ways to image the confined fields in nanostructure so as to analyze their properties. Three principal methods allow us to realize the detection of SPPs. Firstly, the near field detection with the help of a very sharp tip in the vicinity of the surface is extensively employed for imaging SPPs such as scanning near field optical microscopy (SNOM) [129–131], atomic force microscopy (AFM) [132] and scanning tunneling microscopy (STM) [133]. The evanescent fields of SPPs penetrating into the air can be coupled to propagating modes in a tapered tip. Secondly, emitters such as fluorescent molecules or quantum dots directly placed on the surface can map SPPs instead of locally collecting the optical near field of SPPs using a tip. If the frequency of the propagating SPPs lies within the absorption spectra of emitters, the evanescent tail of the SPP field can excite the fluorescence radiation which is proportional to the intensity of the local field at the position of the emitters [64]. Note that this method can also detect the other confined waves such as guided waves and so forth. Thirdly, an optical far-field method named leakage radiation microscopy (LRM) shows the versatility for allowing direct imaging and quantitative analysis of SPP propagation on thin metal films [134, 135]. This possibility is based on the detection of coherent leaking of SPPs through the substrate. Since LRM serves as the principal experimental method for our investigation about the SPP directional generation, the principle will be explained in detail in the following sections.

3.1.1 Leaky modes of SPPs and their detection

Like exciting SPPs by the prism coupling with Kretschmann configuration, the reversed process allows us to detect SPPs via the SPP leaky waves. Now, let's take the classic air/metal/glass system into consideration. SPPs excited at the interface between the air and a metal film (assuming a perfectly flat interface) do not suffer radiation loss into the air region because the dispersion curve of SPPs lies outside the light cone defined as $k_0 = \omega/c$. However, SPPs can radiate as leaky electromagnetic waves into the higher index medium, that is, the glass substrate with the index of refraction n. This radiation loss occurs at all points of the dispersion curve that lie to the left side of the light cone of the substrate defined as $k = n\omega/c$ [1] as indicated in Figure 1.13 in Chapter 1. Therefore, the propagation constant β for the leakage radiation into the substrate is defined as

$$k_0 < \beta < k_0 n. \tag{3.1}$$

Note that the leaky energy can pass a metal film thinner than about 100 nm (it also depends on the grain size and the roughness of metals). If the metal film is so thick that the absorptive losses in the metal are larger than the radiative losses, no leaky energy can be detected in the substrate. In the case of thin metal film, the wave vector matching imposes that leaky SPPs can exit the metal film only at a given angle θ_{LR} such that

$$k_0 n \sin(\theta_{LR}) = k_{spp} \simeq \Re(k_0 \sqrt{\frac{\varepsilon_{metal}}{1+\varepsilon_{metal}}}), \tag{3.2}$$

where $\Re$ stands for the real part of SPP wave vector since the role of the imaginary part can be approximately neglected, $n \simeq 1.5$ is the glass optical index and ε_{metal} is the metal dielectric permittivity. For the case of gold film, the leaky angle θ_{LR} is determined as 44° which is larger than the critical angle for an air-glass interface θ_c=42°. It means that the leaky waves can not exit from the substrate and they can not be detected by classic objectives in the air. Thus, an oil immersion objective is introduced to solve this problem. The substrate is placed in contact with the objective through the immersion oil as shown in Figure 3.1 (a). The refractive index of the oil is chosen as the same refractive index of the glass substrate ($n_{oil} \simeq 1.5$) so that the leaky waves pass directly into the objective. The real part of magnetic field H_y associated with a SPP mode leaking through a thin gold film is illustrated in Figure 3.1 (b) which is deduced based on the ref [134]. This figure shows intuitively the field distribution during the SPP leaky process.

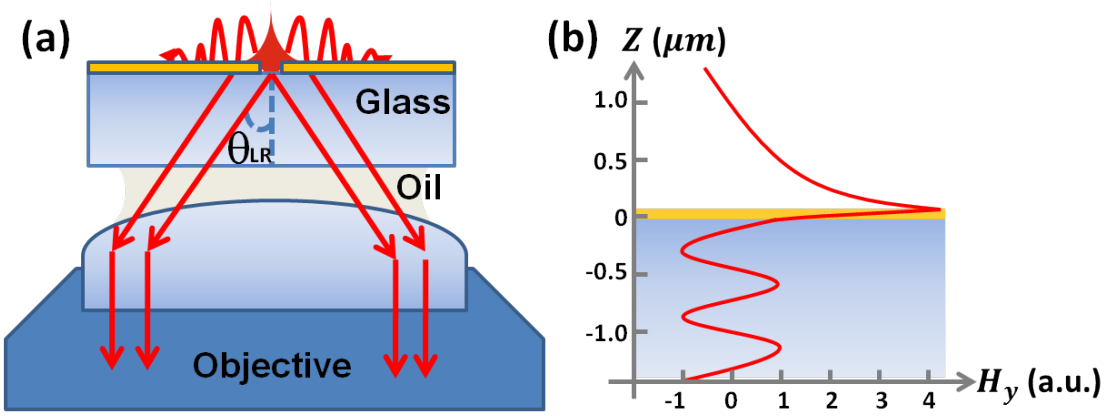

Fig. 3.1 Leakage radiation microscopy principle. (a) The launched SPPs leak with a specific angle $\theta_{LR} = 44°$ through the thin gold film into the glass substrate. They are then collected by an oil-immersion objective. (b) Schematic plot of the real part of magnetic field H_y with respect to the distance Z normal to the sample surface. The thicknesses of the gold film and substrate are 50 nm and 0.2 mm respectively.

Besides, we would like to mention that the oil immersion objective can reach a high numerical aperture which is defined as

$$NA = n \sin \theta, \tag{3.3}$$

where n is the refractive index of the working medium and θ is half the maximal angle of the cone of light injected in the lens. As we introduced in Chapter 1, the numerical aperture of leaky SPPs is equal to $n \sin(\theta_{LR}) = n_{spp} = 1.05$. However, the numerical aperture of the classic objective lens is always less than or equal to unity because the $n = 1$ for the air and $\sin \theta$ is not higher than 1. Thus, the high numerical aperture of the oil immersion objective serves as an alternative method allowing us to collect more light with large angles such as SPP leaky angle. The high numerical aperture also provides higher resolution for a microscope because the minimum separation between two objects (δ) under a microscope is defined as

$$\delta = \frac{\lambda}{2NA_{obj}}, \tag{3.4}$$

where λ is the wavelength of incident light. If the distance between two objects are shorter than the minimum separation, these two objects will be considered as a single object. Therefore, the higher NA_{obj} lead to shorten this distance so as to increase the resolution.

3.1.2 Fourier plane imaging

As we know that SPPs can radiate into the objective via leaky modes, these signals with a specific leaky angle can be collected and then displayed on the back focal plane (Fourier plane). Unlike the front focal plane, all the light parallel with each other can be collected on the back focal plane of the lens at one point. Specifically, all the electromagnetic fields propagating along the optical axis (Z-axis) contain two spatial frequencies k_x and k_y which are also associated with polarization states. The back focal plane of an objective allows to image a k-space with the angular distribution of the field via a Fourier transformation from the spatial coordinates (x-y) to the spatial frequencies (k_x-k_y), which is the reason why the back focal plane is also called Fourier plane. The principle of Fourier plane imaging is illustrated in Figure 3.2 (a). All the beams with the same angles θ are focused on Fourier plane (FP) as the same point and the beams from the same source point are focused on the direct plane (DP). Noteworthy, the angular distribution of all the beams forms three circular regions due to the limitation of the angle θ as shown in Figure 3.2 (b). First of all, the propagating wave suffers the total internal reflection when it goes out from the oil immersion objective with

$\theta > \theta_c$. The critical angle θ_c at the air-glass interface has already been determined at 42°. Thus the permitted propagating light cone on FP is located within the green region with a radius of $NA_1 = 1$. Secondly, the θ_{max}, which is deduced from the numerical aperture of oil immersion objective, decides the size of FP. The angles inferior to θ_{max} can be imaged in the grey region with a radius of $NA_{obj} = 1.45$ (the oil immersion objective what we use). Thirdly, the leaky mode of SPPs with angle $\theta_{LR} = 44°$ can be visualized as the red ring with a radius of $NA_{spp} = 1.05$.

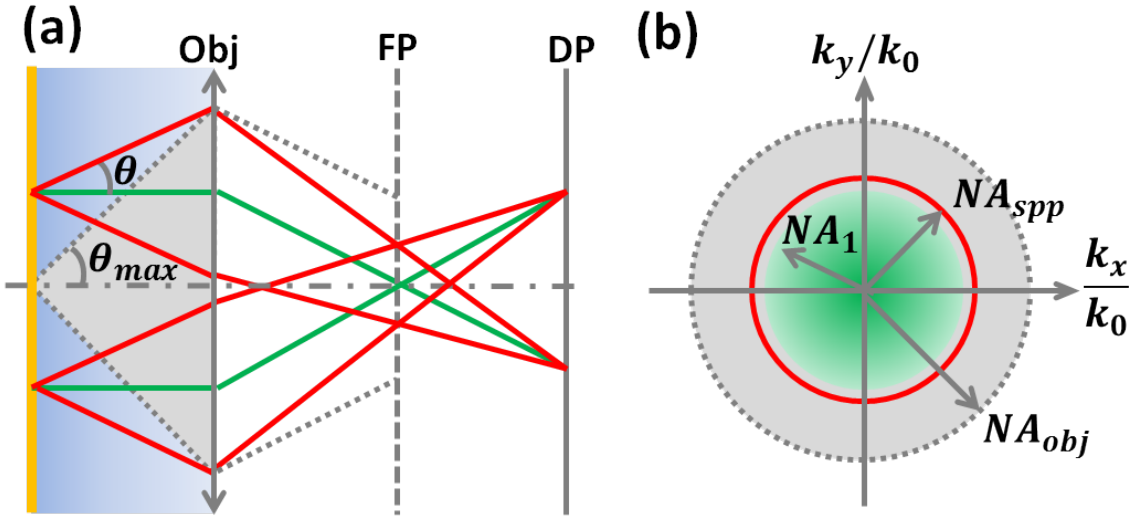

Fig. 3.2 Principle of Fourier plane imaging. (a) Side view of Fourier plane imaging principle. Assuming that two point sources are located at two random positions on the metal film (yellow line), the light beams with certain angles (θ) with respect to the optical axis (horizontal dashed dotted line) can pass the glass substrate and go through the oil immersion objective (Obj). The Fourier plane (FP) and the direct plane (DP) are indicated as a vertical dashed line and a vertical solid line respectively. The θ_{max} represents the numerical aperture of the objective. (b) Top view of the Fourier plane. The green region represent the light cone permitted to pass the substrate ($\theta < \theta_c$) with radius NA_1. The red ring indicates the leaky mode ($\theta = \theta_{LR}$) with radius NA_{spp} and the dotted line is the limitation of the objective ($\theta = \theta_{max}$) with radius NA_{obj}.

Experimentally, this ring-like distribution corresponding to leaky SPPs is not always a complete ring because it depends on the direction of SPP propagation. For example, a slit on 50 nm gold film is excited by a focused laser beam as shown in the inset of Figure 3.3 (a). SPPs launched by the slit propagates along its preferred axis which is normal to the slit. A small angular divergence of the SPP signal on FP results from the portion of the slit which casts the incident field. The remaining signal on the Fourier plane is a convolution between a disc, which stands for the Fourier transform of the Airy spot of the excitation, and a cardinal

sinc function, which is based on the Fourier transform of the rectangular slit [136]. Normally, if we consider only SPP field, its radial distribution with real wave vectors (k_x) on FP would follow a Lorentzian profile defined as [134, 137]:

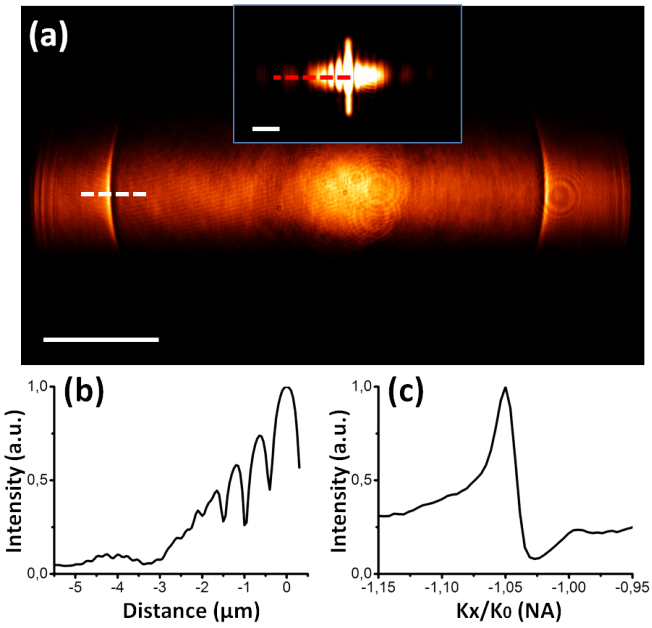

Fig. 3.3 Comparison of the Fourier plane image and the direct plane image. (a) The Fourier plane and the direct plane (inset) images are taken by LRM when a slit on 50 nm gold film is excited by a focused red laser in the center. The scale bars are $0.5k_0$ NA and 2 μm in the inset. (b), (c) The cross sections on DP and FP indicated by the red and white dashed lines respectively.

$$I_{PF}(k_x) = const.|\frac{1}{k_x - k_{spp}}|^2 = \frac{const.}{(k_x - k'_{spp})^2 + (k''_{spp})^2}, \tag{3.5}$$

where k'_{spp} and k''_{spp} are real and imaginary parts of SPP wave number. The Lorentzian function is centered on k'_{spp} with a full width at half maximum (FWHM) of $2k''_{spp}$. However, the experimental image on FP shows an asymmetric profile in Figure 3.3 (c). It is necessary to take the contribution of the directly transmitted light through the slit into consideration because the direct light will interfere with the SPP signal in the far field. This modification can be explained by Fano-type interference [134]. Thus, the total field distribution is expressed as:

$$I_{PF}(k_x) = const.|\alpha + \frac{1}{k_x - k_{spp}}|^2 \simeq \frac{(2\alpha(k - k'_{spp}) + 1)const.}{(k_x - k'_{spp})^2 + (k''_{spp})^2}, \tag{3.6}$$

where α is defined as a coefficient corresponding to the background intensity of the direct transmitted light through the slit and two approximations have been accounted to derive the final equation. We assume that α is a real number and close to 0 because the influence of the transmitted light is much smaller than the SPP signal in the large-angle region on FP. Based on this equation, we could theoretically reproduce the experimental Fano-type profile and calculate two values corresponding to the peaks each side are around ± 1.055 which are still around ± 1.05 corresponding to SPPs. Thus, the profile on FP is still valid to quantify SPPs through measuring the peak values. On the contrary, the profile on DP in Figure 3.3 (b) cannot well distinguish the transmission of light and SPP signal without the help of the angular selection because the profile intensity is impacted by diffraction of the slit, the directly transmitted light and SPPs.

3.1.3 Experimental setup

In order to reduce the interference of the incident light, an opaque mask has been added on the FP. The experimental setup of LRM for recording the SPP radiation has been developed from the beginning of my PhD at Institute Néel in Grenoble as illustrated in Figure 3.4.

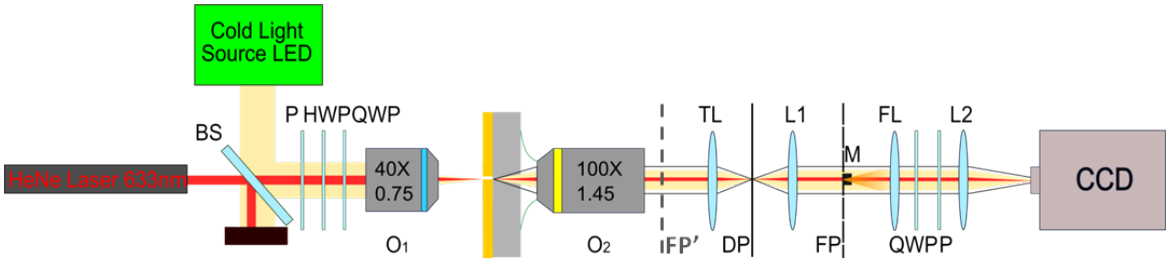

Fig. 3.4 Experimental setup of leakage radiation microscopy (LRM) at Institut Néel in Grenoble. A normally incident laser beam is weakly focused onto the sample via a microscope objective O1. The leaky SPPs are collected by a CCD camera using an oil immersion objective O2. The DP and FP imaging can switched via flipping a Fourier lens (FL).

A collimated He-Ne laser beam (633 nm) is weakly focused via a microscope objective (O1, 40×, 0.75 NA) and normally illuminates the sample from the gold side. A cold light source LED is used to image and visualize the nanostructures on the sample. A beam splitter (BS) is employed for supporting two sources at the same time. A set of polarizer (P), achromatic half-wave plate (HWP) and achromatic quarter-wave plate (QWP) is used to prepare the incident beam into the desired polarization state. Light which is scattered and transmitted through the glass substrate is collected with an oil immersion objective (O2, 100×, 1.45 NA). The real plane images are focused onto the direct plane (DP) by means of a tube lens (TL, f=75 mm). A lens with the same focal length (L1, f=75mm) reconstructs

the image on the first Fourier plane (FP′) and projects that image on the second Fourier plane (FP) where a beam blocker (M) can be used for spatially filtering the light directly transmitted through the sample [137]. The opaque beam blocker in chromium is mounted on a flip supporter and the position can be adjusted along three directions (x, y, z). The real space image can also be mapped into the Fourier space via a flip Fourier lens (FL, f=75mm). Without this FL, the direct plane image can be observed. A set of quarter-wave plate (QWP) and polarizer (P) is used to perform polarization analysis of the transmitted signals before they are focused via second lens (L2, f=150mm) onto a CCD camera. The input and output polarization states prepared via a set of polarizer (P), half-wave plate (HWP) and quarter-wave plate (QWP) will be described thoroughly in the last section of this chapter.

3.2 Dark field and fluorescence imaging

In order to obtain more information about directional coupling the light into the waveguide, the dark field and fluorescence microscopes are employed based on the leakage radiation microscopy (LRM). Dark field imaging is an efficient method to exclude the unexpected light from the image especially the unscattered beam from the source. Attributed to introducing two masks in the imaging system, some rays are eliminated and a dark background can be achieved. The contrast and the resolution of dark field images are thus improved. Fluorescence imaging, as we mentioned before, is not only a good way to visualize SPPs but also to efficiently detect other confined waves such as guided waves. Besides, properties of nanocrystals deposited on the waveguide such as the emission spectrum and the life time for the fluorescence can be further studied.

3.2.1 Experimental setup for dark field imaging

In order to view a small object in the dark field, an opaque mask is placed on the way of the incident beam so as to filter the direct beam with small angles. Only the light with the large angles impinge on the sample. If there is no object on the sample, the detection for the small angles (a diaphragm) placed in the center of the back side of the sample has almost no light arriving because the large angles reflect with the same angles or transmit the sample and propagates still with the large angles. If there is a small object, the incident light with large angles is scattered and the scattered small angles reach the detection system. Thus, small objects on the sample appear as bright, diffraction-limited spots with a strong-contrast background [138].

Our experimental setup is based on the principle of dark field imaging and the configuration is slightly different. A schematic of the experimental setup for realizing the dark field detection is indicated in Figure 3.5. The dark field filters are built up with a reflection of the LRM system which was developed at Institut Lumière Matière (ILM) in Lyon. As the matter of effect, the aim of dark field imaging in our case is to visualize the directional coupling into the waveguide without presence of incident light instead of observing nano-antennas diffraction. Thus, two masks are reversely placed in the imaging system. The laser beam is firstly confined with a diaphragm (F_1) and injected in the objective (100×, 1.49 NA). The focal laser beam then impinges on the nano-antennas. The diffraction with all kinds of angles takes place and is reflected back to the objective. The reflected light pass through a beam spliter (BS) and is refocused to the direct plane (DP) by a tube lens (TL). A lens L1 and a flip Fourier lens (FL) can reconstruct the image on the Fourier plane (FP). The second mask with a ring-like aperture denoted as F2 is placed on FP. This mask can block the light beam with small angles including the incident laser beam and let pass the light with the expected large angles via adjusting the width of the aperture. Finally, the light is reflected by a mirror (M) and focused into a CCD camera by a lens L2. The advantage of the dark field imaging is to select angles on which we are interested by easily adjusting the size of apertures of two masks.

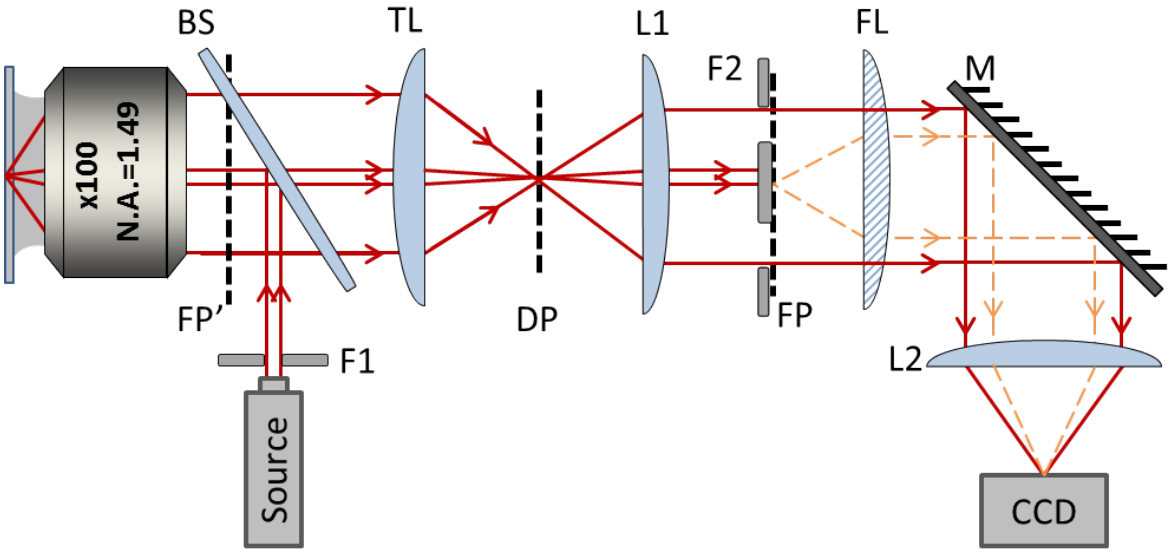

Fig. 3.5 Experimental setup for dark field imaging at ILM in Lyon.

3.2.2 Nanocrystals deposition and verification

The semiconductor nanocystals are widely developed and used in the past 30 years because of their remarkable optical properties. They have a large band of absorption but very fine peak of emission in the room temperature. Moreover, the peak of emission is tunable in the whole visible spectrum by changing the size of nanoparticles. The position of the optical transition radiation results from 3 factors: the band gap of the bulk semiconductor, the Coulomb potential of interaction between electrons and holes, and the quantum confinement. In this study, the core-shell cadmium selenide/zinc sulfide (CdSe/ZnS) nanocrystals are used as emitters in the emitter-plasmons-waveguide system and then they can be detected by the fluorescence microscopy.

Band diagram of CdSe

First of all, we explain a basic knowledge for the CdSe nanocrystals. In fact, the bulk CdSe is a II-VI semiconductor which has a relatively complicated band structure. The conduction band is well approximated by the simple parabolic band but the model is not suitable for the valence band. The latter arises from Se 4p atomic orbitals and includes a 6-fold degeneracy at k=0 including spin. In contrast, the conduction band arises from Cd 5s orbitals and is only 2-fold degenerate at k=0. The real bulk CdSe band diagram is schematically shown in Figure 3.6 (a). Due to strong spin-orbit coupling $\Delta_s o = 0.42$ eV in CdSe, the valence band firstly degenerates in two sub-bands with $J = 3/2$ and $J = 1/2$. Away from k=0, the sub-band with J=3/2 is further split into two sub-bands with $J_z = \pm 3/2$ and $J_z = \pm 1/2$. The three sub-bands are classified named heavy-hole, light-hole and split-off-hole sub-bands from top to down of the band structure. Due to the CdSe crystal field of the hexagonal lattice, a small degeneracy happens between heavy-hole and light-hole sub-bands at k=0 ($\Delta_c f = 0.025$ eV) [139].

After a quick review of bulk CdSe band diagram, we are going to study the confinement of charge carriers which leads to the reason why their optical spectra are highly structured and size-dependent. Light absorption in semiconductor generally binds electrons and holes to form electron-hole pairs, so-called excitons. When excitons recombine, their energies lead to a light emission named fluorescence. Once excitons are bounded with several specific energies which can be tuned by changing the size of quantum dots, the confinement of charge carriers take place. In bulk CdSe, Coulomb interaction V_c between electrons and positively charged holes dominates to bound excitons. The effective mass of excitons m^* can be expressed as:

$$\frac{1}{m^*} = \frac{1}{m_e^*} + \frac{1}{m_h^*}, \tag{3.7}$$

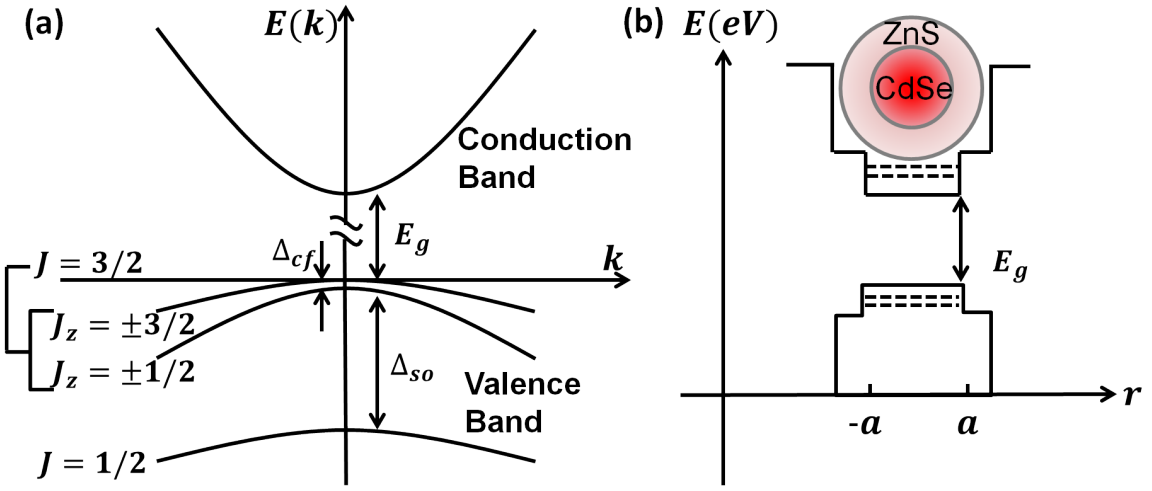

Fig. 3.6 Band diagram of CdSe. (a) Bulk CdSe band structure. The band gap energy E_g is determined at 1.8 eV for $\lambda_0 = 688$ nm. (b) Band structure of a CdSe nanocrystal. The dashed lines show the discrete energy levels while the quantum confinement occurs. The value $\pm a$ denote the radius of the core CdSe. The shell ZnS is used to avoid the non-radiation relaxation via creating a potential well.

where m_e^* and m_h^* denote the effective mass of electrons and holes in bulk CdSe respectively. Similarly with Bohr radius of hydrogen atom, the Bohr radius of excitons a_{exc} in bulk CdSe is deduced as:

$$a_{exc} = \varepsilon_r \frac{m_e}{m^*} a_0, \tag{3.8}$$

where ε_r, m_e and a_0 represent the dielectric constant of bulk CdSe, the electron mass and the Bohr radius of hydrogen atom respectively. The Bohr radius of excitons a_{exc} is determined at 5.6 nm [140]. Once the radius of CdSe crystals achieves the same order of magnitude with a_{exc} called quantum dots, the confinement of charge carriers involves and become predominant compared to Coulomb interaction. Thus, the total energy of excitons can be approached as [141]:

$$E_{exc} = E_g - 1.8\frac{e^2}{\varepsilon_0 \varepsilon_r a} + \frac{\hbar^2 \pi^2}{2a^2 m^*}. \tag{3.9}$$

The three terms represent the band gap of bulk CdSe, the Coulomb interaction and the confinement effect of carriers. Due to the confinement effect, the energy levels become discrete as shown in Figure 3.6 (b). The last two terms strongly depend on the radius of CdSe crystals a. Thus, the optical absorption and emission can be tuned via changing the dimension of nanocrystals a.

Deposition process and verification

Commercial CdSe nanocrystals Qdot ® 655 ITK^{TM} Carboxyl quantum dots are used for our study. The CdSe nanocrystals have a very large band of absorption and a relatively fine emission spectrum as shown in Figure 3.7 (a). The nanocrystals are firstly diluted 50 times in the 2% Polyvinyl alcohol (PVA) solution. The PVA is used for protecting nanocrystals and provides a stable layer for deposition. The sample with metallic nanostructures is firstly dipped in the thiol solution for 5 min. The thiol solution can protect metal structures from oxidizing and can also increase the viscosity on the metal surface so as to well stick nanocrystals on the metal. Before the spin-coating process, the nanocrystal solution suffers a fast shaking for at least 1 min so that the solution becomes homogeneous and no crystal associates together. Then nanocrystals are spin-coated on the sample with 2500 rpm speed for 1 min. The speed of spin-coating and the 2% PVA decide the thickness of nanocrystal layer which is measured around 50 nm. The last step is to check the deposition under the fluorescence microscopy. The best deposition should show a homogeneous red background like the inset image in Figure 3.7 (b) not like the image in Figure 3.7 (b) which has too many bright spots together. The verification is an important step for the quantification of fluorescence measurements.

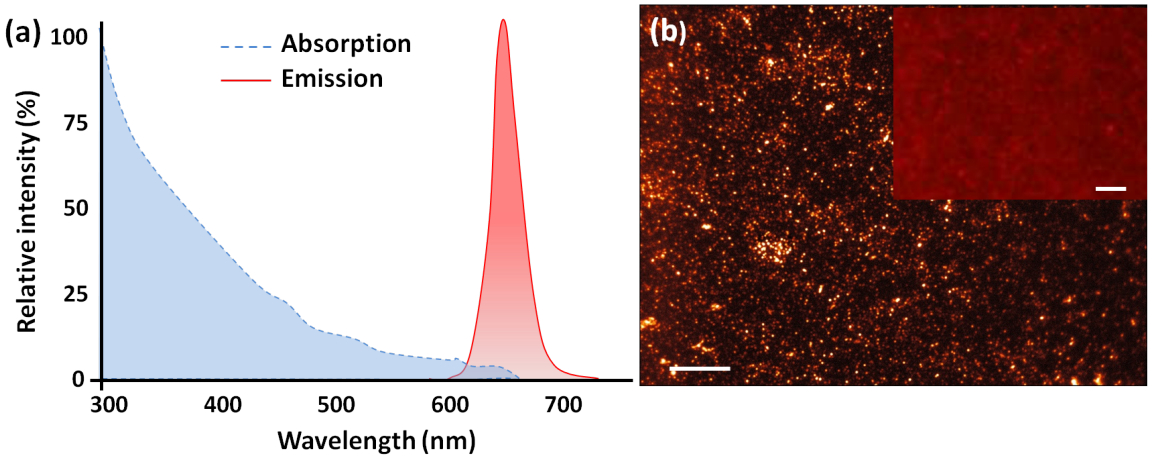

Fig. 3.7 (a) Absorption and emission spectra of CdSe nanocrystals Qdot ® 655 which are indicated by the blue dashed line and red solid line respectively. (b) The fluorescence images of CdSe nanocrystals deposited on the waveguide. The inset image shows a homogeneous deposition after spin-coating. The scale bars are both 25 μm.

In the next section, the fluorescence imaging as well as the lifetime measurement will be explained in detail. The fluorescence imaging for the nanocrystals deposited on the sample helps us not only for observing the confined waves in the waveguide but also for

understanding the properties of emitters in vicinity of metal structures which are associated to the fluorescence lifetime of nanocrystals.

3.2.3 Fluorescence imaging and lifetime measurement

The fluorescence imaging is easy to realize with the LRM. Firstly, the source is chosen as an appropriate wavelength for exciting the fluorophores. Here we use green laser (532 nm) or violet laser (405 nm) as the sources corresponding to the absorption spectrum of CdSe nanocrystals. Then the illumination light which is much stronger than the fluorescence signal is separated by using a dichroic mirror to replace the beam spliter (BS) or by adding a emission filter placed between the BS and the tube lens (TL) in Figure 3.5. The dichroic mirror is employed to reflect the illumination beam and let pass only the wavelength of the fluorescence and more longer wavelength. The emission filter has the similar principle and just blocks the wavelength around the excitation light. Finally, the fluorescence imaging is visualized by the CCD camera. There are two possibilities for more information of the analysis of fluorescence. The CCD camera can be replaced by a spectroscope which is used for measuring the emission spectrum. Furthermore, the CCD camera can be substituted by a system of avalanche photo diode (APD) as well for measuring the life time of nanocrystals.

The method for the life time measurement is called time-correlated single photon counting (TCSPC). The system contains a pulsed excitation laser, an APD and a fast electronics which provide a digital timing result. In practice, a periodic violet laser serves as the illumination source with 100 MHz frequency. The fluorescence excited by a short laser pulse is detected by an APD. The detection system consists of a pinhole placed the focus of lens L2 instead of the CCD camera and a set of lenses to refocus the fluorescence signal into the APD. Lastly, the fluorescence signal and the pulsed-laser signal are collected in the electronic module as shown in Figure 5.6. The principle of the signal analysis system works like a stopwatch. Once a pulsed laser comes, it starts to count the time and stops when a fluorescence signal is received. The time difference between the laser pulse excitation and fluorescence emission is measured for a huge number of cycles. More longer the measurement is carried out, more precise the result is. Subsequently, the data about time difference is sorted into a histogram (the number of counts v.s. time difference.) The width of the time bins typically corresponds to the resolution of the photon counter (several picoseconds) [142]. The life time of nanocrystal fluorescence can finally be determined by exponentially fitting histogram curves. Typically, the fluorescence system emits at different wavelengths and has different life times in the different time regions as well. Thus, the results of life time measurement are mostly described using a multi-exponential decay model [143, 144]. The results of the measurement will be explained in Chapter 5.

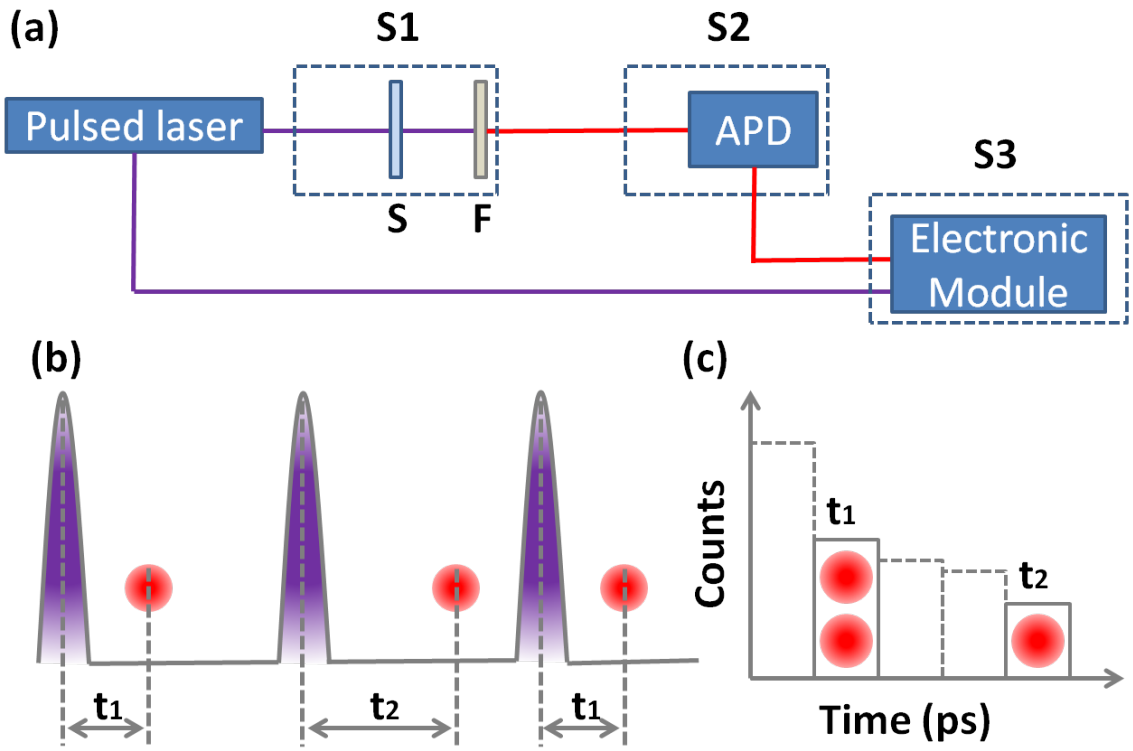

Fig. 3.8 Lifetime measurement of fluorescence. (a) Sketch of the setup for life time measurement. S1, S2 and S3 respectively represent the microscope system, signal collection system and signal analysis system. S and F in S1 denote substrate and emission filter which let pass the fluorescence signal. (b) The signal analysis in S3. The difference of time between excitation and emission can be calculated by using a photon counter like a stopwatch. (c) The data based on (b) within a large number of cycles is sorted into a histogram.

3.3 Polarization generation and analysis

In this section, the basic knowledge about polarization states of light will be explained including the polarization generation and analysis. Spin-controlled directional SPP generation and coupling of light into the waveguide both highly require the circular polarization. Thus, a relatively precise method with polarizer (P), half-wave plate (HWP) and quarter-wave plate (QWP) will be used for generating input circular polarization in the experiment. Due to the scattering of nanostructures on the sample, the output polarization states will be modified. In order to analyze and select the expected polarization states, two methods will be employed. The first one is to reverse the position of P, HWP and QWP in the output part to screen the specific polarization. The second one is to measure a set of values of intensities based on different polarization states which are called Stokes parameters. With the help of these values, the polarization states can be easily determined by constructing a Stokes vector. This

method can precisely measure the incoming polarization states when we need to analyze the ellipticity of the polarization.

3.3.1 Polarization states of light

Polarization is a basic properties of waves which reflects how the electric field oscillates during the propagation. In the nature, most light sources are unpolarized or partially polarized because several different spatial properties such as phases, polarization states and wavelength are mixed randomly [145]. We here consider the coherent plane waves which have sinusoidal oscillations along the direction of the wave vector. First of all, the linear polarization states will be described. Let's remind the electric field and magnetic field of a plane harmonic electromagnetic wave, which are expressed as:

$$\begin{aligned} \overrightarrow{E} &= \overrightarrow{E_0}\exp^{i(kz-\omega t)}, \\ \overrightarrow{H} &= \overrightarrow{H_0}\exp^{i(kz-\omega t)}, \end{aligned} \tag{3.10}$$

where we assume the wave propagates along z-axis. If the amplitudes E_0 and H_0 keep constant real vectors, this wave is linearly polarized. Typically, the direction of the electric field is designated as the direction of polarization. Thus, the projections of $\overrightarrow{E_0}$ on the x and y axis are both constant real values $E_0\cos\theta$ and $E_0\sin\theta$ respectively. The angle θ is defined as the angle between the electric field vector and the x axis.

Now, let's look at another special case which is the circular polarization. If two components of the electric field vector on the x and y axis has the same amplitudes E_0 (real number) in addition with a phase difference of $\pi/2$, the electric field vector can be expressed as:

$$\overrightarrow{E} = \hat{x}E_0\exp^{i(kz-\omega t)} + \hat{y}E_0\exp^{i(kz-\omega t+\sigma\pi/2)} = (\hat{x}+\sigma i\hat{y})E_0\exp^{i(kz-\omega t)}, \tag{3.11}$$

where $\hat{x}$ and $\hat{y}$ represent the unit vectors of x and y axis respectively. σ can be chosen as ± 1. Thus, the electric and magnetic field vectors rotate helically along the wave propagation which is depicted in Figure 3.9. By definition, the clockwise rotation of the electric field vector viewed along the propagation axis is named right-handed circular polarization (RCP) with $\sigma = -1$. On the contrary, the counterclockwise rotation is called left-handed circular polarization (LCP) with $\sigma = 1$. Note that the $\sigma = \pm 1$ are generally given as optical spin states of photons.

More general case of the polarization is when two components of the electric field amplitudes on the x and y axis don't have the same amplitudes but have a phase difference

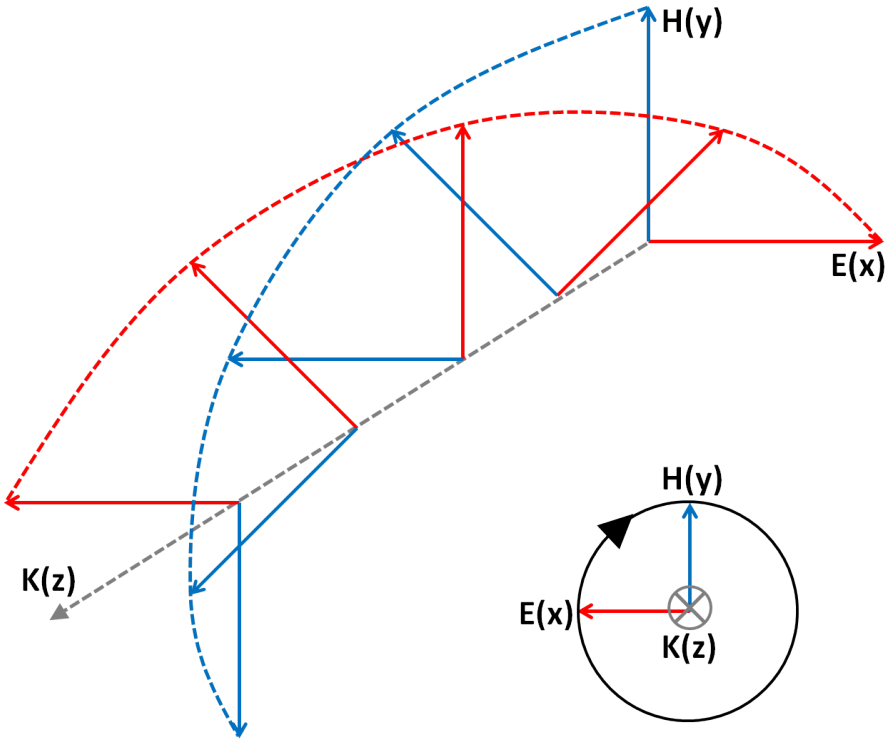

Fig. 3.9 Schematic diagram of the right-handed circular polarization state (RCP). The red and blue solid lines are designated as the electric field and magnetic field vectors respectively. The red and blue dashed lines indicate the rotation of their field vectors. The dashed grey line indicates the direction of the wave vector K(z). The inset is a view from the backside of the wave which is to say the wave is propagating into the plane as denoted with a cross. The black flash show the rotation direction which corresponds to RCP here.

(exclude $\pm\pi$). It is called elliptical polarization and its electric field vector of can be expressed as:

$$\overrightarrow{E} = \hat{x}E_x \exp^{i(kz-\omega t)} + \hat{y}E_y \exp^{i(kz-\omega t+\xi)}, \tag{3.12}$$

where the real number E_x and E_y represent the electric field amplitudes on x and y axis and ξ denotes a phase difference. As the matter of effect, any polarization can be classified into the expression above. Thus if $\xi = 0, \pm\pi$, it expresses a linear polarization, whereas if $\xi = \pm\pi/2$ and $E_x = E_y$, it presents a circular polarization.

3.3.2 Optical elements for generating polarization

As we mentioned before, most of light sources are unpolarized. A polarizer (P) is an optical filter which can produce linearly polarized light from unpolarized light. Typically, there are

two kinds of linear polarizers which are absorptive and beam-splitting polarizers. Beam-splitting polarizers rely on the properties of double refraction of birefringent materials which is to say the polarizers can split the incident beam into two beams with two linear orthogonal polarization along two directions (reflection and transmission). The absorptive polarizers make use of the effect of anisotropic optical absorption which is to say the unexpected polarization states can be blocked through the absorptive polarizers. In the experiment, we use this kind of absorptive polarizers called wire-grid polarizers which contain a series of parallel fine metallic wires. When the incident unpolarized beam interacts with the wire grid, the wave component aligned parallel to the wires is easier to oscilate free electrons along the length of wires than the perpendicular component. Thus, most of light is reflected and absorbed. The perpendicular component can not easily interact the free electrons along the width of wires and therefore most of light is able to pass through the grid [146]. The direction of nearly 100% transmission is defined as a transmission axis of the polarizer which is perpendicular with the wire grid.

After having the linear polarization, we introduce another optical element called wave plate which is used for generating a phase difference between two orthogonal components of linearly polarized light. A typical wave plate is made of a doubly refracting transparent crystal such as calcite or mica [147]. The principle is similar to the aforementioned beam-splitting polarizers. Doubly refracting crystals are able to differ for the directions of polarization due to their anisotropic index of refraction. Normally, the crystal is cut into a slab as the wave plate. An axis of maximum index n_1 and an axis of minimum index n_2 lie in the plane of the slab which correspond to the slow axis and fast axis [145]. If the slab has a homogeneous thickness d, the optical thicknesses for light polarized in the direction of the slow and fast axis are $n_1 d$ and $n_2 d$. The phase shift ξ adjusted by wave plates can be deduced as:

$$\xi = \frac{2\pi}{\lambda_0}(n_1 - n_2)d, \tag{3.13}$$

where λ_0 denotes the vacuum wavelength. For the half-wave plate and quarter-wave plate, the phase shifts ξ are fixed at π and $\pi/2$ respectively corresponding to one-half and one-quarter wavelengths. Thus, the thicknesses of these two wave plates can be determined.

The practical optical elements for producing circularly polarized light is sketched in Figure 3.10. The incident beam impinge in this optical system with unpolarized light. The light is firstly filtered as the linear polarization along the transmission axis (vertically aligned) of a polarizer (P). Then the fast axis of a half-wave plate (HWP) is placed with an angle $\theta_1 = 22.5^\circ$ away from the incoming linear polarization. For linear polarization, the HWP serves to rotate the polarization vector with an angle $2\theta_1$. Therefore, the polarization is turned to $2\theta_1 = 45^\circ$ with respect to the incoming vertically linear polarization after the HWP.

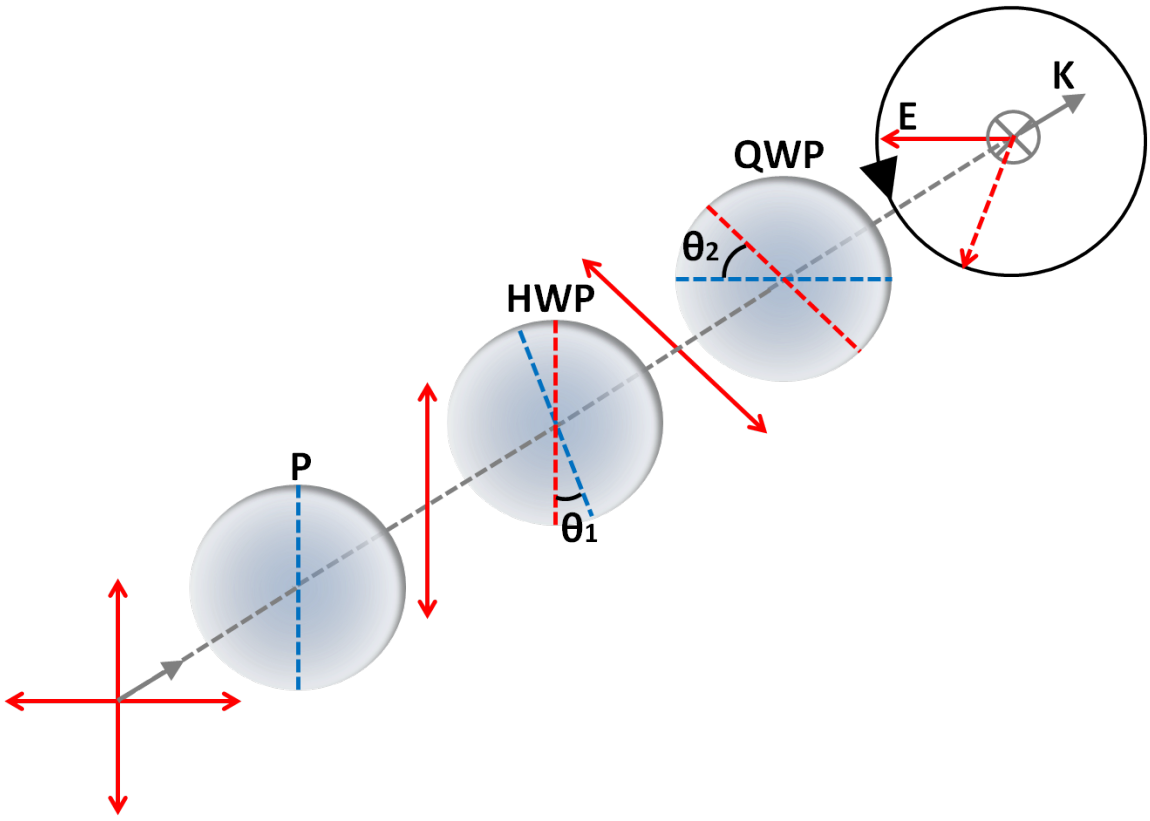

Fig. 3.10 Generation of circular polarization. The grey line with arrows represents the direction of wave propagation. The red lines designate as the electric field polarization. The bule dashed lines on P and HWP/QWP indicate the transmission axis and the fast axis respectively.

The fast axis of a quarter-wave plate (QWP) is horizontally placed and an angle between this axis and the incoming polarization vector is defined as θ_2. If $\theta_2 = 45°$, the incident linearly polarized light can be resolved into two orthogonal components with the same amplitude but a phase difference of $\pi/2$. Hence a circularly polarized emerging light is generated. The sense of rotation like left-handed (LCP) or right-handed circular polarization (RCP) depends on the θ_2. If $\theta_2 = +45°$ (on the left side of the fast axis) like in Figure 3.10, it generates LCP. On the contrary, if $\theta_2 = -45°$ (on the right side of the fast axis), it generates RCP.

Technically, the HWP is not mandatory for producing circular polarization. Here we use the HWP just to avoid turning the P or the QWP which are not as precise as the HWP. When a specific polarized light impinges on the sample with nanostuctures, the polarization state would be modified as a result of the diffraction. Concerning the analysis of output polarization states, two methods were carried out for our experiment. The convenient one is to reverse the sequence of the P, the HWP and the QWP. Here we use only a QWP and a P for

a roughly qualitative analysis. When a circularly polarized light pass through the QWP, the phase difference between two orthogonal components of the electric field will be removed and the emerging light will be linearly polarized with $\theta_2 = \pm 45°$. Then this specific linear polarization can be analyzed by the P. However, this method is not sufficient for the light with elliptical polarization. A more precise method will be used and introduced in the next section.

3.3.3 Stokes parameters

Measurement of the Stokes parameters of light is an alternative way to quantitatively analyze the light polarization states. An Irish scientist George Stokes proposed four parameters (I, Q, U, V) to completely describe the properties of light polarization and even for unpolarized light. In order to determine these four parameters, at least six intensities have to be measured. The output light is firstly analyzed by four linear polarization which are $\phi = 0°, 45°, 90°$ and $135°$. ϕ is defined as the angle between the transmission axis of the polarizer and the vertical axis of the system. Subsequently, the light is separately analyzed by a LCP and a RCP basis. The way is like we mentioned before to place a quarter-wave plate and to filter with a polarizer. Thus, these four Stokes parameters can be experimentally determined by [148]:

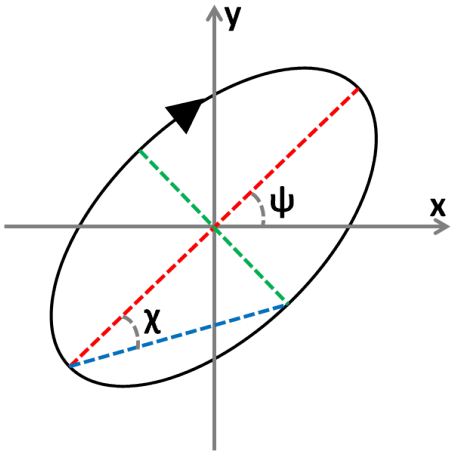

Fig. 3.11 The spherical coordinates for Stokes parameters are expressed in the Cartesian coordinates. The red and green dashed lines indicate the long axis and short axis of the ellipse.

$$
\begin{aligned}
I &= I(0^\circ) + I(90^\circ), \\
Q &= I(0^\circ) - I(90^\circ) = Ip\cos 2\psi \cos 2\chi, \\
U &= I(45^\circ) - I(135^\circ) = Ip\sin 2\psi \cos 2\chi, \\
V &= I(RCP) - I(LCP) = Ip\sin 2\chi.
\end{aligned}
\tag{3.14}
$$

where the second parts of Q, U and V correspond to the elliptic polarization parameters in the Cartesian coordinate system (x, y, z) in which x and y are perpendicular to the direction of light propagation z. p is defined as the degree of polarization, which is equal to $I_{pol}/(I_{pol}+I_{unpol})$. The angle ψ and χ represent the incline with the x axis and the apex angle between the long semi-axis and short semi-axis of ellipse respectively which are indicated in Figure 3.11. As the matter of fact, the Ip, ψ and χ are the spherical coordinates of the Poincaré sphere of the last three vectors of Stokes parameters Q, U, V. When these four Stokes parameters are measured, the rest parameters Ip, ψ and χ can be deduced as:

$$
\begin{aligned}
p &= \frac{\sqrt{Q^2+U^2+V^2}}{I}, \\
2\psi &= \arctan\frac{U}{Q}, \\
2\chi &= \arctan\frac{V}{\sqrt{Q^2+U^2}}.
\end{aligned}
\tag{3.15}
$$

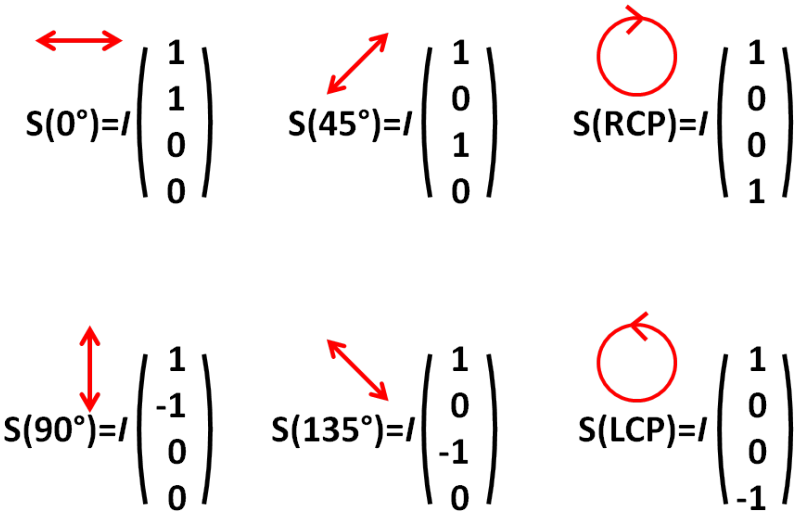

Fig. 3.12 Stokes vectors for six special polarization states.

In addition, the sign of V decides the direction of polarization. By definition of V, the sign $+$ and $-$ represent the RCP and LCP respectively. It is convenient to arrange these 4 Stokes parameters as a column matrix called the Stokes vector. Some special polarization states with Stokes vectors are shown in Figure 3.12.

In conclusion for this chapter, we firstly introduce the LRM which is a very efficient way to detect SPPs in the far field. The experimental setup for the direct plane and Fourier plane imaging is described in details. Secondly, the dark field and fluorescence imaging systems are presented which will be used for studying the confined light in the waveguide. Lastly, the methods for generating and analyzing the circular polarization are well explained. In the next chapter, we will report the first-part results about the spin-controlled directional SPP coupling and all the images are taken under the LRM.

Chapter 4

Spin-controlled directional and singular surface plasmon polariton generation

Abstract: In this chapter, we describe the implementation of leakage radiation microscopy to probe the directionality and singularity of the propagative Surface Plasmon Polaritons (SPPs). The spin-driven directional coupling as well as the vortex generation of SPPs by T-shaped and Λ-shaped apertures is demonstrated and optimized experimentally. An analytical model based on a multidipolar representation of T-shaped and Λ-shaped apertures is developed to support the experimental findings.

Contents

4.1 Spin-controlled directional SPP coupling

In this section, we demonstrate experimentally spin-driven directional coupling of surface plasmon polaritons (SPPs) by nanostructures built with T-shaped and Λ-shaped apertures. Specifically, a rectangular array made of chiral T-shaped or achiral Λ-shaped nanoapertures serves as a direcional coupler to induce unidirectional propagation of SPPs. The recorded leakage radiation microscopy (LRM) images in the Fourier space lead to direct determination of the ratio of SPP intensities along two opposite directions of propagation, defined as the directivity *D*. Thereby, quantitative comparison between the directional coupling efficiency induced by a T-shaped aperture array and that of a Λ-shaped aperture-based array can be achieved. One important finding, which confirms previous works, is that both T- and Λ-shaped slit arrays induce SPP directionality resulting from the spin-orbit coupling mechanism. Our work provides therefore a unified perspective for Λ- and T-shaped systems by clarifying the role of phase and symmetry. Furthermore, to justify this result, we introduce an analytical theory that models the radiated field by each individual rectangular aperture by a pair of electric dipoles. Our analytical approach provides physical insights of the mechanism at play without requiring numerical solutions [149]. Lastly, the optimal structure for the highest directivity of SPP coupling is achieved based on our theoretical section.

4.1.1 Array of T-shaped and Λ-shaped apertures

The directional couplers considered here are milled using a focused ion beam (FIB) on a 50 nm thick gold layer on top of the glass substrate. The T- and Λ- like structures both consist of two same elementary rectangular apertures as shown in Figure 4.1 (a) and (b). Each elementary slit has 200 nm long (L) and 50 nm wide (W) in which the width has ± 10 nm uncertainty due to the imprecision of FIB fabrication under 50 nm. As for the T-shaped aperture, two slits are arranged orthogonal with each other and tilted with an angle $\alpha = 45^\circ$ from the Oy axis. Thus the T-shaped aperture geometrically show a chiral structure with respect to the Oy axis. On the contrary, the Λ-shaped aperture contains two slits placed on the two sides of a symmetric axis and separated with an angle 2α. The angle α is called the apex angle for the Λ-shaped aperture which we define as the half angle of the total angle between two elementary slits and it is firstly considered as 45°.

The distance (D) spacing two rectangular slits is fixed at 210 nm and 150 nm respectively in the case of T-shaped and Λ-shaped structures. Experimentally, we have tried different values for spacing D which range from 150 nm to 250 nm for T-shaped and from 130 nm to 250nm for Λ-shaped structures. The maximum directionalities (by keeping the other parameters fixed) for T-shaped and Λ-shaped structures lie in 210 nm and 150 nm. Theo-

retically, These two values corresponds to $k_{spp}D/\sqrt{2} = \pi/2$ and $k_{spp}D = \pi/2$ respectively for T-shaped and Λ-shaped structures where k_{spp} is the real part of the SPP wavevector. Such a phase constraint provides the necessary condition for SPP directionality, as it will be explained in the part of the theoretical model.

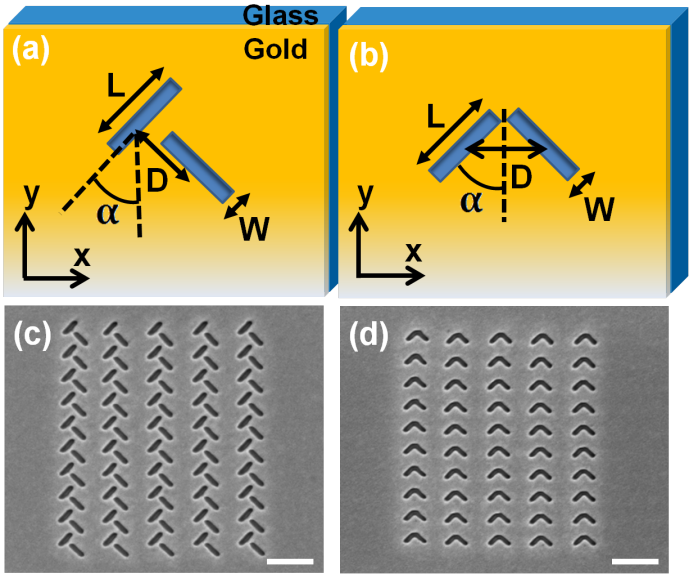

Fig. 4.1 T-shaped and Λ-shaped directional couplers. (a, b) Schematic diagrams of a single T-shaped and Λ-shaped aperture (top view). (c, d) Scanning electron microscopy (SEM) images of arrays made of 50 single T- and Λ-shaped apertures respectively. The scale bars are both 600 nm.

The T-shaped and Λ-shaped apertures are further arranged in 5×10 arrays as shown in Figure 4.1 (c) and (d) with a horizontal pitch of 600 nm ($\cong \lambda_{spp}$) to achieve SPP resonant excitation in the Ox direction and a vertical pitch of 300 nm ($\cong \lambda_{spp}/2$) for preventing SPP propagation in the Oy direction (i.e., at least up to the second diffraction order). There are three advantages for using an array instead of a single T-shaped or Λ-shaped aperture. Firstly, the size of a single aperture is too small compared with the beam size (around 2 μm). The normal incident illumination in the center and the observation are tough to realize. The size of a 5×10 array is almost the same as the beam size. Thus, the array is easy to implement for observation under LRM and for alignment with the incident laser. Secondly, the array can enhance the SPP signal so that we could easily measure the SPP intensity both on the direct and the Fourier plane. Thirdly, by modifying the array size parameters (horizontal and vertical periods) the SPP propagation can be fixed only along the Ox direction so as to eliminate the signal influence from the other directions.

The plasmonic arrays are then illuminated by a weakly focused laser at 633 nm wavelength. The incident beam is prepared either in right-handed circular polarization (RCP)

or left-handed circular polarization (LCP) states. The excited SPPs are then recorded in the far-field on a CCD camera following the LRM characterization method. We firstly present in Figure 4.2 (a), (b) LRM images recorded in the direct plane (DP) corresponding to the excitation of the array of T-shaped apertures by LCP and RCP incident beams as indicated by the white arrow. No polarization analysis is performed at the output part. We point out that the DP images are taken with an opaque mask (M) on the Fourier plane (FP). The mask is designed with a circle with the radius around 0.9 NA aiming at filtering the incident light. The T-shaped coupler as well as the Λ-shaped with $\alpha = 45^\circ$ couple clearly exhibits spin-dependent SPP directionality and the DP images of the T-shaped coupler are demonstrated in Figure 4.2 (a), (b) (the DP images of the Λ-shaped coupler are same with T-shaped's and thus are not shown here). We observe a bright trace corresponding to leaky SPPs that propagate either to the left upon LCP or to the right direction upon RCP excitation. Note that the fringes are due to interferences between the leakage radiation and the incident beam directly transmitted through the sample.

In order to characterize the directional coupling efficiency (directionality) of our plasmonic system, we introduce a quantitative criterion such as the directivity contrast (V), which defines the capacity of the system to couple an incident spin into SPPs propagating in a given direction. It is defined as:

$$V_\sigma = \frac{|I_{\sigma,+} - I_{\sigma,-}|}{I_{\sigma,+} + I_{\sigma,-}}, \tag{4.1}$$

with $I_{\sigma,d}$ the SPP intensity launched upon $\sigma = -1$ (RCP) or $\sigma = +1$ (LCP) incident spin and propagating towards $d = +k_x$ (right) or $d = -k_x$ (left) direction. Note that $0 \leq V \leq 1$. In fact, V is clearly a fringe visibility which explains why we denoted V here.

Owing to the widespread intensity span which decreases exponentially with the distance, the determination of the directivity in the DP can not be clearly defined. On the contrary, as mentioned earlier, the SPP intensity propagation towards the given direction $\pm k_x$ translates into keen intensity peaks in the FP as depicted in Figure 4.2(c)-(f). These intensity peaks allow us to experimentally determine the directivity according to equation 4.1. Note that we remove the mask on the FP for taking the FP images and thus the central bright spot originates from the incident light directly transmitted through the sample.

In Figure 4.2 (g) and (f), we provide intensity cross-sections performed along the center lines (as indicatetd in Figure 4.2 (c)) of Figure 4.2 (c)-(f). We retrieve the aforementioned central lobe as well as the two side peaks corresponding to propagating SPPs. When the arrays are excited by $\sigma = +1$ (black curves), one clearly measures an intense SPP peak towards the negative wavevectors $-k_x$ while it appears very weak towards $+k_x$ ($I_{+1,+} \ll I_{+1,-}$). Inversely, upon $\sigma = -1$ (red curves), propagation towards $-k_x$ exhibits an attenuated intensity peak

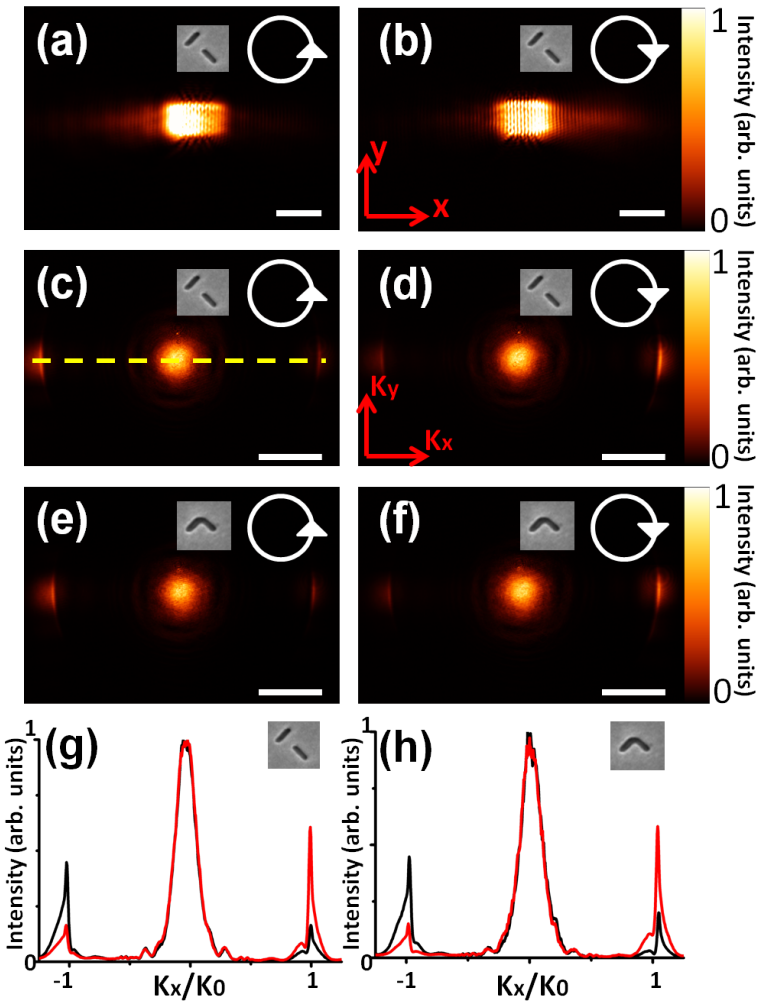

Fig. 4.2 Images of T-shaped and Λ-shaped apertures by LRM. (a), (b) The DP images of T-shape coupler are recorded respectively upon LCP and RCP as indicated by the white arrows. (c), (d) The FP images of T-shape coupler correspond to the DP images of (a), (b). (e), (f) The FP images of Λ-shaped coupler are also recorded upon LCP and RCP respectively. The scale bars in (a), (b) and (c)-(f) are 3 μm and $0.5k_0$ NA. (g), (h) The intensity cross-section profiles of (c)-(f) are taken along the center lines as indicated the yellow dashed line in (c). The cross-section profiles in (c), (d) ((e), (f)) are indicated in (g) ((h)) with black and red curves respectively. The insets of each image are the elements forming the arrays.

compared to that of $+k_x$ ($I_{-1,+} \gg I_{-1,-}$). By using equation 4.1, the intensity contrast provided by Fourier imaging allows for determining the directivity $V = 0.59 \pm 0.09$ for the array of T-shaped apertures and $V = 0.52 \pm 0.11$ for the array of Λ-shaped apertures with $\alpha = 45°$. We thus have shown both plasmonic devices (T-shaped and Λ-shaped couplers) exhibit a clear photonic spin-control of the SPP directivity along a metal film. Furthermore, LRM is shown to provide a direct method for mapping this SPP directivity. This method

becomes quantitative in the Fourier plane where the contrast between the SPP peaks for propagation along $\pm k_x$ directions can be precisely recorded (we point out that working in the Fourier space is here mainly a practical advantage since it is also possible to work directly in the x-y plane [11, 134]).

4.1.2 Symmetric properties of T-shaped and Λ-shaped apertures

From the result of the last section, the T-shaped and Λ-shaped apertures have been shown the same effect on the directionality. An interesting issue about the mirror symmetry draws our attention before studying the mechanism of these two kinds of apertures. The principle of the mirror symmetric analysis is sketched in Figure 4.3. The T-shaped and Λ-shaped couplers are all simplified with a 2 by 2 array. Now we try to predict the behavior of each array of apertures obtained by mirror symmetry with respect to the Oy axis. The achiral Λ-shaped coupler is simple to predict because the mirror symmetric structure is invariant along the Oy axis. Thus, if we know that the array of Λ-shaped apertures shows left directionality upon LCP excitation shown in Figure 4.3 (1), we can intuitively deduce that this array should exhibit right directionality upon RCP excitation shown in Figure 4.3 (2) according to a mirror-symmetry-based reasoning.

However, the chiral T-shaped coupling lead to a more complicated situation. The arrays in Figure 4.3 (3) and (4) are called left-tilted and right-tilted T-shaped apertures respectively. If we know that the array of left-tilted apertures shows left directionality upon LCP excitation, its mirror symmetrical structure, the array of right-tilted apertures should exhibit right directionality upon RCP excitation. Remarkably, no conclusion can be drawn on the response of the array of left-tilted apertures upon RCP illumination in Figure 4.3 (6) and its mirror symmetrical structure in Figure 4.3 (5). Experimentally, the SPPs generated by the array of left-tilted apertures upon RCP illumination propagate to the right (see Figure 4.2 (b)). Accordingly, its mirror image should induce left propagation upon LCP illumination as illustrated in Figure 4.3 (5). These experimental results reveal the similarity between Λ-shaped and T-shaped apertures, which is to say no matter the chiral left-tilted or right-tilted T-shaped apertures, they work exactly the same as the achiral Λ-shaped apertures. If we compare with Figure 4.3 (3) and (5), the same left directionality is predicted. This has been confirmed experimentally and the FP images are shown in Figure 4.4.

From the Figure 4.4, we confirm that both the left-tilted and right-tilted T-shaped apertures have the same response for the same polarization states of the incident laser and the spin-based directionalities are identical with Λ-shaped apertures. It means that the directionality is not dependent on the chirality of the structures. Specifically, the array considered in the inset of Figure 4.4 (a) involves closely packed T-shaped apertures such as the distance between two

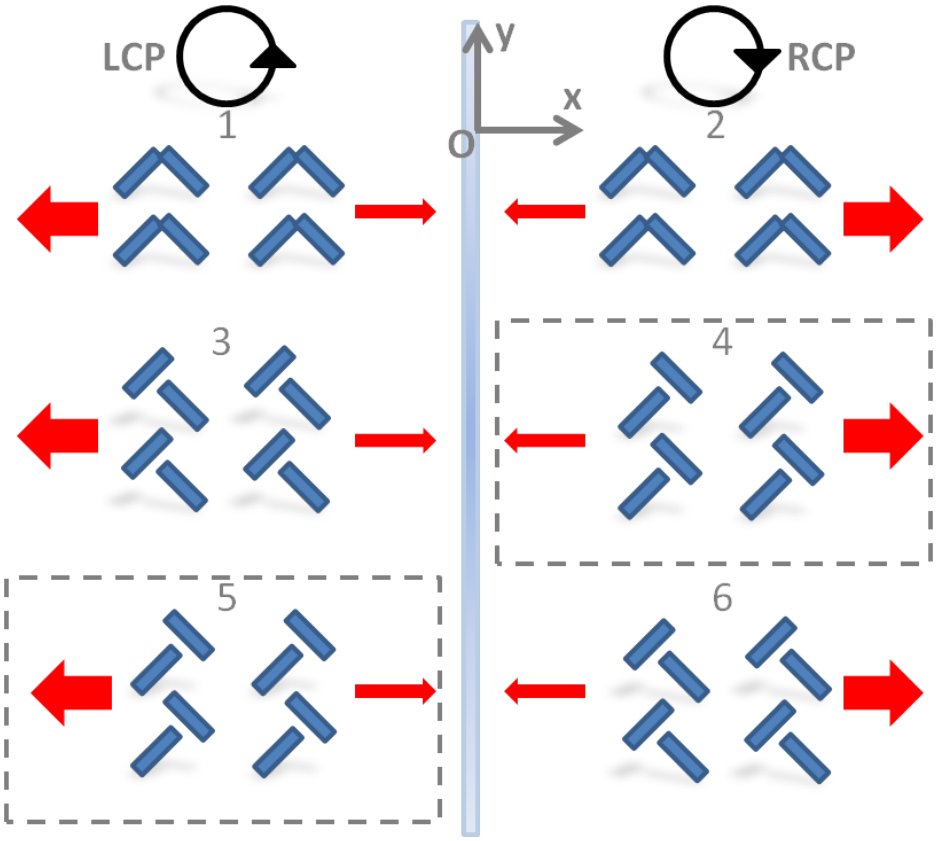

Fig. 4.3 Schematic diagram illustrating the mirror-symmetry analysis for Λ-shaped and T-shaped apertures. The arrays are illuminated by a LCP or a RCP beam indicated by the black arrows on the left or right column. The thick and thin red arrows represent the predominant and minor directions of SPP propagation respectively.

Ts equals merely the distance between two slits in a T. Therefore, in each column of the array, there is approximately an equal number of T apertures and their mirror images. Consequently, for an infinite array in the Oy direction, the geometrical chirality of the whole structure vanishes. If this geometrical chirality of the array was a key issue here, then apparently the directionality observed should depend only on the first and last rows of the array, and this would make the effect very phase sensitive (e.g., small displacements of the excitation beam). Actually, the system is very robust, meaning that the main issue is not the handedness of the T-shaped apertures.

However, the symmetric break is necessary to induce the SPP directionality. The only reason is attributed to the spin-orbit coupling with the dipoles excited by the slits. In other words, the interaction between the polarized light and the two slits of a Λ-shaped or T-shaped aperture generates a phase difference that breaks the symmetry with respect to the Oy axis. In order to understand thoroughly the physics involved in the spin-orbit coupling of SPPs,

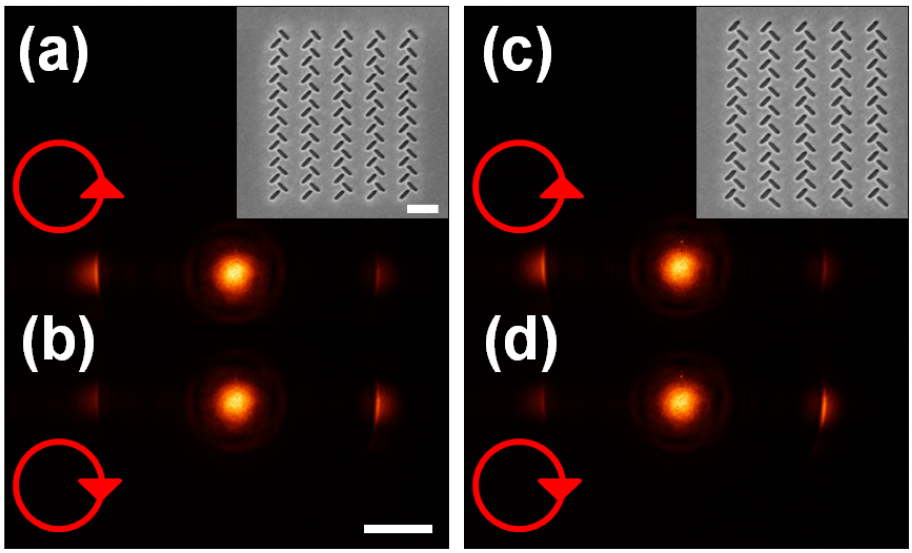

Fig. 4.4 Fourier plane images for right-tilted (a), (b) and left-tilted (c), (d) T-shaped apertures. The scale bar value is $0.5k_0$ NA. The polarization states of the laser illumination are indicated by the red arrows which represent LCP in (a), (c) and RCP in (b), (d) respectively. The inset in (a), (c) are SEM images of the coupler systems with a scale bar value 600 nm.

we develop an analytical model based on a two-dipole representation of the coupler system which will be introduced in the following section. Of course, the equivalence between T-shaped and Λ-shaped apertures is not complete, and we can find differences if we consider SPP propagation along other directions in the Fourier plane, i.e.,the k_y axis. Thus, for the single elemental T-shaped and Λ-shaped apertures, we carry out a simulation based on the theoretical model which will be explained in the next section.

4.1.3 Multidipolar model of T-shaped and Λ-shaped apertures

Here, we detail the analytical model of two pairs of SPP dipoles for describing spin-controlled directional propagation of SPPs induced by Λ-shaped and T-shaped apertures. In the proposed model, SPPs radiated by a rectangular aperture is approximately that of a pair of in-plane SPP dipoles formed by a major-axis dipole (orthogonal to aperture long axis) and a minor-axis dipole (orthogonal to aperture short axis) as indicated in Figure 4.2 (a), (b) with the red and green arrows respectively.

On the one hand, let us consider the case of an elementary Λ-shaped structure. It is made of two rectangular apertures making an apex angle α with (Oy) and positioned at $\overrightarrow{x}_1 = (0,0)$ and $\overrightarrow{x}_2 = (-D,0)$ (see Figure 4.2 (a)). The unit vectors of each dipoles are defined by $\widehat{n}_1 = (\cos\alpha, \sin\alpha)$, $\widehat{n}_{1\perp} = (-\sin\alpha, \cos\alpha)$, $\widehat{n}_2 = (-\cos\alpha, \sin\alpha)$, $\widehat{n}_{2\perp} = (\sin\alpha, \cos\alpha)$. An

incident circularly polarized electric field $\vec{E}_\sigma = (\hat{x} + i\sigma\hat{y})/\sqrt{2}$ with handedness $\sigma = -1$ and $\sigma = +1$ for right-handed circular polarization (RCP) and left-handed circular polarization (LCP) respectively excites the structure. The dipole moment corresponding to the launched SPPs by each rectangular slit (m = 1, 2) is given by:

$$\vec{\mu}_{m,\sigma} = \eta[(\vec{E}_\sigma \cdot \hat{n}_m)\hat{n}_m + \beta(\vec{E}_\sigma \cdot \hat{n}_{m\perp})\hat{n}_{m\perp}], \tag{4.2}$$

with

$$\vec{\mu}_{1,\sigma} = \frac{1}{\sqrt{2}}\eta[(\cos\alpha + i\sigma\sin\alpha)\hat{n}_1) + \beta(-\sin\alpha + i\sigma\cos\alpha)\hat{n}_{1\perp}], \tag{4.3}$$

and

$$\vec{\mu}_{2,\sigma} = \frac{1}{\sqrt{2}}\eta[(-\cos\alpha + i\sigma\sin\alpha)\hat{n}_2) + \beta(\sin\alpha + i\sigma\cos\alpha)\hat{n}_{2\perp}], \tag{4.4}$$

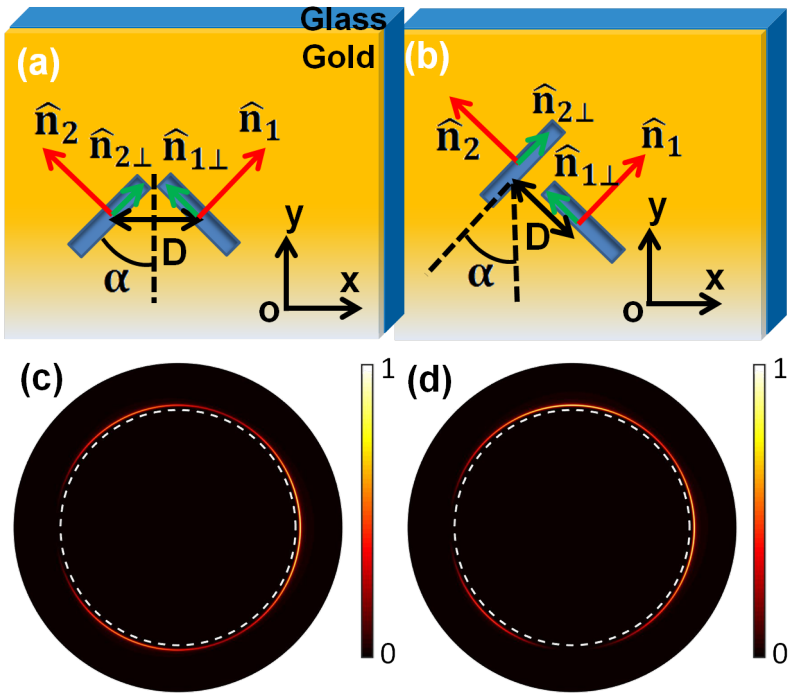

Fig. 4.5 (a), (b) Multidipolar representation (top view) of a single Λ-shaped and T-shaped aperture. (c), (d) Simulated results in the Fourier plane for a single Λ-shaped and T-shaped aperture respectively upon the RCP excitation with $\beta = 0$ in the model.

where η is the polarizability of the major-axis dipole which depends on the geometry of the slit. β $(0 \leq \beta < 1)$ describes the weighted contribution of the minor-axis dipole with

respect to the major-axis dipole in the SPP launching. In the Fourier plane, the radiated SPP field upon an excitation with spin state σ is defined by

$$\overrightarrow{E}_{\sigma}^{spp}(\overrightarrow{k}) = \sum_{m} \widehat{k}(\overrightarrow{\mu}_{m,\sigma} \cdot \widehat{k}) e^{i\Phi} F_{spp}(k), \tag{4.5}$$

where $\overrightarrow{k}$ represents the in-plane wave vector of radiated field and $\widehat{k}$ denotes the unit vector in the Fourier plane (FP). $F_{spp}(k) \simeq 1/(k - k_{spp})$ which is defined as a distribution of SPP radiated waves detected in the FP, which has a Lorentzian line shape, depicting the narrow ring-like shape peaked on the SPP wavevector k_{spp}. Owing to the strongly peaked resonance associated with $F_{spp}(k)$, the spatial phase factor $\Phi = -\overrightarrow{k} \cdot \overrightarrow{x}_m$ now depends directly on the SPP wave vector $\overrightarrow{k}_{spp}$ (assuming k_{spp} here to be a real number) such as $-\overrightarrow{k}_{spp} \cdot \overrightarrow{x}_m$. These phase provide the key ingredient for the coherent SPP-induced spin-control studies in this work. By inserting equation 4.3 and 4.4 in equation 4.5, the SPP field launched by a single Λ-shaped aperture along the direction of propagation $\widehat{k}_{x\pm}$ becomes:

$$\overrightarrow{E}_{\sigma,k_{x\pm}}^{spp}(k) = F_{spp}(k)[(\overrightarrow{\mu}_{1,\sigma} \cdot \widehat{k}_{x\pm}) e^{\pm i k_{spp} \cdot 0} + (\overrightarrow{\mu}_{2,\sigma} \cdot \widehat{k}_{x\pm}) e^{\pm i k_{spp} \cdot D}] \cdot \widehat{k}_{x\pm}. \tag{4.6}$$

Assuming $k_{spp} \cdot D = \pi/2$, the above equation is simplified as:

$$\overrightarrow{E}_{\sigma,k_{x\pm}}^{spp}(k) = \pm \frac{\eta}{\sqrt{2}} F_{spp}(k) \cos^2\alpha \cdot C_{\sigma,\pm} \cdot \widehat{k}_{x\pm}, \tag{4.7}$$

where we introduce $C_{\sigma,\pm}$ which represents the coupling efficiency for a spin state σ along $\widehat{k}_{x\pm}$. It describes the interactions between the incident spin σ and the nanostructure leading to unidirectional propagation of SPPs along $k_{x\pm}$. It is given by:

$$C_{\sigma,\pm} = 1 \pm \sigma \tan\alpha + (\sigma \tan\alpha \pm 1)i + \beta[1 \mp \sigma \tan\alpha - (\sigma \tan\alpha \mp 1)i]. \tag{4.8}$$

From $I_{\sigma,\pm} = \| \overrightarrow{E}_{\sigma,k_{x\pm}}^{spp} \|^2$ which is the SPP intensity in the Fourier space at the given direction of propagation and upon spin state σ, we can deduce the directivity V associated to a Λ-shaped aperture:

$$V_{\sigma} = \frac{|I_{\sigma,+} - I_{\sigma,-}|}{I_{\sigma,+} + I_{\sigma,-}} = \frac{2\beta(1-\beta)\tan^3\alpha + 2(1-\beta)\tan\alpha}{\beta^2 \tan^4\alpha + (1+\beta^2)\tan^2\alpha + 1}. \tag{4.9}$$

On the other hand, in the case of a single T-shaped aperture in the model, the apex angle α is fixed at 45° and the positions of two centers of the slits are slightly modified which are $\overrightarrow{x}_1 = (0,0)$ and $\overrightarrow{x}_2 = (-D/\sqrt{2}, D/\sqrt{2})$. Analogously, assuming $\Phi = k_{SPP} \cdot D/\sqrt{2} = \pi/2$, the eq 4.5 reduces as:

$$\overrightarrow{E}^{spp}_{\sigma,k_{x\pm}}(k) = \pm\frac{\eta}{2\sqrt{2}}F_{spp}(k)\cdot C_{\sigma,\pm}\cdot\widehat{k}_{x\pm}, \tag{4.10}$$

with

$$C_{\sigma,\pm} = 1\pm\sigma+(\sigma\pm1)i+\beta[1\mp\sigma-(\sigma\mp1)i]. \tag{4.11}$$

The directivity V of SPPs for a single T-shaped aperture is thus given by:

$$V_\sigma = \frac{1-\beta^2}{1+\beta^2}. \tag{4.12}$$

Up to now, our "multidipolar" representation for both a single Λ-shaped and T-shaped aperture has been explained. Noteworthy, D, α and β strongly influence the directivity V in our model. If the wavelength of an incident light for exciting SPPs is choosen, k_{spp} is fixed. The only variable to change the spatial phase is the distance D between two centers of each slit. Assuming a given D satisfies the spatial phase $\Phi = 0$ or $n\pi$ (n is an integer), we find the terms of σ are all disappeared and the coupling efficiency $C_{\sigma,\pm}$ keeps a constant value. It means that the SPP intensities on the left and right do not depend on the spin states any more and keep the same intensity. When $\Phi = \pi/2$ or $(\pi/2+n\pi)$, the coupling efficiency C becomes strongly spin-dependent and SPPs on each side can reach the maximum or minimum intensity upon a chosen spin state. Thus, we determine the distance D spacing two rectangular slits as 150 nm and 212 nm in the case of Λ-shaped and T-shaped respectively such that based on the theoretical model, the phase becomes $\Phi = \pi/2$.

Once the spatial phase is well chosen at $\pi/2$, the spin-controlled directionality can be achieved. The factors α and β only influence the maximum directivity V that we can reach. Comparing with the equation 4.7 and equation 4.10 based on the theoretical analysis, we find that a single T-shaped aperture generates the same SPP field as the field generated by a single Λ-shaped aperture with the apex angle $\alpha = 45^\circ$ along the $k_{x\pm}$. However, the SPP fields along the $k_{y\pm}$ are different (see Figure 4.5 (c), (d)). The figures are the simulated results obtained with a MATLAB code based on our model. The excited SPP field of a Λ-shaped aperture has a symmetric intensity with respect to Ox axis but not for a T-shaped aperture. This discrepancy results from the center position of x_1 and x_2. The achiral Λ-shaped aperture has only a different distance D along $k_{x\pm}$ but the chiral T-shaped aperture has two differences $D/\sqrt{2}$ along $k_{x\pm}$ and $k_{y\pm}$. As we has already chosen the values D for the phase $\Phi = \pi/2$ in the two cases, the unidirectional coupling of SPPs occurs only along $k_{x\pm}$ for the Λ-shaped aperture but along both $k_{x\pm}$ and $k_{y\pm}$ for the T-shaped aperture. Thus, we prove the similarity of these two kinds of apertures along $k_{x\pm}$ from both theoretical and experimental results.

Besides, we emphasize that equation 4.10 is slightly modified if we consider not a single aperture but the full array. Mainly, we have to include an additional form factor that modifies the 2D radiation pattern in the FP. However, this does not impact the main reasoning since we focus our attention on propagation in the $k_{x\pm}$ direction. Furthermore, we point out that the previous model can be generalized to include the full expansion of transverse electric (TE) and magnetic (TM) modes radiated by the dipoles [137, 150]. This method is systematically used in the present work. For rectangular arrays it leads to results identical to the intuitive model (as far as the TE components have a weak contribution, as it is the case for a not too thin metal film [134]).

Concerning the coefficient β, the strong dependence of the directivity on the minor-axis dipole contribution can be found from the equation 4.12. In particular, for a given angle α, the directivity becomes maximum if β vanishes, i.e., if there is no effect of the minor-axis dipole, an assumption usually considered [11]. However, in practice, the directivity rarely reaches 1, so the contribution of β cannot be neglected. Actually, the coefficient β may depend on the aspect ratio of the length and width of the slit, the thickness of the gold film and so forth. Thus, to know the value β in our coupler system is the first thing to do.

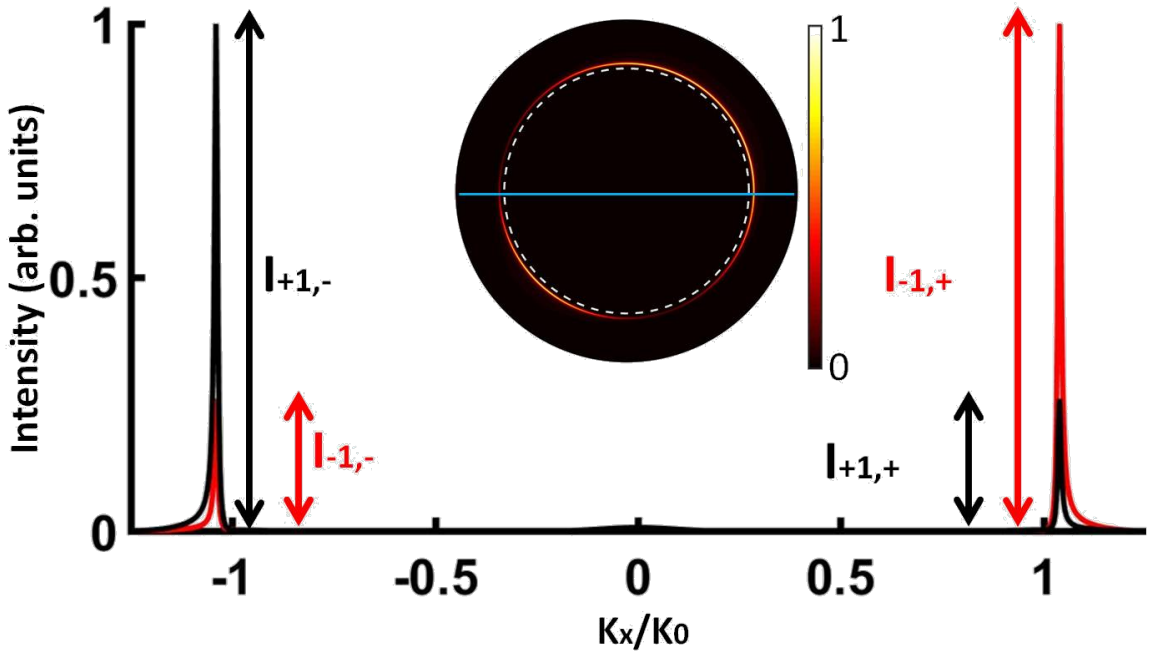

Fig. 4.6 Theoretical intensity cross-section profiles along center line on FP of T-shaped apertures as indicated in the inset (β= 0.5 upon RCP). The black and red lines corresponds to LCP and RCP excitation respectively.

According to the theoretical model, we find that the value $\beta = 0.5$ can better reproduce the experimental results for $V \cong 0.6$. The simulated image of the SPP intensity cross-section profiles with $\beta = 0.5$ is illustrated in Figure 4.6. A plot of $I_{\sigma,\pm}$ on the FP for a single T-shaped aperture is achieved along $k_{x\pm}$ indicated as a blue line (the plot for a Λ-shaped aperture is exactly the same along $k_{x\pm}$). Note that the excitation field is filtered and thus no Fano resonance around the SPP peak positions occurs. In accordance with the experimental results, two side peaks corresponding to the leaky SPP signals are clearly visible and have the same directivity as the experimental results. The black and red curves relates to the resulting SPP signals excited by $\sigma = +1$ and $\sigma = -1$, respectively. In order to confirm the correctness of this theoretical value of β, we introduce a method to measure experimentally β which will be explained in the following section.

4.1.4 Optimization of Λ-shaped apertures

In this section, we firstly present the method for the measurement of β. Secondly, with the determined β, we are going to optimize the apex angle α for seeking the maximum directivity of the coupler system.

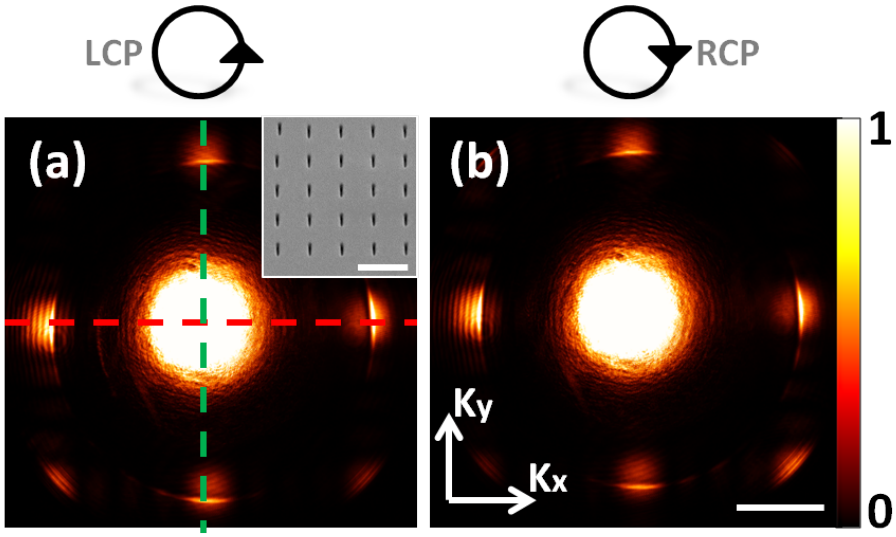

Fig. 4.7 Measurement for the value of β. (a), (b) Fourier plane images corresponding to the LCP and RCP excitation of arrays made of rectangular apertures respectively. The inset displays the SEM image of the whole array. The scale bar values are 1 mm and $0.5k_0$ NA in the inset of (a) and in (b) respectively.

Experimentally, the coefficient β can be determined using a reference array made of vertically oriented ($\alpha = 0°$) rectangular slits with dimensions similar as that of the Λ-shaped aperture's arms (see the inset of Figure 4.7 (a)). The horizontal and vertical periods are fixed

at 600 nm so as to generate propagative SPPs in both Ox and Oy directions. The ratio of the average SPP intensities along the two orthogonal directions in the Fourier plane directly leads to $|\beta|^2$, i.e. the ratio of the two dipolar contributions. Specifically, we have to make sure that the laser beam is well focused in the center of the array. The way is to verify whether the SPP intensities on the left is close to the one on the right (the top and the bottom as well) because there is no reason to generate the directionality from the array of slits. Then, the average SPP intensities along the green and red dashed lines as indicated in Figure 4.7 (a) have been determined. The ratio between the average intensity along the Oy axis and the one along the Ox axis gives directly $|\beta|^2$. Lastly, assuming β is a real positive number, the value $\beta = 0.50 \pm 0.07$ is measured allowing us to derive a theoretical value of α for which the directivity is maximum.

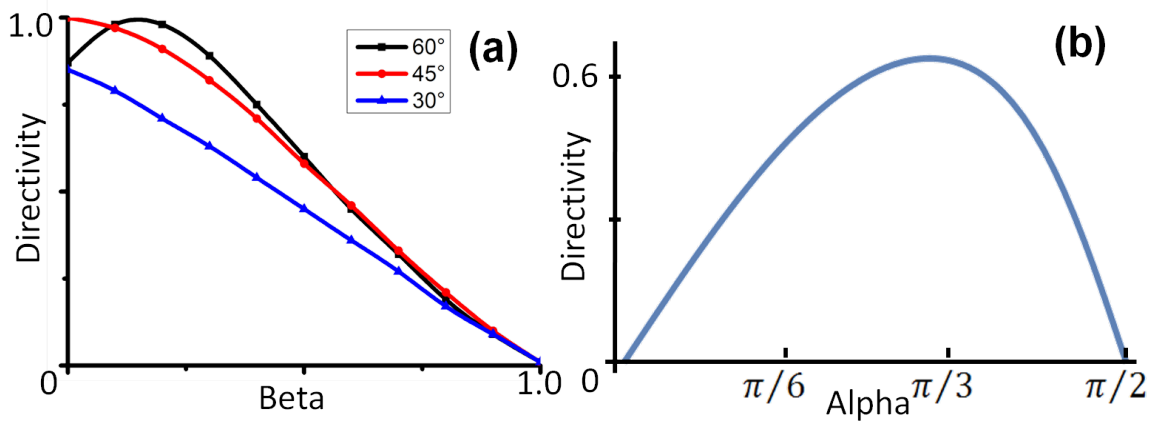

Fig. 4.8 (a) Theoretical plot of the directivity obtained for a Λ-shaped aperture as a function of β. The blue, red and black lines correspond to $\alpha = 30°$, $45°$ and $60°$ respectively. (b) Theoretical plot of the directivity as a function of α at given $\beta = 0.5$.

Now let's try to study whether we could achieve the higher directivity of the Λ-shaped apertures theoretically and experimentally. First of all, let's remind the equation 4.9 based on the multidipolar model. This equation provides the dependence of directivity V with α and β. Thus, we plot this equation of V and β with choosing $\alpha = 30°$, $45°$ and $60°$ which is shown in Figure 4.8 (a). From these three curves, we observe that the apertures with $\alpha = 45°$ and $60°$ can reach the maximum directivity V=1 with a specific β but the aperture with $\alpha = 30°$ can only achieve maximum directivity V=0.9 in the field $0 \leq \beta \leq 1$. Moreover, if $\beta \neq 0$, the maximum directivity is expected to be reached by the aperture with $\alpha > 45°$. If we introduce the value $\beta = 0.5$ measured before, we can further plot the directivity as a function of α shown in Figure 4.8 (b). The directivity of a single Λ-shaped aperture takes its maximum value V=0.68 for $\alpha \approx 60°$. It means that the theoretical model predicts the

maximum directivity can be reached around $\alpha = 60°$. Thus in the following part, we fabricate several Λ-shaped apertures ranging from $\alpha = 30°$ to $75°$ in order to confirm our expectation experimentally.

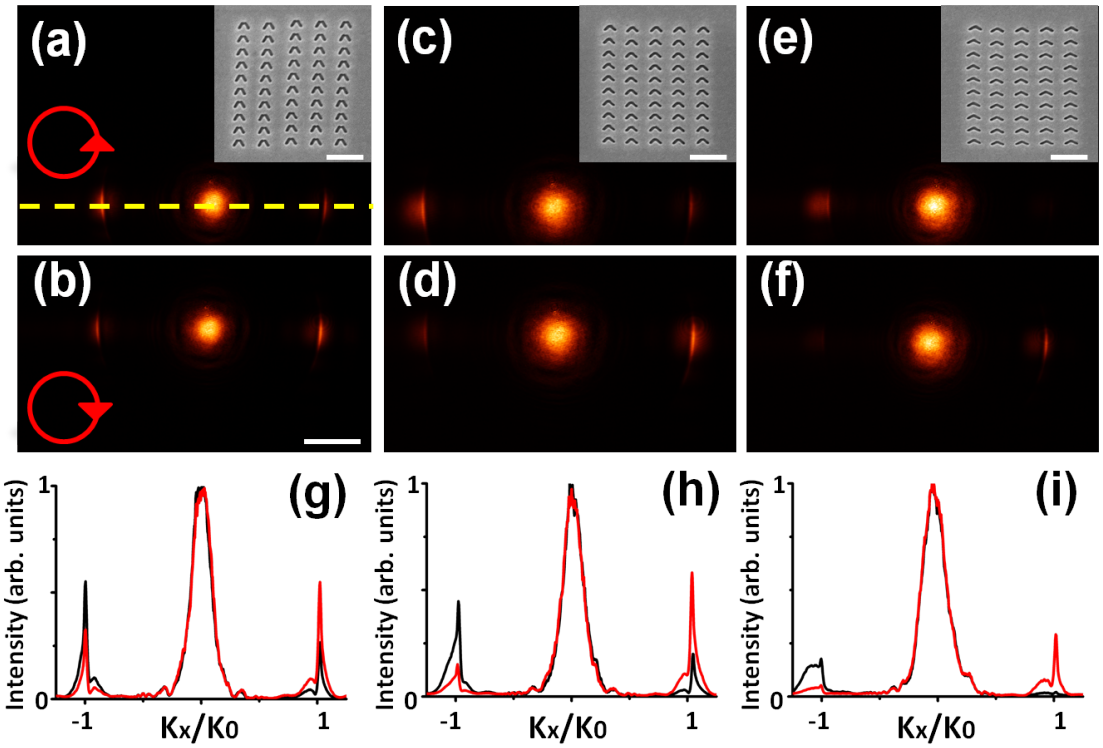

Fig. 4.9 Fourier plane images of Λ-shaped apertures with different apex angles. (a-f) FP images corresponding to the excitation of arrays made of Λ-shaped apertures with apex angles $\alpha = 30°$, $45°$ and $\alpha = 60°$ are shown in (a, b), (c, d) and (e, f) respectively. The insets of (a, c, e) display the SEM images with the scale bar of 1 μm. The (a, c, e) and (b, d, f) are excited upon LCP and RCP beam respectively in the center of arrays. The scale bar for FP images is $0.5k_0$ NA. (g-i) The cross-section profiles in (a, b), (c, d) and (e, f) respectively are measured along the central lines as indicated by the yellow dashed line in (a). The black curve and red curve represent the results upon LCP and RCP excitation respectively.

The 5x10 arrays made of the aformentionned apertures are used in our test. The horizontal and vertical periods of the array are now fixed at 600 nm and 300 nm for SPP resonant excitation in the Ox direction and for preventing SPP propagation in the Oy direction as we mentioned before. The plasmonic arrays are illuminated by a weakly focused laser at 633 nm wavelength and the incident beam is prepared either in RCP or LCP. The FP images of Λ-shaped apertures with apex angles $\alpha = 30°$, $45°$ and $60°$ are displayed in Figure 4.9. By performing cross sections along the center line (see Figure 4.9 (g-i)), we determine the directivities associated with the arrays made of $30°$, $45°$ and $60°$ apertures. We measured

directivities of $V_{30^\circ} = 0.32 \pm 0.11$, $V_{45^\circ} = 0.59 \pm 0.09$ and $V_{60^\circ} = 0.74 \pm 0.07$. All these values are in consistence with the theoretical values in the model. The small discrepancy between theoretical and experimental results may result from the errors for measuring β and SPP peak intensities. Besides, the small inclination of the excitation beam can also lead to the errors. Fortunately, these errors are all in the tolerance of our study. To be conclude, in agreement with the theoretical prediction, we find that the angle $\alpha = 60^\circ$ yields to the maximum value of the directivity. Besides, our experimental result is also consistent with previous numerical simulations [13], which also predict maximum directional coupling for a Λ-shaped structure array with $\alpha = 60^\circ$. Although a finite difference time domain [13] based numerical resolution approach was adopted (see also ref [9] for related studies with lithographed Λ-shaped antennas but with a directionality along the ky axis), we showed that our analytical model based on dipolar approximation is in complete agreement with these results.

4.2 Singular SPP generation in chiral nanostructures

We now extend the above capability and methodology to radial directional coupling by spatially rotating the T-shaped and Λ-shaped apertures following a circle. Radial SPP propagation with an inward or outward direction according to the handedness of the excitation beam is expected from near-field measurements [11]. By means of LRM, we performed detailed characterization of SPP propagation and intensity distribution with polarization analysis in both image and Fourier spaces. The structure is demonstrated, both analytically and experimentally, to induce singular SPP modes and spin-dependent radial directionality as a result of optical spin-orbit interaction. More specifically, unlike the spin angular momentum (SAM), the orbital angular momentum (OAM) of a light beam sketched in Figure 4.10 is independent of the beam's polarization. It arises from helical wave fronts shown in the left column of Figure 4.10. At any fixed radius within the beam, the Poynting vector follows a spiral trajectory around the propagation axis. As we known, the Poynting vector of a plane wave is always along the propagation axis. Therefore, its beam's instantaneous phase cross-section should be in phase all the time. But for the helical waves, the beams' instantaneous phase cross-sections (center column in Figure 4.10) are not in phase any more. The rotation of the phase is associated to the orbital angular-momentum quantum number m (also called topological charge) [151]. The phases with $m \neq 0$ are called singular phases or singularities. The waves which contain singular phases are considered as singular waves. In the right column of Figure 4.10, the intensity profiles of each beam are displayed as well. The wave with $m = 0$ shows a bright spot and the waves with $m \neq 0$ have simple annular (doughnut-

shaped) intensity profiles which are also called optical vortices. The diameters of vortex is dependent on the quantum number m. The presence of OAM leads to not only the new degree of freedom of light beam but also the turning force. Thus, the research about the coupling between SAM and OAM draws a lot of interest in particle trapping, data communication and so forth. In this chapter, we explain one possible solution, which is to introduce SPPs launched by chiral structures, to realize spin-orbit coupling.

4.2.1 Singular SPP and vortex generation

We firstly fabricated a series of plasmonic structures where the elementary T-shaped apertures are spaced 600 nm apart, oriented and arranged into a ring of 2 μm radius which are engraved on the 50 nm gold film (see Figure 4.11 (a), (b)). The broken symmetry of the T-shaped elements imparts chirality to the structure geometry. However, we emphasize that the key feature here is the handedness associated with the whole structure and not the individual chirality of the T-elements (Later, we will show the similar results about the rings of Λ-elements). The plasmonic structure under study is globally right-handed, as displayed in the SEM image in Figure 4.11 (a). Figure 4.11 (b) shows the left-handed plasmonic structure which is the mirror image of Figure 4.11 (a).

A laser beam prepared in the circular polarization state is weakly focused onto the sample and couples into SPPs, which are then imaged on a CCD camera by LRM. The LRM signals are shown in Figure 4.11 (c-f) and are collected in both image and Fourier spaces, thus providing the spatial and angular distributions of the SPP intensity. A beam block is used in order to suppress the incident light directly transmitted through the sample. The results depicted in the row of Figure 4.11 (c, d) and (e, f) are recorded with an exciting beam prepared in the LCP (RCP) state respectively as indicated by the solid white arrow. No polarization analysis (output analysis) are performed here.

One can readily observe in Figure 4.11 (c-f) that SPPs radially propagate toward the center of the system or outward, depending on the incident spin. Upon RCP excitation, inward directional coupling is evident as a well-defined bright spot (Figure 4.11 (e)), whereas a dark central spot (Figure 4.11 (c)) corresponding to outward propagation is observed when the system is illuminated with the orthogonal LCP state. As intuitively anticipated, mirror symmetry property is conserved in the spin-dependent radial coupling. In case of the right-handed structure (Figure 4.11 (a)), RCP illumination leads to inward directional coupling whereas for the left-handed structure (Figure 4.11 (b)) it is obtained under LCP excitation. Inversely, we have outward directional coupling when the right-handed strucure is excited with LCP illumination but with RCP excitation for the left-handed structure.

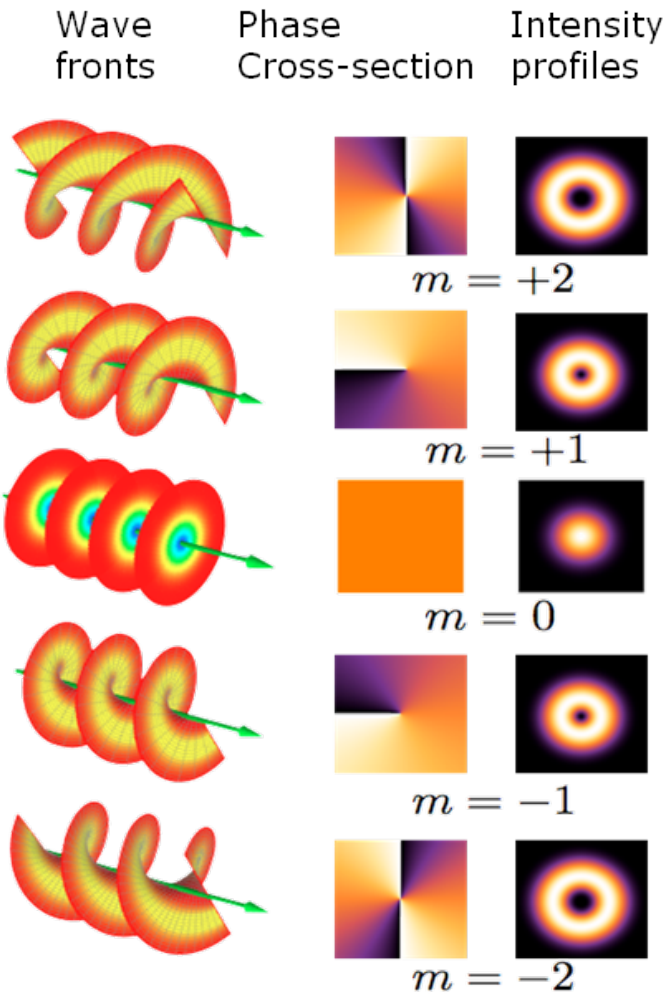

Fig. 4.10 Orbital angular momentum of a light beam, unlike spin angular momentum, is independent of the beam's polarization. It arises from helical wave fronts (left column), in which green arrows indicate the direction of the wave propagation. Rows are labeled by m, the orbital angular-momentum quantum number (topological charge). $L_z = m\hbar$ is the beam's orbital angular momentum along the propagation direction per photon. For each m, the center column is a schematic snapshot of the beam's instantaneous phase cross-section. An instant later, the phase advance is indistinguishable from a small rotation of the beam. By themselves, beams with helical wave fronts have simple annular intensity profiles (right column) [151].

From these four LRM images, the chirality of our system is firstly proven to result in a spin-sensitive radial directional coupling, as anticipated by our previous study. Our chiral plasmonic device demonstrates spin-based switching capability with a tightly focused spot that can be switched on and off by an appropriate input spin-state. Furthermore, working with a thin metal film allows us to decouple the singular SPP field into the far-field. An additional

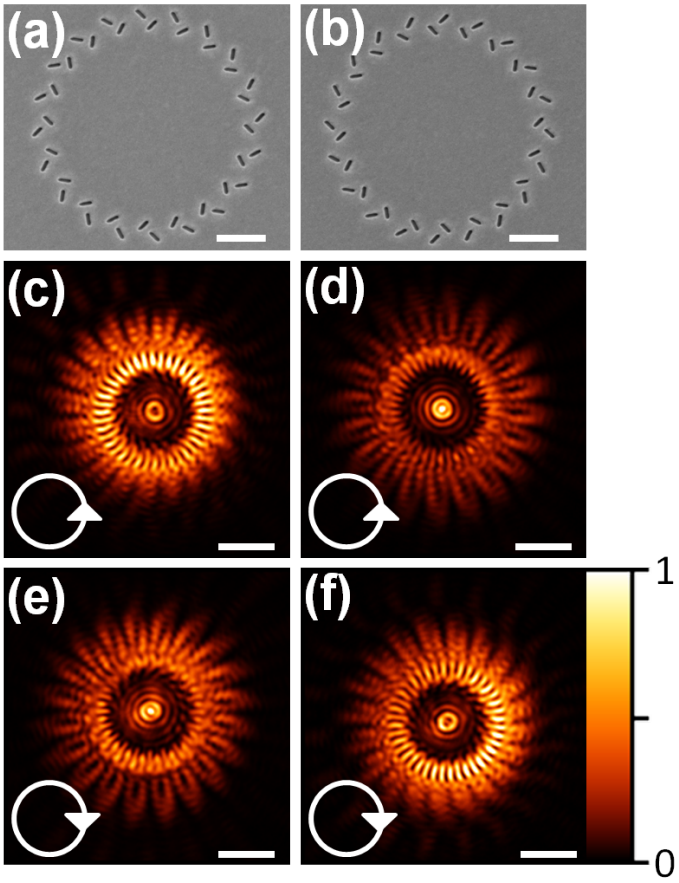

Fig. 4.11 (a), (b) SEM images of right-handed and left-handed plasmonic structures. The scale bar values are both 1 μm. (c-f) LRM images on the DP obtained for the structures in (a) (first column) and in (b) (second column) upon polarized excitation as indicated by the white solid arrows. The scale bars are all 2 μm.

observation we address here is the remarkable annular intensity patterns (donuts-shape) surrounding the central spots. Ring profiles are typical of vortex fields. Previous works on bull's eyes and circular apertures reported that structures with rotational symmetry create Bessel beams according to spin-states [152, 153].

To further probe the recorded SPP intensity distribution, we perform polarization analysis in both direct and Fourier spaces for the right-handed structure shown in Figure 4.11 (a) as an example. The images were recorded in circular polarization basis (output analysis) as indicated by the dashed arrows in Figure 4.12. Upon RCP and LCP projection, Figure 4.12 (c) and (d) display intensity maxima near the center when the signal is recorded with the same handedness as the input state, whereas intensity minima with annular pattern (Figure 4.12 (e), (f)) are obtained for the orthogonal output state. Furthermore, spin-orbit coupling

induced by the handedness of the structure results in brighter intensity in the case of RCP excitation. The spin-driven SPP intensity and the pattern that are associated with SPP vortices will be discussed in detail later. Noteworthy, inspection of FP images (Figure 4.12 (g), (h)) shows the two main contributions to the observed LRM signals: the radially excited SPPs and the diffraction emission. The discretized SPP pattern demonstrates that SPPs are launched by T-elementary apertures. For a given k_{spp} direction in the reciprocal space, the images corresponding to RCP and LCP output states exhibit the same SPP intensities in accordance with the conversion of energy between SPP propagating toward and outward from the center of the structure. The asymmetric SPP intensity may be ascribed to a weak misalignment of the setup or to a slight ellipticity, hence providing sensitive information on experimental errors. In order to understand the physics involved in the directional propagation of SPPs, we now propose an analytical model based on a two-dipole representation of the nanostructures. Before introducing the model, we firstly display a group of images to clarify the mirror symmetric confusion in the next section.

4.2.2 Mirror symmetry and handedness of chiral structures

The mirror symmetric issue in the rings of T-shaped apertures are more complicated in the arrays of Λ-shaped apertures because there are four kinds of plasmonic structures instead of two and it is not evident to predict them without experiment. Thus, we list all these four cases sorted from the experimental results with polarization analysis in the Figure 4.13. The right-handed plasmonic structure in column 1 and its mirror symmetric structure along the Oy axis in column 2 (left-handed structure) have been displayed and discussed in the previous section. The plasmonic structure in column 3 has the reversed handedness to the structure in column 1. Therefore, the structure in column 3 is defined as left-handed structure as the one in column 2 and its mirror symmetric structure along the Oy axis is thus called right-handed structure as the one in column 1. Without carrying out experiment, we can imagine the structures in column 1 and column 4 should have exactly the same results with the same polarized excitation whereas the LRM images in column 2 and column 3 should be the same.

The experimental images confirm that our reasoning is correct and allow us to interpret any chiral ring-like structure in the following study. Furthermore, the DP images with the output polarization analysis are also shown in Figure 4.13. Interestingly, we notice if the output analysis has the same polarization as the incident excitation, a small relatively bright spot namely SPP singularity appears in the center of the structures. The intensity of the singularity is associated to the handedness of the structure. On the contrary, if the output analysis has the opposite polarization with respect to the excitation light, only the donuts-shaped pattern namely SPP vortex left near the center of the structure for all the

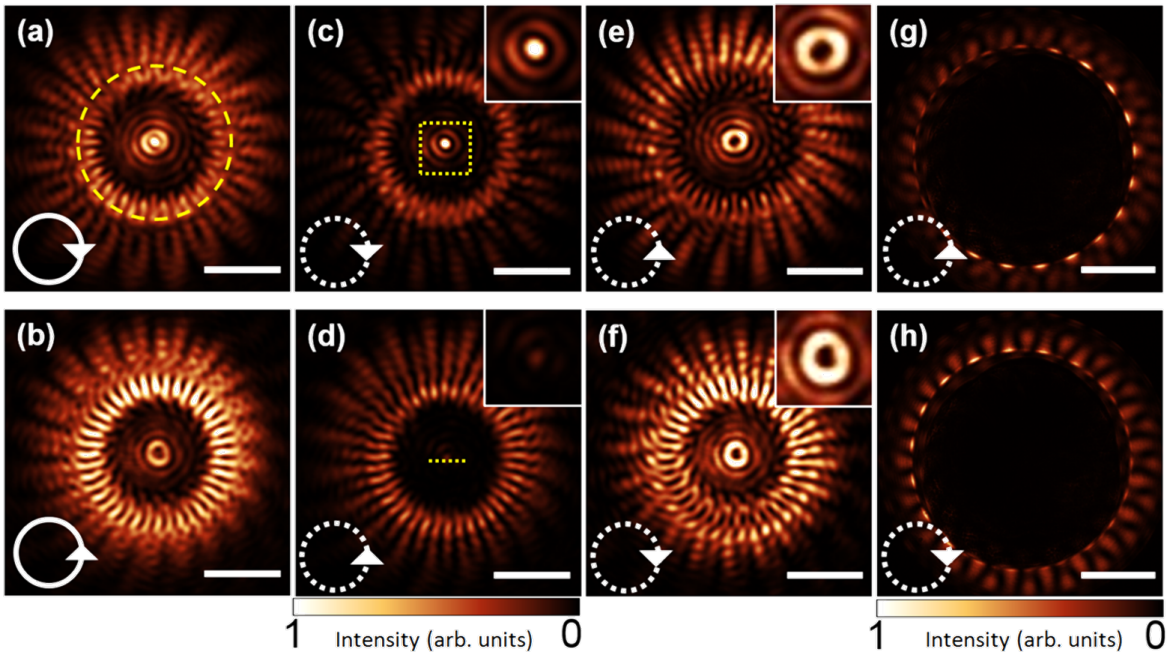

Fig. 4.12 Experimental LRM results for the right-handed plasmonic structure depicted in Figure 4.11 (a). It is illuminated either with RCP (first row) or LCP (second row) polarization, as indicated by the white solid arrows in (a) and (b). The yellow dashed circle in (a) indicates the position of the structure. (a-f) Transmitted LRM signals measured on the DP (scale bar value: 2 μm) and (g, h) on the FP (scale bar value $0.5k_0$ NA). (a, b) Signal recorded without and (c-h) with polarization analysis in the circular basis as indicated by the dotted arrows. Zoom-in on SPP focusing spot and SPP vortex are shown in the insets. Exposure time is 2 s (a-d) and 4 s (e, f). A beam block in the Fourier plane is used to remove the directly transmitted light from the incident beam.

cases. As a conclusion from the experimental results, the handedness structure upon the same handedness of the circular polarized excitation can generate the stronger intensity of the SPP singularity. The opposite case lead to the stronger SPP vortex field. Secondly, with the additional output filter, we can achieve more pure SPP singular and vortex fields based on the discipline which is pointed out before for the polarization analysis.

4.2.3 Multidipolar model for singular SPP generation

After confirming the issue about symmetry and handedness of the ring-like chiral structures from the experimental results, we are trying to find a physical insights into the observed LRM signals. We analytically derive the solutions describing the SPP intensity distribution near the origin, generated by our plasmonic structure. In the present analytical model, the system is described by the aforementioned pair of dipoles and the structure diameter is

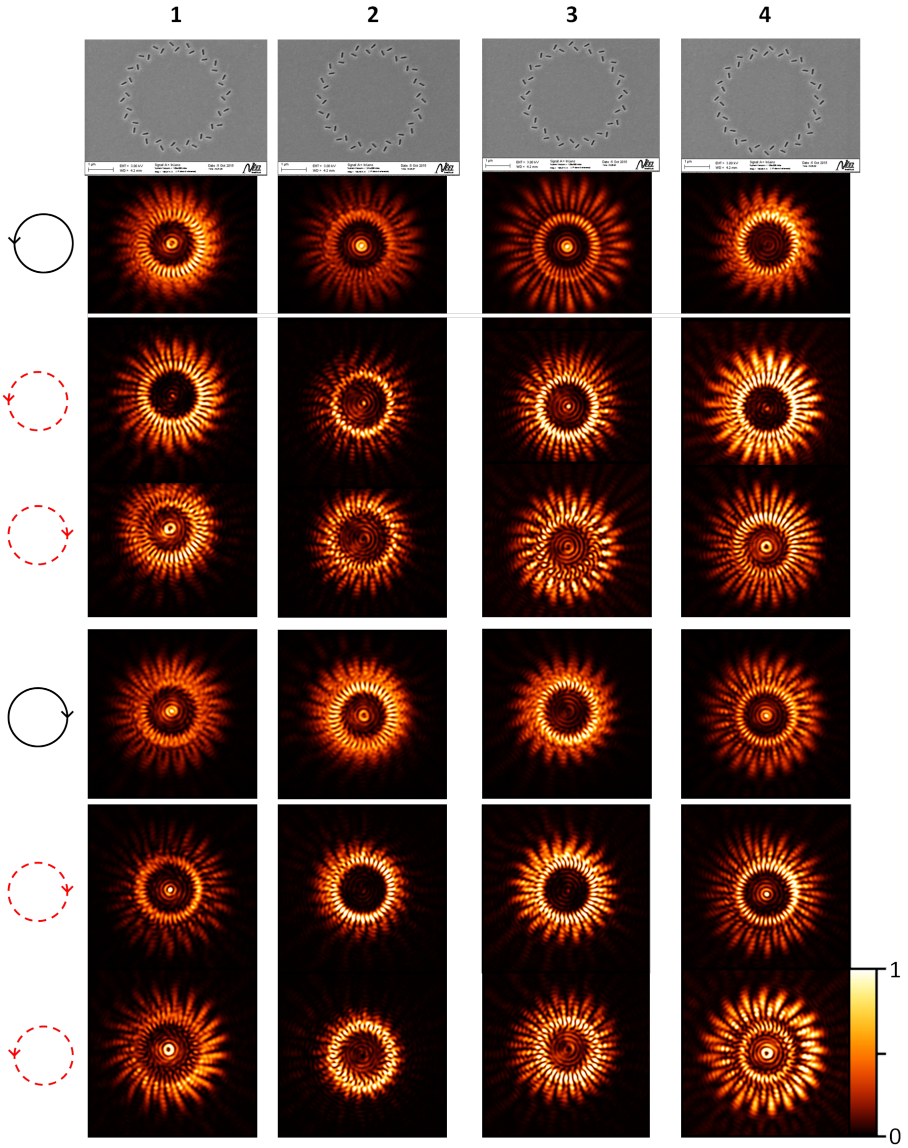

Fig. 4.13 Experimental results of four chiral T-shaped plasmonic structures. Each column with number 1-4 shows the DP images with corresponding structure (SEM images in the first row) under LCP or RCP excitation. The second and fifth rows are the DP images without output analysis upon the LCP and RCP excitation respectively. The black solid arrows indicate the incident polarization states and the red dashed arrows represent the polarization states using for output analysis.

assumed to be large enough with respect to λ_{spp} and separation D. Now, let us first come back to a plasmonic structure comprising two rectangular slits refered here as *A* and *B* and oriented to form a T-shaped aperture, which is schematized in Fig.4.14 (a). Each aperture

was characterized by a short and long axis. The normal vectors to the long axis $\widehat{n}_i$ (i=A, B) of each apertures are given by: $\widehat{n}_A = \dfrac{\widehat{U}_x + \widehat{U}_y}{\sqrt{2}}$ and $\widehat{n}_B = \dfrac{-\widehat{U}_x + \widehat{U}_y}{\sqrt{2}}$.

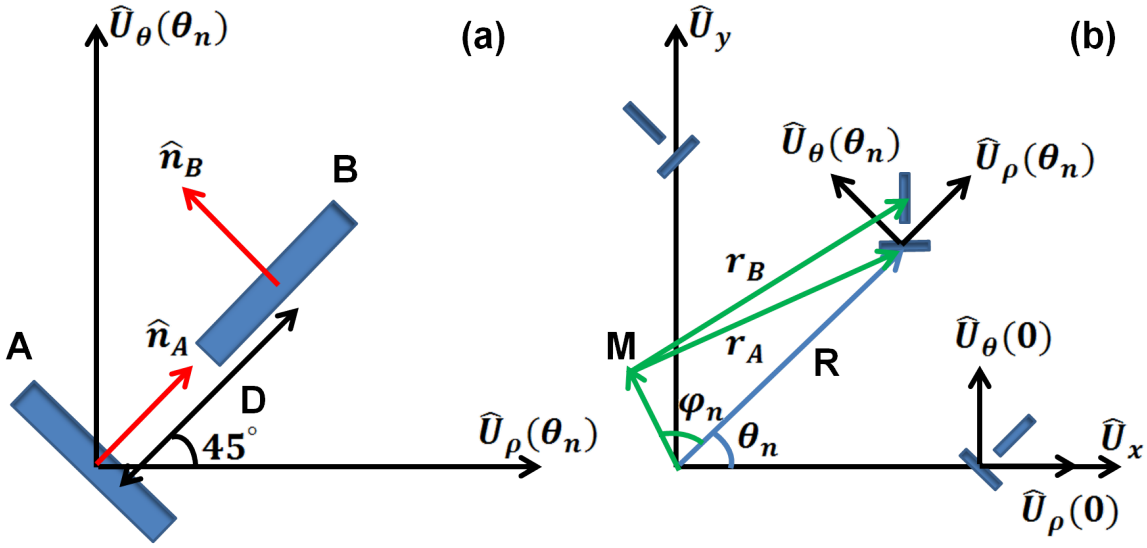

Fig. 4.14 Schematic of the analytical model for chiral plasmonic structures. (a) Recap of a single T-shaped nanoaperture. (b) T-shaped apertures arranged in a circle. We don't show all the circle with twenty T-shaped apertures. Only one quarter of the circle with three T-shaped apertures is shown here as an example.

For the sake of simplicity, we consider a single dipole description for describing the SPPs launched by a rectangular slit. Given only the component of the incident light that is polarized perpendicularly to scattering elements can efficiently be coupled into SPPs, we here consider SPPs to be mainly induced by SPP dipoles $\overrightarrow{\mu}_i$ along $\widehat{n}_i$.

Each T-shape aperture is then duplicated and arranged in a ring configuration as displayed in Fig.4.14 (b). The coordinate system associated to each elementary T aperture n comprising the plasmonic structure is referred as $(0, \widehat{U}_\rho(\theta_n), \widehat{U}_\theta(\theta_n))$. The plasmonic structure is excited by an incident electric field prepared in a circular polarization state σ. In polar coordinates $(0, \widehat{U}_\rho(\theta_n), \widehat{U}_\theta(\theta_n))$, it writes:

$$\mathbf{E}_\sigma = \frac{\widehat{U}_x + i\sigma\widehat{U}_y}{\sqrt{2}} = \frac{e^{i\sigma\theta_n}}{\sqrt{2}}(\widehat{U}_\rho(\theta_n) + i\sigma\widehat{U}_\theta(\theta_n)), \tag{4.13}$$

with $\sigma = +1$ refering to a incident beam prepared in LCP and $\sigma = -1$ in RCP. Therefore, the SPP dipole moment corresponding to each slit is given by: $\overrightarrow{\mu}_i(\theta_n) = \eta(\mathbf{E}_\sigma.\widehat{n}_i(\theta_n)).\widehat{n}_i(\theta_n)$. Let us now derive the total SPP field near the center of the structure in the direct plane. It can be expressed as:

$$\overrightarrow{E_{spp}}(M) \propto \sum_{n=0,1...N} \frac{e^{i\mathbf{k_{spp}}.\widehat{r}_A}}{\sqrt{r_A}}(\overrightarrow{\mu}_A.\widehat{r}_A)\widehat{r}_A + \frac{e^{i\mathbf{k_{spp}}.\widehat{r}_B}}{\sqrt{r_B}}(\overrightarrow{\mu}_B.\widehat{r}_B)\widehat{r}_B \tag{4.14}$$

with N the total number of T-shape apertures comprising the ring. As we are interested in the SPP intensity distribution near the origin of the system, it is assumed the distance between the observation point M and each T-shaped aperture to be much greater than the exciting wavelength, and the distance between the slits namely $R \gg D, \lambda$ as indicated in Figure 4.14 (b). Hence under this approximation $\widehat{r}_A \approx \widehat{r}_B \approx \widehat{U}_\rho(\theta_n)$ and projected on the $\mathbf{E}_\sigma$ basis $(0, \mathbf{E_{-1}}, \mathbf{E_{+1}})$, we find the total SPP field at a point M is given by:

$$\begin{aligned}\overrightarrow{E_{spp}}(M) \propto C_\sigma \{ & e^{i(\sigma+1)\theta_M} \sum_{n=0,1...N} e^{ik_{spp}r_M cos(\varphi_M)} e^{i(\sigma+1)\varphi_M} \overrightarrow{E}_{-1} \\ & + e^{i(\sigma-1)\theta_M} \sum_{n=0,1...N} e^{ik_{spp}r_M cos(\varphi_M)} e^{i(\sigma-1)\varphi_M} \overrightarrow{E}_{+1} \},\end{aligned} \tag{4.15}$$

with

$$C_\sigma = n_A^x(0) + i\sigma n_A^y(0)).n_A^x(0) + n_B^x(0) + i\sigma n_B^y(0)).n_B^x(0) e^{ik_{spp}D/\sqrt{2}}. \tag{4.16}$$

Assuming $\theta_{n+1} - \theta_n \ll 1$, we can transform the sum into an integral:

$$\begin{aligned}\overrightarrow{E_{spp}}(M) \propto C_\sigma \{ & e^{i(\sigma+1)\theta_M} (-1)^{\sigma+1} J_{\sigma+1}(k_{spp}r_M) \overrightarrow{E}_{-1} \\ & + e^{i(\sigma-1)\theta_M} (-1)^{\sigma-1} J_{\sigma+1}(k_{spp}r_M) \overrightarrow{E}_{+1} \},\end{aligned} \tag{4.17}$$

with $J_l(x)$ the l^{th} order Bessel function. Finally, we show that the singular SPP intensity near the origin upon an illumination with the spin state σ is a combination of Bessel's functions [149] such as $I_\sigma^{tot} = I_{\sigma,L} + I_{\sigma,R}$ with:

$$\begin{aligned} I_{\sigma,L} &\propto \mid C_\sigma \mid^2 J_{\sigma-1}^2(k_{spp}, \rho) \\ I_{\sigma,R} &\propto \mid C_\sigma \mid^2 J_{\sigma+1}^2(k_{spp}, \rho) \end{aligned} \tag{4.18}$$

.

$I_{\sigma,j}$ denotes the resultant SPP intensity launched by LCP/RCP polarization states ($\sigma = +1/-1$) and analyzed in RCP/LCP states ($j = L/R$). ρ represents the distance between the T-shaped elements and the circular-structure center, and $J_{\sigma\pm1}$ stands for the $(\sigma \pm 1)^{th}$ order Bessel function [154, 155]. In the case of $\sigma = \pm 1$, J_0^2 and $J_{\pm2}^2$ represent that the output polarization analysis is similar and opposite to the incident polarization states respectively.

C_σ ($\sigma = \pm 1$) refers to the SPP coupling efficiency of the single T-shaped element upon RCP (LCP) polarization input state given by:

$$\begin{aligned} C_\sigma &= 1 - \sigma + (1 - \sigma)i \\ &+ \beta[1 + \sigma - (1 + \sigma)i]. \end{aligned} \tag{4.19}$$

In accordance with our LRM measurements, our model successfully predicts the spin-orbit coupling induced by our chiral structures. It demonstrates the conversion of the incident spin into singular SPP fields, which can be described by zeroth and second-order Bessel functions, respectively. Similarly to a ring aperture under circularly polarized field, the structure can excite SPP vortices of topological charges of 0 and 2. Besides, it is associated with a selection rule leading to SPP intensity contrast between RCP and LCP excitation. This selection rule comprises the spin-sensitive coupling coefficients C_{-1} and C_{+1} with $C_{-1} > C_{+1}$. In agreement with our experimental results, our calculations well reproduce the spin-sensitive SPP coupling efficiency: upon RCP illumination, high intensity SPP fields are measured (Figure 4.12 (c), (e)), whereas lower intensity SPP fields are collected upon LCP illumination (Figure 4.12 (d), (f)). Note that, the equation 4.19 is only valid for the right-handed structure which is chosen as an example in the analytical model. Thus, for the left-handed structure, the SPP coupling efficiency is modified as:

$$\begin{aligned} C_\sigma &= 1 + \sigma + (1 + \sigma)i \\ &+ \beta[1 - \sigma - (1 - \sigma)i]. \end{aligned} \tag{4.20}$$

Moreover, the field distributions upon RCP and LCP excitation are spatially separated near the origin, which is reminiscent of a spin Hall effect. Generally applied to electrons and originating from the spin-orbit coupling, the spin Hall effect manifests itself as a dependence of the electron's spatial trajectory on its spin. Here, we observe a spin-sensitive deviation upon interaction with the chiral plasmonic system. We can envision the implementation of the latter as a means to generate singular SPP fields with RCP or LCP states.

4.2.4 Simulation results and quantitative analysis

The above simplistic theoretical model provided us with a physical comprehension of the mechanism at play and qualitatively described the observed SPP intensity patterns with Bessel functions. However, the contribution of diffraction and the effects of the imaging systems on the LRM images were ignored. In order to carry out a quantitative analysis, we take these effects into consideration and perform simulations with the radiated fields described by TM and TE fields [137]. We also account for the contribution of β previously determined

experimentally. The simulation results are depicted in Figure 5.5. We found the simulated results to be in excellent agreement with the experimental results shown in Figure 4.12. The simulation clearly exhibits the fact that the right-handed plasmonic structure radially focuses the incident RCP into a central peak and LCP excitation leads to a donuts-shaped pattern.

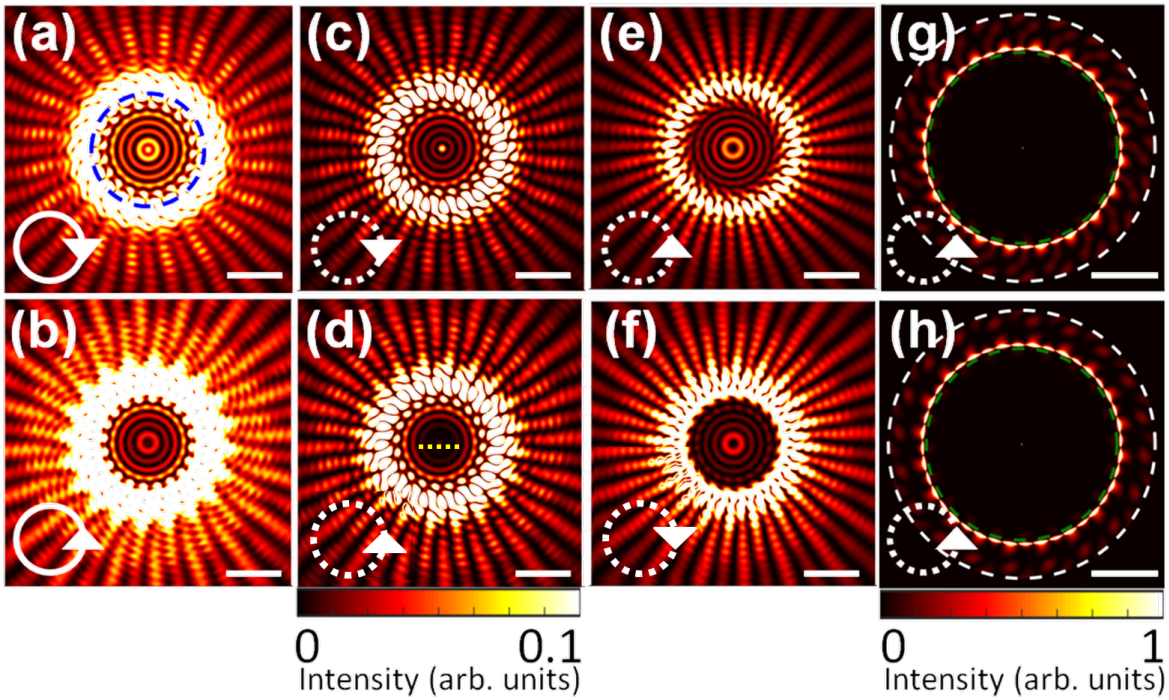

Fig. 4.15 Simulated LRM results for the right-handed plasmonic structure. It is illuminated either with RCP (first row) or LCP (second row), as indicated by the white solid arrows. The blue dashed circle in (a) indicates the position of the structure (respectively beam blocker). (a-f) Transmitted LRM simulated signals provided in the image plane (scale bar value: 2 μm) and (g, h) in the Fourier space (scale bar value $0.5k_0$ NA) in which the white dashed circle represents k_0 NA. (a, b) Signal recorded without and (c-h) with polarization analysis in the circular basis as indicated by the dotted arrows. Exposure time is 2 s (a-d) and 4 s (e, f). Beam block in the FP is used to block transmitted light from the incident beam.

To quantify the value of the SPP switching capability, we perform cross-sections along the center line in Figure 4.12 (c-f) as indicated by the yellow dashed line in Figure 4.12 (d). The intensity cross-sections are displayed in Figure 4.16 (a), (b). LRM images allow direct and quantitative determination of the plasmonic device features such as focusing efficiency and extinction ratio. We found a subwavelength focused spot of 247 nm full width at half maximum in the case of input and output in the RCP state. We also define the extinction ratio (ER) which is used to quantify the SPP singular generation induced by the right-handed plasmonic structure as $ER = |C_{-1}|^2/|C_{+1}|^2$. The value of $ER = 7.45$ can be experimentally achieved by measuring the peak value of red curve in Figure 4.16 (a) and of blue curve in

4.16 (b). Thus, our characterization method allows quantitative measurements and can be implemented for plasmonic device performance optimization.

A quantitative comparison is achieved by obtaining cross-sections along the center line in Figure 4.15 (c-f) as indicated in Figure 4.15 (d) similarly to Figure 4.12 (d). The intensity cross-sections are displayed in Figure 4.16 (c), (d). We find that experimental results well support the theoretical model, which predicts an extinction ratio of 6.50 and a focused spot size of 182 nm. This close inspection also reveals some differences between the measured and simulated SPP intensity profiles. Experimental uncertainties such as setup misalignment and polarizer imperfections are assumed to be at the origin of the observed discrepancies. Additionally, interactions between dipoles have been neglected in our theoretical model and hence can also contribute to those differences. These effects require further investigation such as numerical simulations accounting for interdipole interactions.

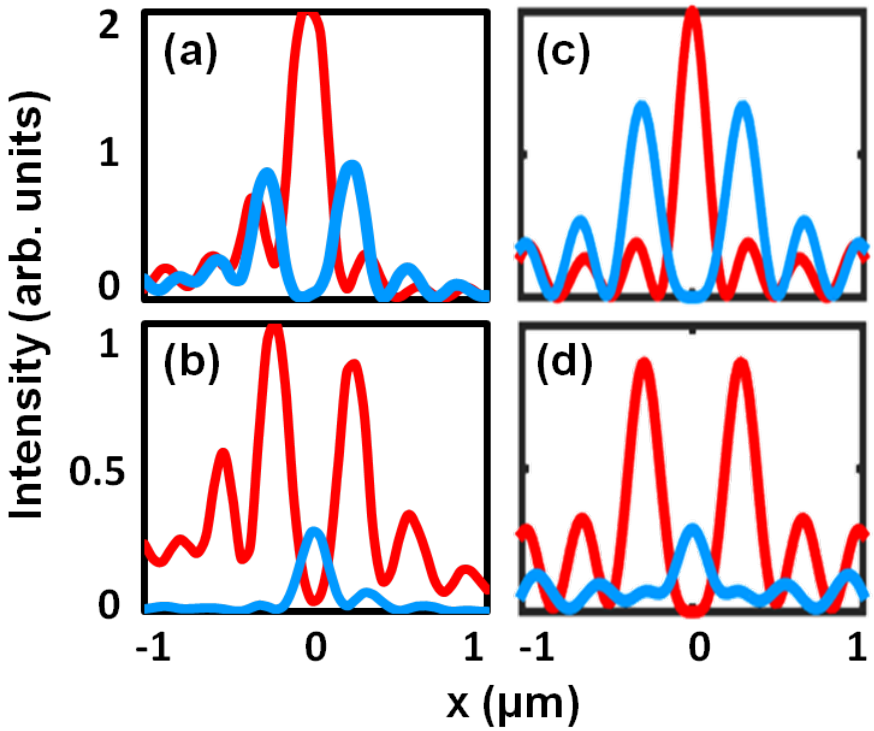

Fig. 4.16 Intensity cross-section along the center line as indicated by the yellow dotted lines in Figure 4.15 (d). (a, b) Experimental and (c, d) simulated results obtained with input states prepared in RCP (a, c) and LCP (b, d). The blue curve corresponds to output states prepared in LCP and the red curve to RCP.

4.2.5 Optimization of the SPP singularity

The rotational symmetry of the structure is broken due to the chirality ascribed to the T-shaped elements. We note however that similar results can be obtained with Λ-shaped apertures forming a circle and inducing therefore a global twist to the system. This emphasizes again the role played by the phase in our experiments due to the previously discussed equivalence between Λ-shaped and T-shaped apertures. Thus, we employ here the ring made of achiral Λ-shaped apertures instead to reach the maximum efficiency by optimizing the apex angle α (see the inset in Figure 4.17 (a)). We emphasize that the structure is globally chiral since the circle is oriented by the direction of the Λ-shaped apertures.

The LRM images of a plasmonic structure formed by 20 rotating Λ-shaped apertures with the apex angle $\alpha = 60^\circ$ are displayed in Figure 4.17 (a-f). In Figure 4.17 (a), (b), a spin-sensitive response of SPPs clearly appears upon RCP and LCP excitation as a result of spin-orbit coupling. Like the handedness of T-shaped apertures, a bright (dark) central spot is observed when the signal features the same (opposite) handedness as the input field (Figure 4.17 (c), (d)). We emphasize that the SPP focusing and vortices are more intense under RCP than LCP excitation because the right-handed structure of Λ-shaped apertures inwardly generates SPP under RCP excitation. These recorded intensity distributions can be understood by applying the above analytical study to a ring of Λ-shaped apertures.

Theoretically, with the practical value of β=0.5, the apex angle that optimizes ER is predicted for $\alpha = 60^\circ$ with $ER_{60^\circ} = 13.93$. In order to experimentally determine ER, we derive the ratio between the central peak values from cross-sections intensities as depicted in Figure 4.18 (a), (b). In consistence with the theory, we find $ER_{60^\circ} = 11.02 \pm 3.22$ which is higher than the extinction ratio of the ring of T-shaped apertures previously determined $ER = 7.45$. It demonstrates that the circular ring design of achiral Λ-shaped apertures with the optimal apex angle has the same effect on singular SPP generation and even better efficiency than the structure of chiral T-shaped apertures. Furthermore, we verify that this design corresponds to the optimal design by comparing it to structures fabricated with the apex angle $\alpha = 30^\circ$ and 45°. The later are shown to feature $ER_{30^\circ} = 3.90 \pm 2.17$ and $ER_{45^\circ} = 6.45 \pm 3.01$, which is in agreement with the expected theoretical values $ER_{30^\circ} = 2.18$ and $ER_{45^\circ} = 4.00$ as well as with the directional coupling efficiency of the arrays. As predicted, the SPP vortices present two side lobes with a minimum intensity or singularity at the center as indicated by the blue curves in Figure 4.18. Noteworthy, our model does not take into account the coupling between adjacent apertures and the SPP field around the center (far away from the origin), which could explain the observed discrepancies between the experimental and theoretical data.

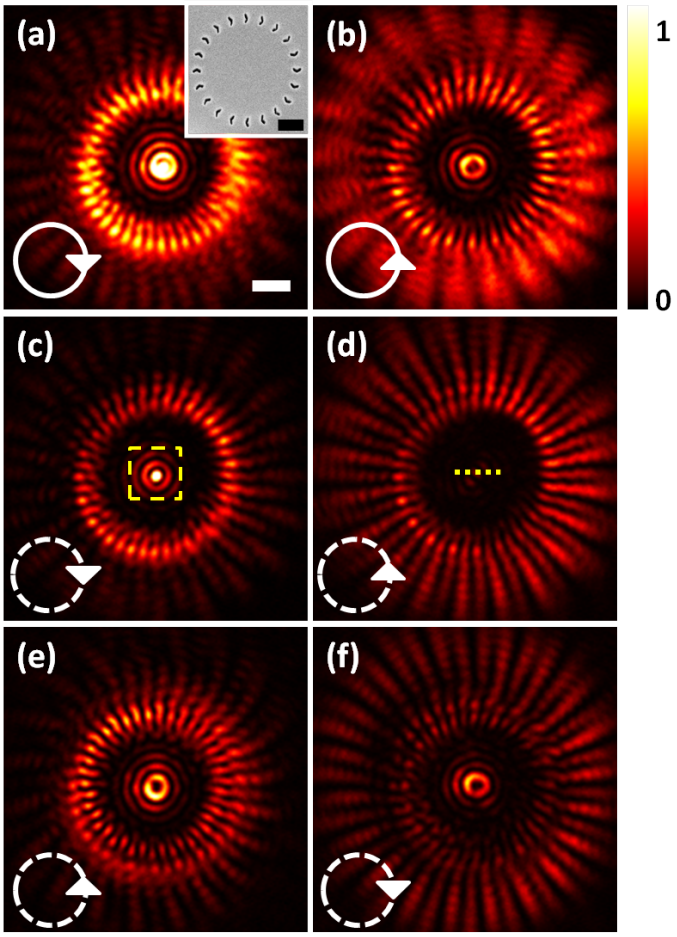

Fig. 4.17 Direct plane images for the circle of Λ-shaped apertures with $\alpha = 60°$. A beam block in the Fourier plane is used to remove the directly transmitted light from the incident beam. (a, b) Signal recorded under the polarization excitation indicated by the solid arrows. (c, e) Signal recorded under RCP with polarization analysis in the circular basis as indicated by the dotted arrows. (d, f) Signal recorded under LCP with polarization analysis. The inset in (a) is the SEM image for the circle of Λ-shaped apertures. The scale bars in (a) are both 1 μm.

In summary, the optimal apex angle of the achiral Λ-shaped structure was successfully determined for both directional coupling and singular SPP generation in the far field. Our method based on LRM detection allows quantitative analysis and was proven to be a sophisticated characterization technique for mapping SPP vortex field. It provides several new possibilities for polarization controlled SPP subwavelength focusing. The presented multidipolar model was demonstrated to be a suitable tool for predicting the extinction ratio of the SPP singularity. In particular, it highlights the the short axis aperture contribution has to be taken into account in the design of directional plasmonic structure. All these findings offer a promising way for device development in the field of nanophotonics such as optical

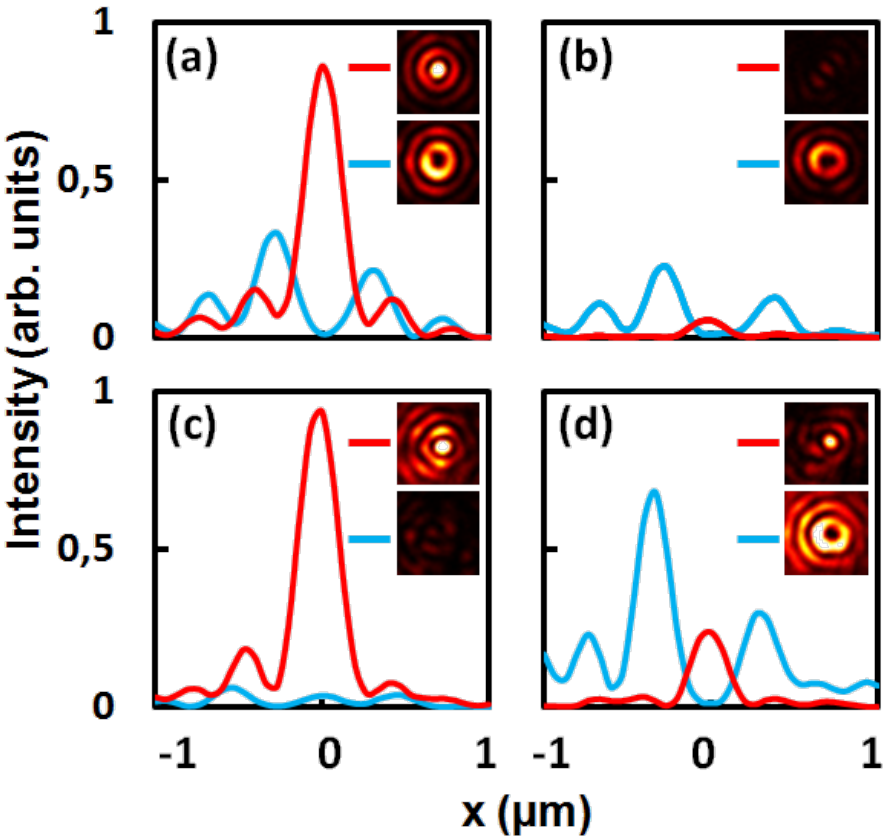

Fig. 4.18 Intensity cross-section along center-line as indicated by the yellow dashed line in Figure 4.17 (d). (a, b) Cross-section polarized analysis for $\alpha = 60^\circ$ and (c, d) cross-section polarised analysis for $\alpha = 30^\circ$. Zoom on SP focusing spot and SP vortex are shown in insets as indicated by the yellow dotted box in Figure 4.17 (c). (a, c) are the results under RCP input state and (b, d) are under LCP input state. The red curves correspond to the same output state (polarizer) with the input state. The blue curves correspond to the reversed output state (polarizer) with the input state.

tweezers,[88, 156] particle trapping [157, 89] etc. In the next chapter, we will apply the Λ-shaped structures to study whether they can still work for the case of guided waves. The second-part results about the spin-orbit coupling of light into the waveguide and its reciprocal effect are reported.

Chapter 5

System of emitters, nanostructures and waveguides

Abstract: In this chapter, we explore the directional coupling of light into the waveguide because waveguides are the important ingredients for integrated optics. In the first section, coupler and decoupler gratings for converting the free-space light to the confined waves are presented. Then, a triple-coupler system is proven to work as a beam block for waveguides so as to realize the directional control of the coupled light. In the second section, the Λ-shaped antennas are fabricated on the waveguide in order to achieve the optical spin-orbit coupling of guided waves. The dark field and fluorescence images provide us strong evidences for the directional coupling effect. In the last section, the reciprocal effect of spin-orbit coupling is proposed and investigated both experimentally and theoretically. Finally, this reverse effect is realized by filtering the specific region on the Fourier plane.

Contents

5.1 Couplers and decouplers for dielectric waveguides

In the previous chapter, the directional coupling of SPPs has been demonstrated. From now on, the directional coupling of light into the waveguide will be investigated. Dielectric waveguides is always of interest because it is an important ingredient for integrated optics. In a huge number of research on optical waveguides recently, periodic structures or gratings have been considered into large amounts of devices [158, 159]. The grating can perform three functions depending on the variety of requirements such as phase matching, wave coupling and wavelength dispersion etc. [160–163]. In this section, we will discuss a kind of simple grating deposited on a waveguide which is served as input or output couplers (also called decouplers). The design details of couplers are firstly illustrated and then a simple way for the unidirectional coupling of light into the waveguide is realized by a group of couplers. This effect is easier to observe with the help of nanocrystals. The fluorescence of nanocrystals provides us an efficient method for visualizing the propagation of the guided light. Lastly, we conclude that the couplers work as a very efficient beam block for the control of propagation direction in the waveguide. It means that neither reflection nor transmission of confined waves can be presented and almost all the guided light radiates in the free space from the couplers.

5.1.1 Design of coupler gratings

The basic coupler is generally made of a periodic structure with a certain number of rectangular indentations on the waveguide [164]. The gold strips serve as these periodic indentations in our case and are fabricated by the method of e-beam lithography. If waves in the free-space need to couple into the waveguide or the confined waves in a waveguide need to convert into the free-space waves, the period (Λ) for in- or out-coupling has to respect the conservation of momentum according to the equation below:

$$\frac{2\pi}{\lambda_0}\sin(\theta)+\frac{2\pi}{\Lambda}=\frac{2\pi}{\lambda_0}N_{eff}, \tag{5.1}$$

where the coupling critical angle θ depends on the wavelengths. This angle is defined as the minimum angle with respect to the normal excitation on the grating for light coupling. The N_eff represents the effective index of waveguides which has been introduced in Chapter 2. For the case of out-coupling, the coupling angle θ can be expected at 0° (assuming the confined waves are normally decoupled into the free space). Thus, the above equation can be simplified as [165]:

$$\Lambda = \lambda_0 / N_{eff}. \tag{5.2}$$

In our case, the working wavelength (λ_0) is chosen at 633 nm and the effective index of the 240 nm TiO_2 waveguide (N_{eff}) was characterized at 1.75 (taken for the TM mode). Thus, the period of the decoupler grating is deduced at 362 nm (360 nm is used in the design of the couplers). The duty cycle is fixed at $1/2$, namely the width of gold strips is equal to one half of the period which is 180 nm. The length and the height of each stripe are respectively fabricated at 4 μm and 50 nm as indicated in Figure 5.1 (a). Four stripes are used for the decoupler. The same grating can be also used as the coupler in the following experiment.

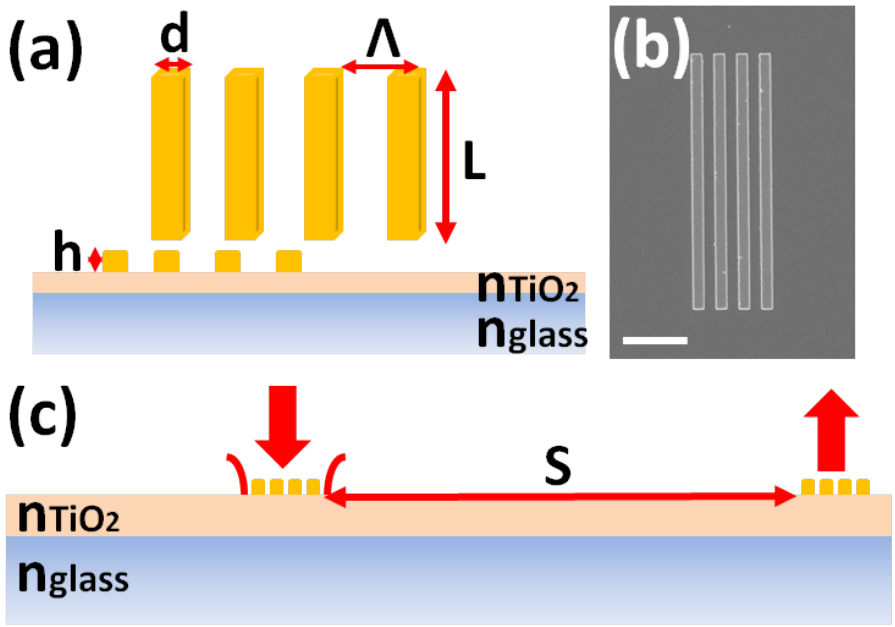

Fig. 5.1 Scheme of the coupler and decoupler system. (a) The detail of each dimension of the coupler grating. L, d, h represent the length, width and height of gold bars which are fixed at 4 μm, 180 nm and 50 nm. The period (Λ) is twice longer than the width. The effective index of TiO_2 (n_{TiO_2}) is measured 1.75 (TM mode) and the index of glass (n_{glass}) is 1.49. (b) SEM image of the coupler grating fabricated by e-beam lithography. The scale bar is 1 μm. (c) Schematic configuration of the coupler and decoupler system. The left-side and right-side gratings respectively serve as a coupler and a decoupler. S indicates the distance between the coupler and the decoupler.

To check the functionality of couplers and decouplers, we combine two similar couplers with a 20 μm separating distance S as displayed in Figure 5.1 (c). The left one serves as a coupler for launching the free-space light into the waveguide and the right one serve as a decoupler for extracting the confined waves out of the waveguide. The aim is to test whether

the light could couple into the waveguide and be re-emitted by the decoupler. In the next section, we will show the experimental images for the coupler and decoupler system.

5.1.2 Performance of the coupler and decoupler system

For the sake of a simple way to couple the light into the waveguide, optimizing the coupling efficiency is not the principal aim for the coupler at this moment. The key point is to evidence that the coupler, especially the decoupler, can work as we expect. Therefore, we show the test images of the coupler and decoupler system in Figure 5.2. The signal on the decoupler, as indicated in the red circles in Figure 5.2 (a), confirms that the light can be coupled into the waveguide using the coupler and can be coupled out of the waveguide using the decoupler as well. The brighter spot on the coupler indicates a large amount of the incident light still

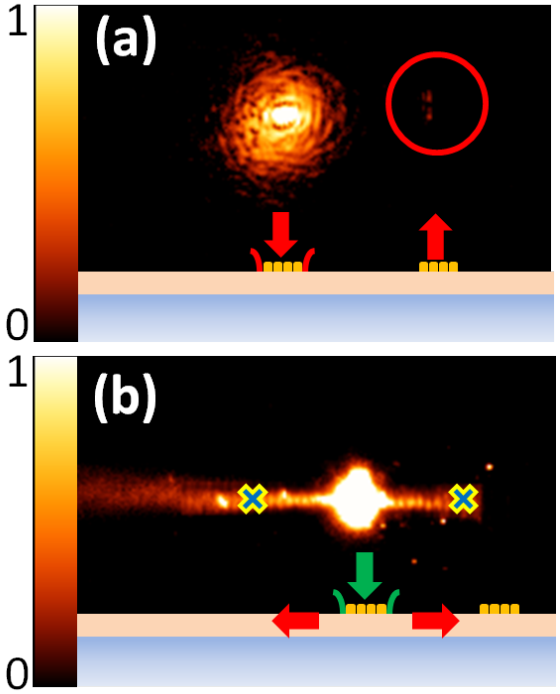

Fig. 5.2 Performance of the coupler and decoupler system. (a) show that red laser impinges on the coupler and the guided light is re-emitted out of the waveguide by the decoupler which is indicated by the red circular rings. The sketch on the bottom indicates the position of the excitation. The image is mathematically employed with a logarithm scale in order to better display the signal from the decoupler. (b) Fluorescence image for the coupler and decoupler system. The green laser impinges on the coupler as indicated in the sketch on the bottom. Two green crosses represent the position at which we measure the intensity. The distances between each cross and the central spot are fixed at 15 μm. The color scales are chosen by arbitrary units.

could not couple into the waveguide and is lost by the transmission, reflection and absorption of the metal. If we take a quantitative measurement for this system, the ratio between the coupler and decoupler with a logarithm scale is obtained 0.505.

In order to further study the light propagation in the coupler and decoupler system, we deposit the CdSe nanocrystals on the surface of the sample and observe the fluorescence image. In Figure 5.2 (b), we display the fluorescence image with filtering out the green excitation light. The strong beams are shown at two sides of the coupler corresponding to the coupled light in the waveguide. If we measure the fluorescence intensities on two sides of the coupler, the ratio between the left and right green crosses in Figure 5.2 (b) is obtained 1.08.

As a conclusion, the coupler and decoupler system can realize the light injection and emission. The decoupler on the waveguide provides us a possibility to detect guided waves for our following study about the directional coupling of light. In addition, the fluorescence of nanocrystals shows another possibility to directly visualize the propagation of the coupled light. Both of these two methods will be used for the quantitative analysis of directionality.

5.1.3 Directional propagation in the waveguide

From Figure 5.2 (b), we observe that the strong beam disappears behind the decoupler. It means that the coupler grating may block the light propagation in the waveguide somehow. Thus, we design a triple-coupler system shown in the bottom of Figure 5.3. The separation between three couplers is designed at 3 μm and the distance S between the first coupler and decoupler is still kept the same at 20 μm. Compared with the single-coupler system, we expect that the two more couplers on the left of the first coupler (also called excitation coupler) could reflect and block the coupled light.

From Figure 5.3 (a), we observe that the out-coupling light in the red circle seems to be slightly stronger than the light in the single-coupler system as shown in Figure 5.2 (a). If we take the same quantitative measurement for the triple-coupler system, the ratio between the excitation coupler and decoupler with a logarithm scale is obtained 0.525 which is almost the same value for the single-coupler system. It means that the reflection does not increase with adding two couplers behind the excitation coupler.

Similarly, the fluorescence image is also taken for the triple-coupler system. Noteworthy, we only show the image when the green laser impinges on the left coupler of the triple-coupler system as indicated in the bottom of Figure 5.3 (b). An interesting effect draws our attention. We clearly observe a strong directional beam on the left side of the excitation coupler but almost nothing on the right side. If we measure the fluorescence intensities on two sides of the excitation coupler with the same distance like the single-coupler system, the ratio between the left and right green crosses is obtained 57.04 which is enormously higher than

the ratio in the single-coupler system. This ratio gives us an intuitive idea for the directional coupling of light into the waveguide with the triple-coupler system.

In order to understand the possible reasons for the strong directional beam, we did more tests with different positions on both the direct plane (DP) and Fourier plane (FP). Besides, we also use spectroscopy to measure the wavelength of the strong directional beam which helps us to clarify the composition of the strong beam.

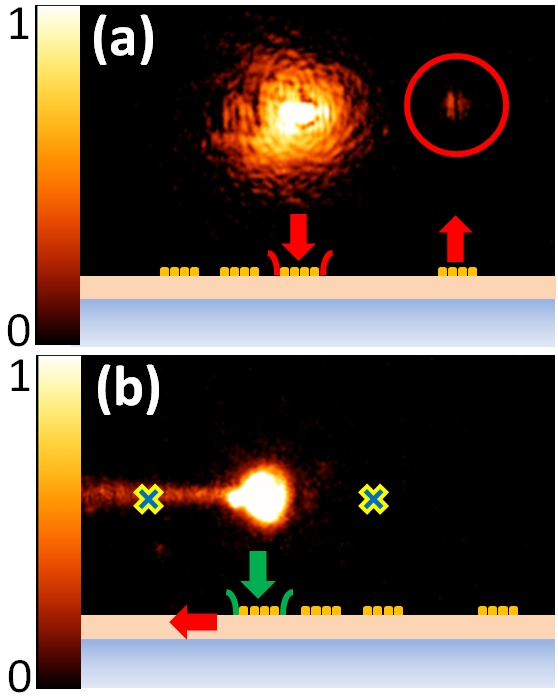

Fig. 5.3 Performance of the triple-coupler and decoupler system. (a) show that red laser impinges on the triple-coupler and the guided light is re-emitted out of the waveguide by the decoupler which is indicated by the red circular rings. The sketch on the bottom indicates the position of the excitation. The image is mathematically employed with a logarithm scale. (b) Fluorescence image for the triple-coupler and decoupler system. The green laser impinges on the coupler as indicated in the sketch on the bottom. Two green crosses represent the position at which we measure the intensity. The distances between each cross and the central spot are fixed at 15 μm. The color scales are chosen by arbitrary units.

The laser is excited at two different positions which are indicated as 1 and 2 in Figure 5.4 (a). With illumination of all the structure by the white light, we can make sure the excitation laser is well placed as we expect (see Figure 5.4 (b), (e)). From two spectral images as shown in Figure 5.4 (d), (g), we observe that almost no signal corresponds to the excited wavelength (532 nm) as indicated by the green arrows and most of the signal corresponds to the wavelength of the fluorescence (650 nm) as indicated by the red arrows. It confirms

that the strong directional signal is all from the fluorescence of nanocrystals on the sample surface. Besides, each FP image clearly shows a bright line corresponding to the guided mode in the waveguide on the same side of the strong directional beam which is indicated by the yellow arrows in Figure 5.4 (c), (f). It means that the incident green light couples into the waveguide and propagates along only one direction. Then, the confined wave excites the nanocrystals on the surface of the sample. Besides, the strong directional beam is not attributed to the directional scattering of the excitation light on the surface because the Figure 5.3 (a) without nanocrystals does not show the directional scattering. In brief, according to the results of these tests, we conclude that the directional beam effect is due to the absence of the coupled green laser propagating along one direction.

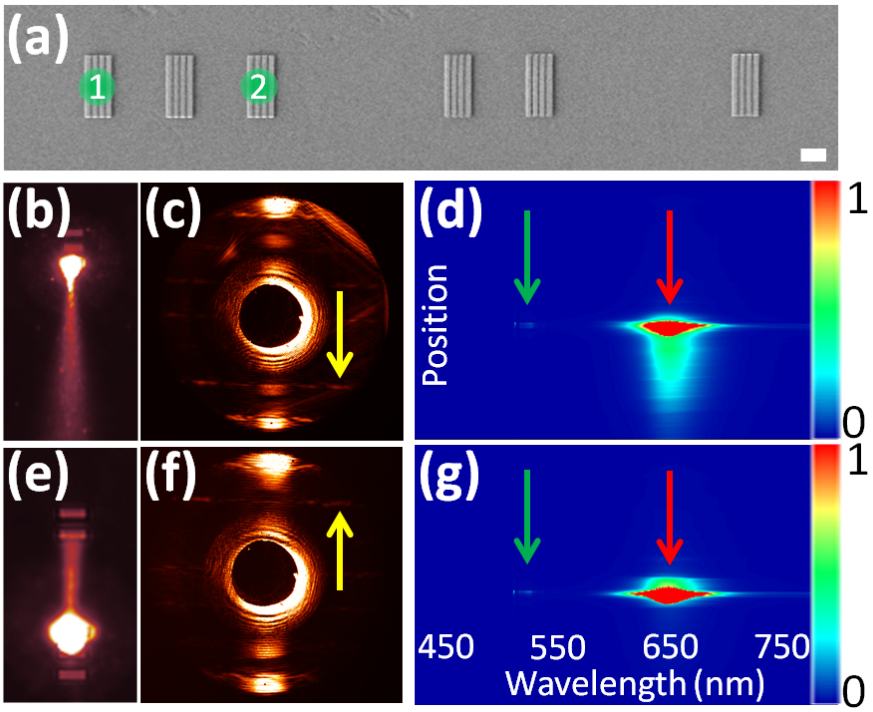

Fig. 5.4 Fluorescence and spectral images of the triple-coupler system. (a) SEM images of the triple-couper system. The green spots indicate the excitation position of the green laser beam. The scale bars is 1 μm. (b), (e) The DP fluorescence images are recorded with the white light and the green laser excitation at position 1 and 2 respectively. The white light provides the illumination for the whole sample. (c), (f) The FP images correspond to the (b) and (c) respectively. The yellow arrows indicate the bright lines corresponding to the guided modes. (d), (g) Spectral images correspond to their fluorescence images (b) and (e) without the white light illumination. The green and red arrows indicate the wavelengths corresponding to 532 nm or 650 nm respectively. The color bars are chosen by arbitrary units.

5.1.4 Waveguide beam block

After confirming several issues from the tests in the last section, it remains two possibilities to contribute this directional propagation in the waveguide. First assumption, the coupled wave may be all decoupled out of the waveguide by the rest couplers at the backside of the excited coupler. Second assumption, the triple-coupler system might strongly modify the fluorescence lifetime of nanocrystals which increases the emission intensity along a specific side namely the Purcell effect. As we known, when nanocrystals are close to a metal resonance cavity, the spontaneous emission rate of the fluorescence will be increasingly enhanced. Thus, we did a numerical simulation and several supplementary experiments about the lifetime of nanocrystals to confirm our assumptions.

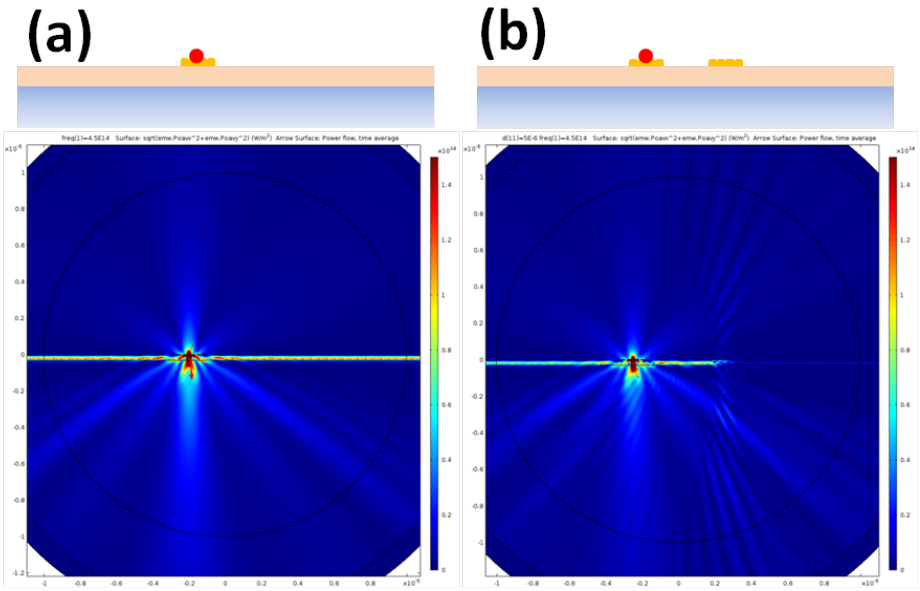

Fig. 5.5 (a) Simulation image for the single-coupler system. The image on the top show the position of the dipole source. (b) Simulation image for the double-coupler system and the position of the dipole source is displayed on the top.

Firstly, we implemented a numerical simulation using the software Comsol with the help of an expert Aurélien Crut. In the 2D simulation, we design a double-coupler system with the same parameters of the sample and a dipole is placed in the center of the excited coupler as shown in Figure 5.5. From the simulated images, we observe a symmetric field distribution in the single-coupler system. The 8% of the emission light from the dipole is coupled into the waveguide and propagates along the two directions. In the double-coupler system, 7% and 0.7% of the emission light are obtained for propagating to the left and right ends of the waveguide respectively. It means that reflection is not presented in the waveguide because

no enhancement for the left side. From the simulated image in Figure 5.5 (b), the guided wave propagating to the right side is observed to re-emit in the free space at the second coupler position. It confirms that no more light is reflected to the left side and almost all the guided wave is decoupled from the waveguide by the second coupler. Besides, we also try to vary the distance between two couplers from 3μm to 5μm. The ratio of the light intensity between the left and right ends of the waveguide is always kept as 10, which means that the ratio is independent for the distance between two couplers. It confirms again that directional beam appears because the guided light along one side is completely blocked by the coupler absorbing in the way of decoupling the confined waves out of the waveguide.

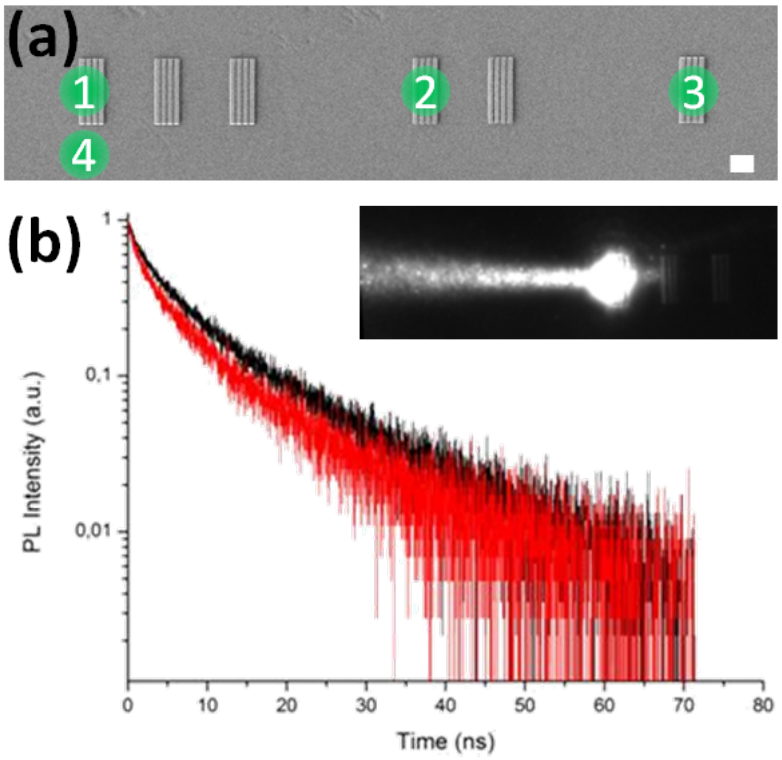

Fig. 5.6 Lifetime measurement for the coupler systems. (a) SEM images of triple-, double- and single coupler system. The green spots indicate the excitation position of the green laser and they are also the positions for the lifetime measurement. (b) The curve of photoluminescence decay shows the log scale of fluorescence intensity as a function of the time. The red and black curves represent the fluorescence decays of the CdSe nanocrystals at the position 1 and 4 indicated as the green spots in Figure 5.6 (a) respectively. The inset shows the fluorescence image when the laser spot is excited at position 1.

Secondly, we measure the lifetime of the CdSe nanocrystals at four different positions which is shown in Figure 5.6 (a). The positions 1, 2 and 3 correspond to the triple-, double- and single-coupler system respectively. The fluorescence of nanocrystals at position 4 without

the gold structure is chosen as the reference. The curves of the photoluminescence decays of the CdSe nanocrystals at positions 1 and 4 are shown in Figure 5.6 (b). These decay curves can be well fitted by a bi-exponential function which is expressed as [166–168]:

$$I(t) = A_b \exp^{-t/\tau_b} + A_g \exp^{-t/\tau_g}, \tag{5.3}$$

where I(t) represents the photoluminescence intensity as a function of time. The τ_b and τ_g denote the life times of bright and grey states corresponding to the radiative and nonradiative (Auger) recombination respectively. The A_b and A_g indicate the proportions of these two states [169, 170].

We show the fitted results of the fluorescence decay of each position in Table 5.1. The changes of the lifetime compared with the lifetime in position 4 (without couplers) are also determined as shown in the column $\Delta\tau_g$ and $\Delta\tau_b$ in percentage. We observe that the number of couplers in the coupling system does make influence on the Auger lifetime but almost no changes for the radiative lifetime. Thus, concerning the second assumption, we conclude that the Purcell effect has a few influence on the fluorescence lifetime of nanocrystals in our system. We can neglect this very small possibility for leading to the strong directional beam.

Table 5.1 The fitted results of lifetime measurement.

Position	τ_g (ns)	A_g	$\Delta\tau_g$ (%)	τ_b (ns)	A_b	$\Delta\tau_b$ (%)
1	2.39	0.25	30	19.05	0.62	8
2	2.49	0.10	27	20.50	0.77	1
3	2.81	0.11	18	20.49	0.77	1
4	3.43	0.11	ref.	20.66	0.79	ref.

As a conclusion, the strong directional beam mainly results from the absorption by the coupler which is placed on the backside of the excited coupler. The periodic strips of the coupler serves well as the decoupler which can radiate almost all the guided light into the free space. Thus, the triple-coupler system is proven to work as a beam block for waveguides so as to realize the directional control of the coupled light. Furthermore, the nanocrystals on the waveguide provides us a simple way to illustrate the propagation of confined waves in the waveguide which will bu used to study the directional coupling light into the waveguide by the Λ-shaped antennas in the next section.

5.2 Optical spin-orbit coupling into the waveguide

In the last section, we show a triple-coupler system and confirm that the directional propagation in the waveguide is attributed to the coupler which block all the light propagating to one

side. Now, we propose a more efficient way to directly couple the incident beam in a given direction controlled with polarization. As few paper about the directional coupling of light into the waveguide is reported, we do not have more references for the coupler structures. Therefore, we propose to use a similar configuration of Λ-shaped antennas as what we described in Chapter 4. Geometrically, the difference is that the sample is fabricated by using the electron-beam lithography (EBL) instead of the focused ion beam (FIB) milling. It means that the gold Λ-shaped strips are deposited on the waveguide rather than the Λ-shaped apertures engraved on the gold film.

The dark field imaging is firstly employed for testing whether the Λ-shaped antennas could work for the directional coupling of light into the waveguide. Then we deposit the CdSe nanocrystals on the surface of the sample in order to visualize the propagation of the coupled light in the waveguide. The fluorescence images and the dark field images evidently show that the optical spin-orbit coupling of light into the waveguide can be achieved by the Λ-shaped antennas.

5.2.1 Realization of the spin-orbit coupling by dark field imaging

The SEM image of the array of Λ-shaped antennas is shown in the inset of Figure 5.7 (a). The parameters of each elementary Λ-shaped ridge are kept the same as the elementary Λ-shaped slit which are 200 nm, 50 nm and 160 nm for the length (L), width (W) and the distance between two center of the elementary slits or ridges (D) respectively. The height (h) of the gold ridge is 50 nm deposited directly on the waveguide. The apex angle (α) is chosen at 45° for the first test. The periods of the 4×4 array along the Ox and Oy direction are fixed both for 650 nm. Four decouplers are deposited 10 μm away from the array on the Ox and Oy direction. An image under the white light illumination is shown in Figure 5.7 (a).

We firstly describe the decouplers on the vertical direction (Oy axis). When we look at the dark field images under the linear polarization in Figure 5.7 (b) (only the horizontal linear polarization indicated as the red arrow is shown here), the intensities of two decouplers along the Oy axis re-emit the guided light with different intensities. In order to quantify the directional coupling effect, we involve the parameter V as the directivity to represent the capacity of the coupling directionality. It was defined in Chapter 4 as $V = \frac{|I_+ - I_-|}{I_+ + I_-}$. The directivity V along Oy axis for the linear polarization is obtained 0.23±0.02 and $V = 0.26 \pm 0.02$ and $V = 0.19 \pm 0.04$ for the left- (LCP in Figure 5.7 (c)) and right-handed circular polarization (RCP in Figure 5.7 (d)) respectively. We observe that the upwards and downwards couplings are independent for the incident polarization. The similar results for the directivity of the unidirectional scattering have been explained in ref. [9].

The more interesting feature occurs in the horizontal direction (Ox axis). The directivity along the Ox axis is extracted in the same way as above. For a linear polarization, $V = 0.01 \pm 0.01$ which means no difference for the intensities on the left and right decouplers. But for the circular polarization, $V = 0.56 \pm 0.06$ and $V = 0.69 \pm 0.08$ for LCP and RCP respectively. Specifically, light couples into the waveguide and propagates to the left side under the LCP and light propagates to the right side under RCP. This shows that a strong control of coupling direction for guided waves can be obtained with incident polarization, which has never been done before.

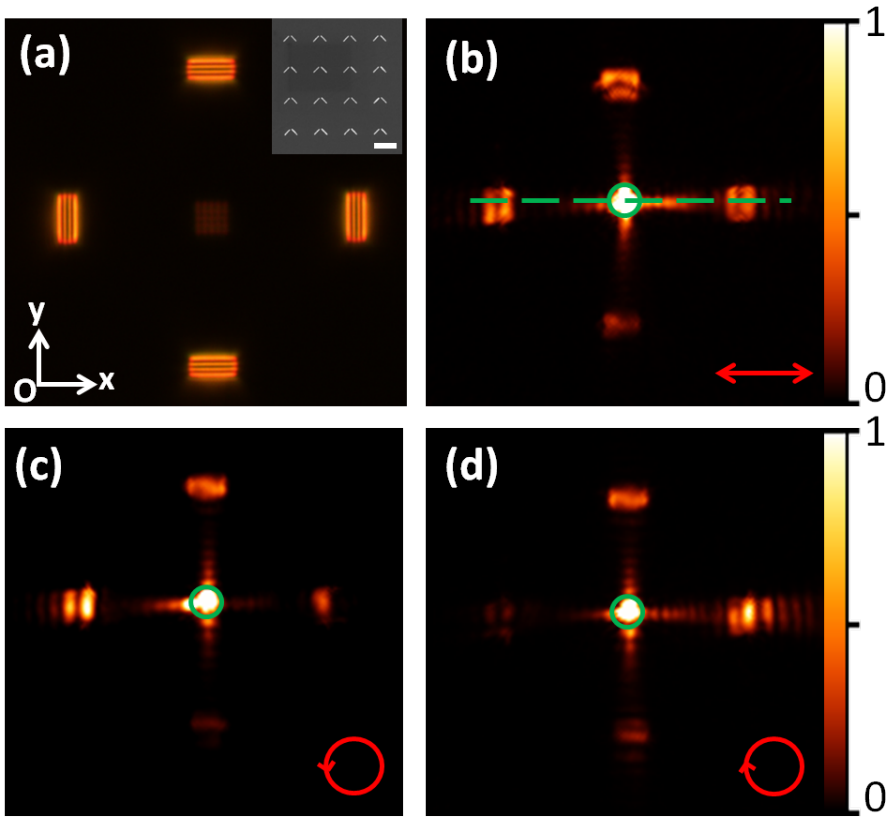

Fig. 5.7 (a) White light illumination of the whole structures. The inset is the SEM image of the central array part with a 500nm scale bar. (b) Dark field image with linear polarized excitation as indicated by the red arrow. The red laser (λ =633nm) is weakly focused on the whole array of the Λ-shaped ridges shown in the green circle. The cross-section profile is analyzed along the dashed green line. (c), (d) Dark field image with the LCP and RCP excitation. The red circles indicate the direction of the circular polarization. The intensity bar is an arbitary unit.

The directivity V$\simeq$0 along the Ox axis under the linear polarization confirms that no preferred coupling direction appears without introducing the circular polarization and the

incident excitation of laser beam normally impinge on the array. The high directivity along the Ox axis under circular polarization affirms that the optical spin-orbit coupling into the waveguide works well not only for SPP coupling but also for coupling the free-space light into the waveguide. Subsequently, we try to optimize the directivity with the apex angle as indicated in Figure 5.8 (a). Two values of apex angles $\alpha = 30^\circ$ and $\alpha = 60^\circ$ are checked. The dark field images of array of Λ-shaped strips with $\alpha = 60^\circ$ under the LCP and RCP are display in Figure 5.8. We observe the less difference of intensities between the left and right decouplers. The directivities for $\alpha = 60^\circ$ are obtained $V = 0.32 \pm 0.08$ and $V = 0.38 \pm 0.07$ under the LCP and RCP respectively. $V = 0.25 \pm 0.11$ and $V = 0.33 \pm 0.08$ are obtained for $\alpha = 30^\circ$ under the LCP and RCP respectively. Interestingly, we find that Λ-shaped antennas with $\alpha = 45^\circ$ achieve the maximum directivity instead of 60° which is optimized for the SPP directional coupling.

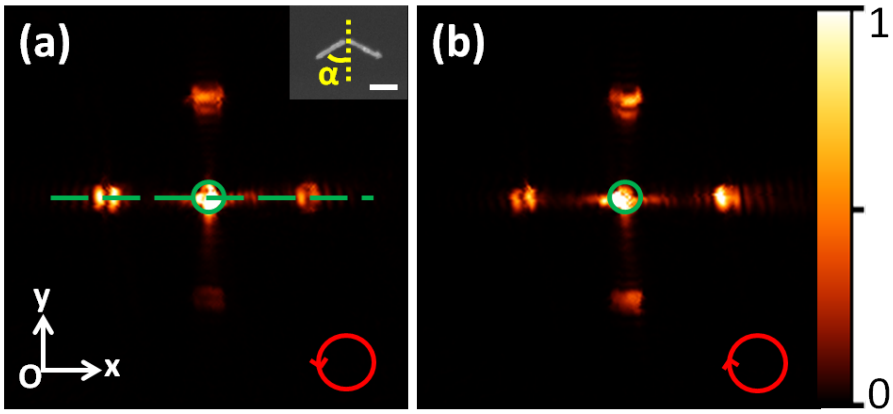

Fig. 5.8 (a) Dark field image for Λ-shaped antennas with $\alpha = 60^\circ$ under the LCP excitation as indicated by the red arrow. The red laser spot is shown in the green circle. The cross-section profile is analyzed along the dashed green line. The inset is the SEM image of one Λ-shaped antenna with a 100nm scale bar. The apex angle α is indicated as 60° in this case. (b) Dark field image with the RCP excitation as indicated by the red circles. The intensity bar is an arbitary unit.

Now, we try to analyze the difference between nanostrips and nanoslits. In fact, the mechanisms for generating electric dipoles are quite different for the case of slits (apertures) and stripes (ridges). On one side about a slit on the gold film, the excited dipole, which is perpendicular with the slit, serves as a major-axis dipole because the electrons are more easily accumulated along the length of the slit. On the other side about a gold stripe on the dielectric film, the excited dipole, which is parallel with the stripe, serves as a major-axis dipole because the electrons on the gold stripe are more easily moved along the length of the stripe [9]. Thus, the weighted contribution for the major-axis and minor-axis dipoles (β as

we mentioned in Chapter 4) is modified. β is evaluated close to 0 for the gold stripe which is much lower than the case for slits. That is why the maximum value of directivity could be reached by the apex angle $\alpha = 45°$. Here, we just give a rough approximation to adapt our multidipolar model. In fact, the dipole distribution is more complicated in the case of nanostrips. We did not consider the interaction between the dipoles of each antennas. If we take the interaction into account, the position of each dipole might be changed due to the inhomogeneous accumulation of electrons on the gold strips which need more systematical investigation on it. In the following experiment, we will use Λ-shaped antennas with $\alpha = 45°$ for all the cases.

5.2.2 Evidence of the spin-orbit coupling by fluorescence imaging

Due to the limitation of the length of four decouplers around the central array, we can not

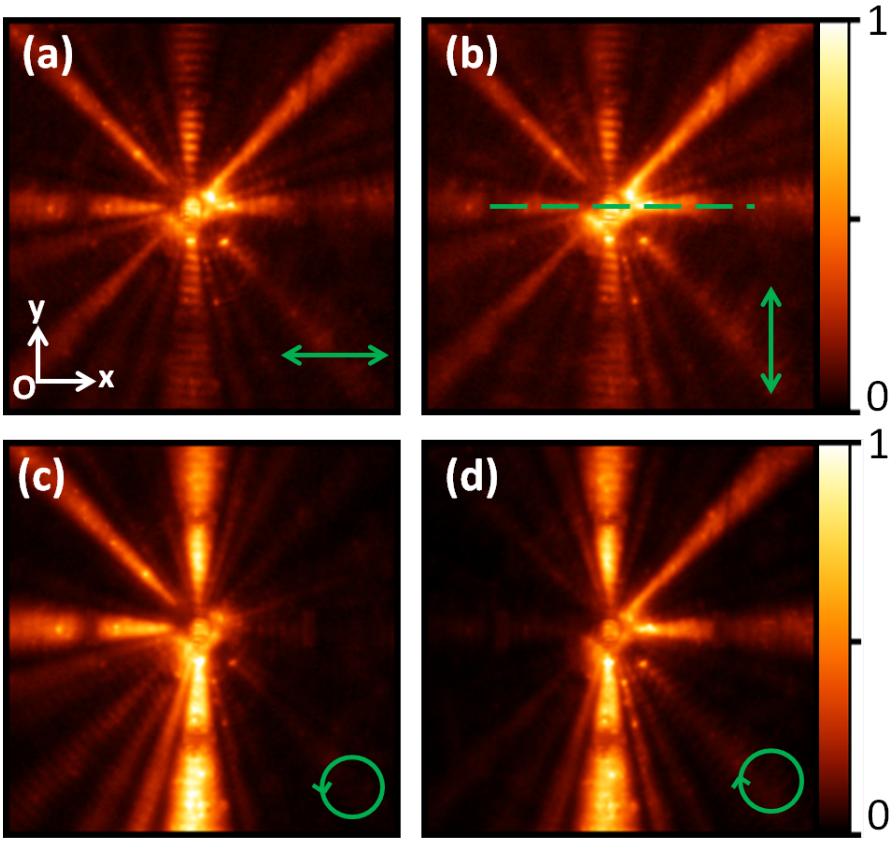

Fig. 5.9 Fluorescence images of nanocrystals deposited on the sample. (a), (b) The incident green laser (λ =532nm) is illuminated the array with linear polarization indicated by the green arrows. (c), (d) Fluorescence images under the LCP and RCP excitation clearly show unidirectional coupling of light into the waveguide. The intensity bar is an arbitrary unit.

detect the coupled light which propagates to the other direction. So we deposit the CdSe nanocrystals on the sample surface so as to visualize how the coupled light propagates in the waveguide. Keeping the dark field setup, we just change the excited source to the green laser and add a filter before the CCD camera to select the wavelength larger than 633 nm.

The green laser with the linear polarization firstly illuminates the array of Λ-shaped antennas. The fluorescence images with two direction of linear polarization are recorded in Figure 5.9 (a) and (b). From these two images, we observe that there are four strong beams propagating along the diagonal of the array besides the four strong beams along the Ox and Oy axis. The strong beam along each opposite direction does not show the different intensities. It means that no directional coupling of light into the waveguide under the linearly polarized excitation. In the case of circular polarization, we see the strong directional coupling effect as shown in Figure 5.9 (c) and (d). When the array of Λ-shaped antennas is excited by the green laser with the LCP, most of the coupled light propagates to the left side even along the diagonal to the left. On the right side, neither the Ox axis nor the diagonal do not show any strong beam. On the contrary, the coupled light propagates to the right side under the RCP excitation. Although the fluorescence image is not very precise for the quantitative analysis of the directivity, the strong beams can clearly help us to efficiently visualize the propagation of the directional coupled light. In brief, the fluorescence images confirm again that the optical spin-orbit coupling effect works as well for the antennas-waveguide system. Furthermore, the directional coupled light propagates not only along the Ox axis but also along the diagonal of the array. In conclusion, we show experimentally that the directional coupling of light into the waveguide controlled with polarization can be achieved by Λ-shaped antennas. This strong directional coupling is expected to be used for new devices of integrated optics.

5.3 Reciprocal effect of spin-orbit coupling

After realizing the spin-orbit coupling of light into the waveguide, another issue interests us so much which is whether we could observe the reciprocal effect of spin-orbit coupling. It means whether we could detect the different circular polarization when a guided light coming from the left or right side of the array of Λ-shaped antennas. As a matter of fact, this effect is very challenging to observe because the light diffracted by the array of Λ-shaped antennas is very complicated to analyze. There are few papers mentioned about this issue theoretically but they hardly prove the expectation experimentally [83, 171]. Here, we firstly record all the polarization diffracted by the array on the Fourier plane (FP) with the help of Stokes parameters. Subsequently, we modify our previous analytical model to adjust the

reciprocal effect in order to explain the experimental results. Lastly, we achieve to observe the reciprocal effect of spin-orbit coupling by selecting the diffraction order on the FP.

5.3.1 Output polarization analysis

The same structure can be used for testing the reciprocal effect of spin-orbit coupling. Now the decouplers serve as the couplers in order to generate the guided light propagating to the central array part. We firstly take the case shown in Figure 5.10 (a) as an example. The red laser impinge on the left coupler and we are interested on the diffracted light on the array of Λ-shaped antennas as indicated in the red zone of Figure 5.10 (b). This experimental image show us two spots on the right of the excited coupler which correspond to the central array and the right coupler. The right spot is stronger than the central spot which means that the array of Λ-shaped antennas does not work as well as the coupler for light decoupling but the intensity of decoupling light on the central array is sufficient for our following analysis. Subsequently, the polarizer (P) and quarter-wave plate (QWP) are added to the setup in front of the CCD cemera aiming at a quick output analysis. But unfortunately, it does not work as we expect. The central spot can not be completely extincted with any circular polarization. It means that the diffracted light can not directly generate the circular polarized states. Therefore, we implement an output analysis on the FP to further study the diffracted light by the array of Λ-shaped antennas.

For the systematical analysis for the polarization, we introduce a motor for turning the QWP. After calibration of the QWP and P with the record system, we save all the images once the motor turns for each 15°. Thus, 24 images from 0° to 360° helps us to obtain all the intensity under different polarization states which lead to determine all the Stokes parameters at each point. Then, we reconstruct the polarization states of each pixel directly on the recorded image which is shown in Figure 5.10 (c). From the polarization analysis on the FP, we observe 9 bright spots on the FP which correspond to the different diffraction orders by the array of Λ-shaped antennas. Specifically, the three orders of each line do not have the same polarization states but each column has almost the same polarization. Let us take the bottom line as an example. The central spot shows the linear polarization and the left and right spots are determined as the RCP and LCP separately. Noteworthy, the experimental results show that the polarization on the two sides are not perfectly circular but a little bit elliptical. This imperfection of the polarization may result from the inaccuracy of the measurement. In fact, this small ellipticity does not influence the important effect which is that the polarization states on the left and right orders have the opposite phases as indicated by the white or black color for the polarization representation. In order to understand the

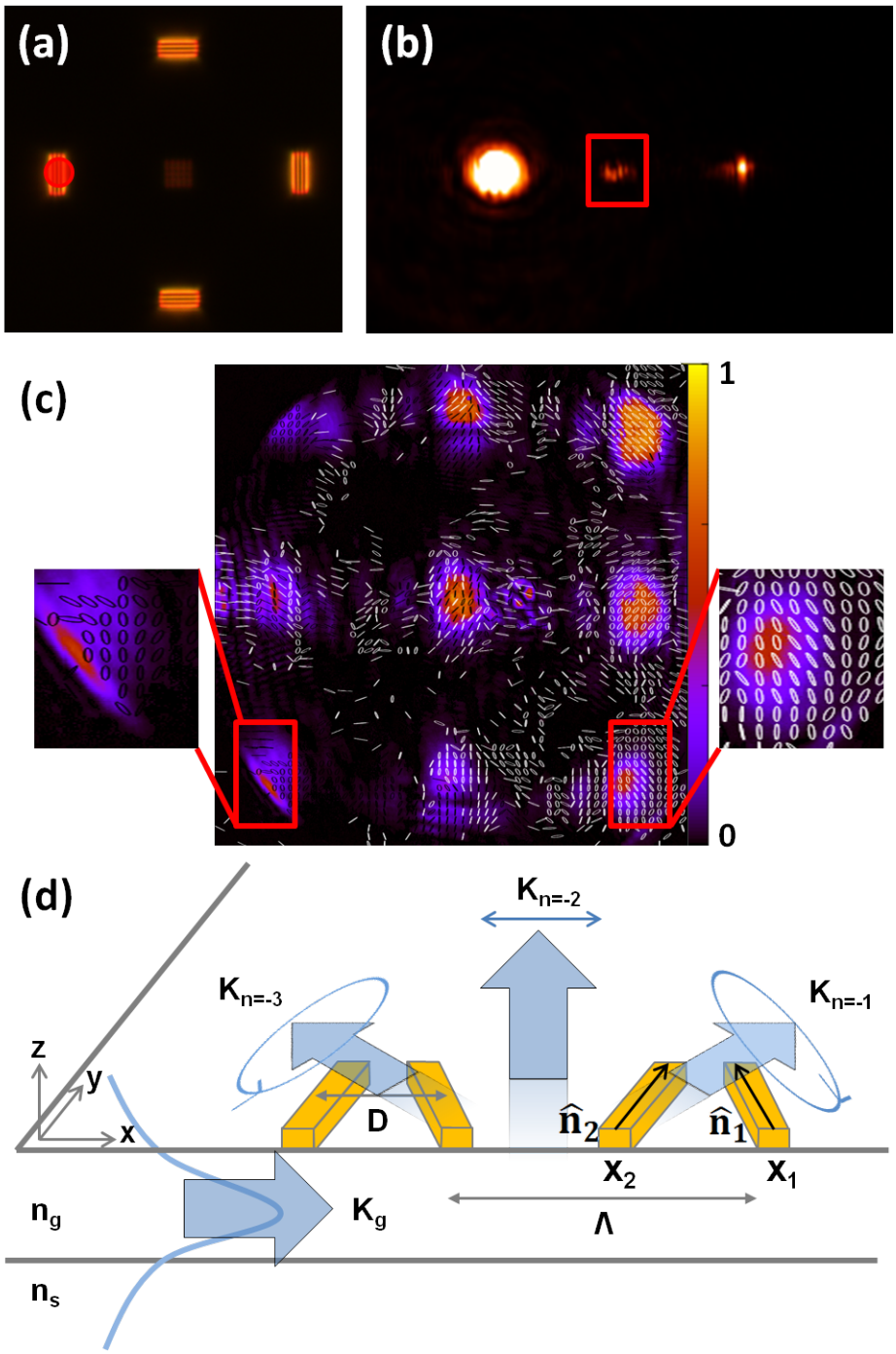

Fig. 5.10 Reciprocal spin-orbit coupling effect demonstrations. (a) The DP image with the white light illumination The red spot indicate the position of the incident excitation. (b) Experimental DP image. The red box indicates the place for the FP imaging shown in (c). (c) Polarization analysis of each 16 pixels on the FP. Each 16 pixels have a sign of polarization. The black and white color of the polarization states represent the different directions of circular or elliptical polarization. The two insets indicate that the polarization state on the left side reverses the direction of the polarization state on the right side. (d) Sketch of the reciprocal effect. The guided light propagates from the left to right. Three main orders of diffraction light along the Ox axis show the different polarization states.

reason why the diffracted light has the different polarization, we analogically develop our previous analytical model to adjust the case for the reciprocal effect.

Our analytical model is divided into two parts. First of all, we will study the possible diffraction orders on the FP. Secondly, the phase analysis of each order will be discussed. A schematic diagram of the reciprocal effect is displayed in Figure 5.10 (d).

a. Diffraction orders on the Fourier plane

According to the conservation of angular momentum, the wave vector diffracted by the array of Λ-shaped antennas (K_n) should respect:

$$K_n = K_g + \frac{2\pi}{\Lambda} n, \tag{5.4}$$

where K_g represents the wave vector of the guide mode which could be determined by $K_g = \frac{2\pi}{\lambda_0} N_{eff}$ (here we know the incident laser wavelength and the effective refraction index of waveguide). The integer number n represents the order of diffraction and Λ is the period of the array of Λ-shaped ridges indicated on the Figure 5.10 (d).

The visible order on the Fourier plane is limited by the numerical aperture of the objective (N.A.=1.49). For example, if the grating period Λ is fixed at 650nm, the visible diffraction order n along the Ox axis could be taken with three values -1, -2, -3. K_{-1}, K_{-2}, K_{-3} located respectively on the right side, the center and the left side of the FP. These three determined orders explain why three spots each line appear on the experimental FP image. Then, these three orders will be taken into the consideration for the next step.

b. Phase analysis for the different orders

The analytical model for the Λ-shaped apertures can be used for ridges except the major-dipole ($\widehat{n}_1$ and $\widehat{n}_2$ indicated in Figure 5.10) direction along the length of the ridges instead of perpendicular with the length of the slits. The total electric field radiated by one single Λ-shaped antenna excited by the guided light in the waveguide is shown below:

$$\overrightarrow{E}(K) \propto ((\widehat{n}_1 \cdot \overrightarrow{E_g}(x_1))\widehat{n}_1 \exp^{-i\overrightarrow{K_n}\cdot\overrightarrow{x_1}} + (\widehat{n}_2 \cdot \overrightarrow{E_g}(x_2))\widehat{n}_2 \exp^{-i\overrightarrow{K_n}\cdot\overrightarrow{x_2}}), \tag{5.5}$$

where $\overrightarrow{x_1}$ and $\overrightarrow{x_2}$ represent the position of two dipoles which is fixed in the center of the ridges. If the origin is set the middle of the Λ-shaped ridges, $\overrightarrow{x_1}$ and $\overrightarrow{x_2}$ will be $\frac{D}{2}$ and $-\frac{D}{2}$. $\overrightarrow{E_g}$ denote the electric field of the guided wave in the waveguide. If we assume that the guided wave field propagates only along $\widehat{x}$, it is expressed as $\overrightarrow{E_g} \propto \exp^{i\overrightarrow{K_g}\cdot\overrightarrow{x}}$. Therefore the total electric field radiated by one Λ-shaped ridges is simplified as:

$$\begin{aligned}\overrightarrow{E}(K) &\propto (\widehat{x}-\widehat{y})\exp^{i(K_g-K_n)\frac{D}{2}}+(\widehat{x}+\widehat{y})\exp^{-i(K_g-K_n)\frac{D}{2}},\\ &\propto (\widehat{x}-\widehat{y})\exp^{-i\frac{nD}{\Lambda}\pi}+(\widehat{x}+\widehat{y})\exp^{i\frac{nD}{\Lambda}\pi}.\end{aligned} \tag{5.6}$$

In our case, $\frac{D}{\Lambda}=\frac{1}{4}$ since D is fabricated around 160nm and we choose the period 650nm for observation. Therefore, the total electric fields of three orders of diffraction are listed below:

$$\begin{aligned}\overrightarrow{E}(K_{n=-1}) &\propto \widehat{x}+i\widehat{y},\\ \overrightarrow{E}(K_{n=-2}) &\propto i\widehat{y},\\ \overrightarrow{E}(K_{n=-3}) &\propto \widehat{x}-i\widehat{y}.\end{aligned} \tag{5.7}$$

The three visible orders have three different polarization states which are LCP, linear, RCP corresponding to the right, central and left spots on the FP. Thus, the results from the analytical model confirm the possibility to achieve the reciprocal effect of spin-orbit coupling by selecting the expecting diffraction order on the FP. The output polarization states could be controlled by changing the period of the array and the distance between each ridge. Noteworthy, we do not consider the interaction between each two Λ-shaped ridges in our model. With involving the interaction between each ridge, the output polarization could be modified slightly. This is also a reason why we can not achieve the perfect circular polarization from the experimental results.

5.3.2 Realization of the reciprocal effect

In the last section, we confirm our expectation about the realization of the reciprocal effect based on the analytical model. We firstly excite the right coupler as indicated in the inset of Figure 5.11 (a). Then, the right part of the FP is selected by a diaphragm as shown in the inset of Figure 5.11 (b). It means that the left part of the PF is blocked and only the signal on the right part of the PF (right side of the white line in the inset of Figure 5.11 (b)) can be collected by the CCD camera. The filtered PD images with two opposite polarization analysis are displayed in Figure 5.11 (a) and (b). We observe that the maximum intensity on the central array appears when the RCP analysis is applied. Almost no light appears in the central part when the LCP analysis is added. Thus, the diffracted light in the center is determined as the RCP. On the contrary, if we excite the left coupler and filter the same region on the FP (see the inset in Figure 5.11 (c) and (d)), the strong signal in the central

part is clearly observed with the LCP output analysis and the signal in the center with the RCP analysis is hardly seen. It means that all the radiated light in the center is the LCP. It confirms again the reciprocal effect can be realized by selecting the expecting part on the FP.

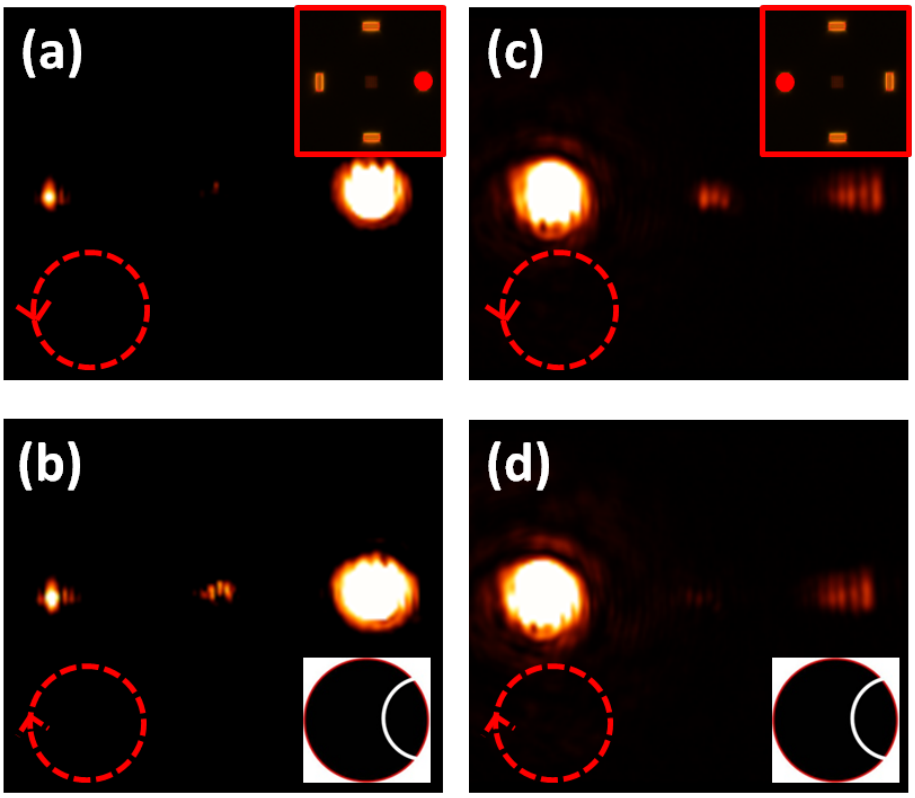

Fig. 5.11 Realization of the reciprocal effect on the DP by filtering the zone on the FP. (a), (b) The red laser spot is excited at the same position as indicated by a red spot in the inset of (a). The diffraction order is selected by a diaphragm on the FP as indicated in the inset of (b). The right part of the white line shows the region of interest on the FP. With the polarization output analysis, the decoupled light in the central part is proven as a RCP state. (c), (d) The laser spot impinge on the right coupler as indicated in the inset of (c). With filtering the same region on the FP shown in the inset of (d), the light in the central part is observed as a perfect LCP state. The arrows with red dashed lines represent the output polarization analysis.

As a conclusion, a simple grating coupler and decoupler system is well developed at the beginning. Then, a triple-coupler system is proven to work as a beam block for realizing the unidirectional propagation of the guided waves. Furthermore, the Λ-shaped antennas fulfill the directional coupling of light into the waveguide by the methods of dark field and fluorescence imaging. The nanocrystals deposited on the waveguide provide an efficient way to illustrate the propagation of confined waves in the waveguide. Lastly, the reciprocal effect of spin-orbit coupling is investigated both experimentally and theoretically. The analytical model helps us to understand the reason of the different polarization on the FP. With the

FP selection, we can realize the control of the extraction properties of a guided mode by the Λ-shaped antennas. Specifically, the light can be radiated from the Λ-shaped antennas with opposite circular polarization when the guided light comes from the different directions. Thus, the reciprocal effect of spin-orbit coupling can be used to detect the direction of the guided modes through the polarization of extracted light. Such device will be applied to integrated optics such as demultiplexer, demodulation, quantum information and processing etc.

Conclusion and perspective

This project about the directional control of light is associated with both fundamental research and emerging applications. Thus, the experiment and theoretical studies are both implemented during the 3-year investigation. The basic knowledge about Surface Plasmon Polaritons (SPPs) and dielectric waveguides has been well understood. The methods for nanopatterning such as Focus Ion Beam (FIB), Electron Beam Lithography (EBL) and the thin film waveguide preparation have been intensively used and more than 15 batches of samples have been developed. Concerning the experimental setup, the Leakage Radiation Microscopy (LRM) was constructed piece by piece at Institute Néel in Grenoble and the dark field microscopy was modified and aligned based on the LRM at Institute Lumière Matière (ILM) in Lyon. Working in two groups provides an opportunity to combine the advantages of each laboratory and to achieve the best results. As a conclusion about both the experimental and theoretical results, we firstly talk about the spin-driven directional and singular SPP generation and then the spin-orbit coupling and its reversed effect on the waveguide.

By means of LRM, our plasmonic systems made of Λ-shaped apertures on the gold film prove to induce spin-controlled SPP directionality decoupled into the far-field. Furthermore, a comparison between simulation and experimental data shows that our theoretical model well reproduces the experimental results and allows precise determination of dipole contributions in the SPP radiated field. Simultaneously, the understanding of the mechanism helps us to unify the other plasmonic structures such as T-shaped apertures. Furthermore, optimization of the directivity based on the analytical model is achieved experimentally. In addition, within the chiral circular gratings, radial propagation and singular SPP formation are demonstrated with LRM. By selecting the proper input and output polarization states, we map SPP singularity and Bessel vortices on the direct space. We have shown that the LRM characterization method makes quantitative analysis possible for polarization tomography. Lastly, the optimization of the extinction ratio is realized by modifying the apex angle of the Λ-shaped apertures. All of these findings offer a promising way for device development in the field of nanophotonics, such as plasmonics information processing, optical tweezers [88], particle trapping [89], etc.

Concerning the directional coupling of light into the waveguide, we also obtained some important results. Firstly, we report that the simple triple-coupler system work as a beam block for radiating all the confined light out of the waveguide. By introducing the nanocrystals, the unidirectional propagation of the guided waves is revealed under fluorescence imaging. Then, the gold Λ-shaped antennas deposited on the waveguide help us to realize the spin-orbit coupling of free-space light into the waveguide like the SPP coupling. Furthermore, the reciprocal effect is observed and thoroughly studied. The imperfection of the output polarization is due to the presence of the different diffraction orders by the antennas. Thus, we analyze the polarization states of different orders on the Fourier plane by Stokes parameters. The linear polarization is found in the central order of diffraction and two opposite circular polarization states locate at each side. With the helps of the experimental results and an analytical model, we finally obtain the output circular polarization by selecting the expected region on the Fourier plane. This effect plays an important role for developing the opto-electronic device to distinguish the direction of the signal propagating in the waveguide through analyzing the polarization of the extracted light. All the investigation for waveguides is expected to have an impact in the emerging field of integrated optics especially for the information processing and analysis.

In addition, the reciprocal effect of spin-orbit coupling is being applied to the case of SPP decoupling into photons. Now we are trying to design a new device for removing the interference from two sources which is called fringe eraser. Specifically, two arrays of the Λ-shaped apertures are engraved on the gold film and a slit is placed in the center of two arrays. When a laser impinges on the central slit, the SPPs will be excited and propagate to the array of Λ-shaped apertures on each side. As the SPPs propagate to the same structures from two opposite direction, the decoupled light should have the opposite polarization each side which can not lead to any interference. Thus, the fringes of each order on the Fourier plane are expected to vanish. If a quantum emitter is introduced in the center of two arrays of Λ-shaped apertures instead of a slit, the device serves as a quantum fringe eraser which can also eliminate the interference from two single plasmons. Therefore, our future work will focus on applications into the quantum domain using single photons coupled to near-field optics [172].

References

[1] Stefan Alexander Maier. *Plasmonics: Fundamentals and Applications*. Springer Science & Business Media, May 2007.

[2] Mark L. Brongersma and Vladimir M. Shalaev. The Case for Plasmonics. *Science*, 328(5977):440–441, April 2010.

[3] Mathieu L. Juan, Maurizio Righini, and Romain Quidant. Plasmon nano-optical tweezers. *Nat Photon*, 5(6):349–356, June 2011.

[4] Terukazu Kosako, Yutaka Kadoya, and Holger F. Hofmann. Directional control of light by a nano-optical Yagi–Uda antenna. *Nat Photon*, 4(5):312–315, May 2010.

[5] Jingjing Li, Alessandro Salandrino, and Nader Engheta. Shaping light beams in the nanometer scale: A Yagi-Uda nanoantenna in the optical domain. *Phys. Rev. B*, 76(24):245403, December 2007.

[6] Tim H. Taminiau, Fernando D. Stefani, and Niek F. van Hulst. Enhanced directional excitation and emission of single emitters by a nano-optical Yagi-Uda antenna. *Opt. Express*, 16(14):10858, July 2008.

[7] Daniel Dregely, Richard Taubert, Jens Dorfmüller, Ralf Vogelgesang, Klaus Kern, and Harald Giessen. 3D optical Yagi-Uda nanoantenna array. *Nat Commun*, 2:267, April 2011.

[8] Yannick Sonnefraud, Sarp Kerman, Giuliana Di Martino, Dang Yuan Lei, and Stefan A. Maier. Directional excitation of surface plasmon polaritons via nanoslits under varied incidence observed using leakage radiation microscopy. *Opt. Express*, 20(5):4893, February 2012.

[9] Dries Vercruysse, Yannick Sonnefraud, Niels Verellen, Fabian B. Fuchs, Giuliana Di Martino, Liesbet Lagae, Victor V. Moshchalkov, Stefan A. Maier, and Pol Van Dorpe. Unidirectional Side Scattering of Light by a Single-Element Nanoantenna. *Nano Lett.*, 13(8):3843–3849, August 2013.

[10] Jing Yang, Xiao Xiao, Chuang Hu, Weiwei Zhang, Shuxiang Zhou, and Jiasen Zhang. Broadband Surface Plasmon Polariton Directional Coupling via Asymmetric Optical Slot Nanoantenna Pair. *Nano Lett.*, 14(2):704–709, February 2014.

[11] Jiao Lin, J. P. Balthasar Mueller, Qian Wang, Guanghui Yuan, Nicholas Antoniou, Xiao-Cong Yuan, and Federico Capasso. Polarization-Controlled Tunable Directional Coupling of Surface Plasmon Polaritons. *Science*, 340(6130):331–334, April 2013.

[12] Nanfang Yu, Patrice Genevet, Mikhail A. Kats, Francesco Aieta, Jean-Philippe Tetienne, Federico Capasso, and Zeno Gaburro. Light Propagation with Phase Discontinuities: Generalized Laws of Reflection and Refraction. *Science*, 334(6054):333–337, October 2011.

[13] Feng Huang, Hanning Yang, Siren Li, Xiangqian Jiang, and Xiudong Sun. Tunable Unidirectional Coupling of Surface Plasmon Polaritons Utilizing a V-Shaped Slot Nanoantenna Column. *Plasmonics*, 10(6):1825–1831, June 2015.

[14] Amnon Yariv and Pochi Yeh. *Photonics: Optical Electronics in Modern Communications (The Oxford Series in Electrical and Computer Engineering)*. Oxford University Press, Inc., New York, NY, USA, 2006.

[15] Paul Liao. *Theory of Dielectric Optical Waveguides 2e*. Academic Press, December 2012.

[16] D. A. B. Miller. Rationale and challenges for optical interconnects to electronic chips. *Proc. IEEE*, 88(6):728–749, June 2000.

[17] Xingcun Colin Tong. Fundamentals and Design Guides for Optical Waveguides. In *Advanced Materials for Integrated Optical Waveguides*, number 46 in Springer Series in Advanced Microelectronics, pages 1–51. Springer International Publishing, 2014.

[18] Katsunari Okamoto. *Fundamentals of Optical Waveguides*. Academic Press, August 2010.

[19] S. E. Miller. Coupled Wave Theory and Waveguide Applications. *Bell Syst. Tech. J.*, 33(3):661–719, May 1954.

[20] P. K. Tien. Light Waves in Thin Films and Integrated Optics. *Appl. Opt.*, 10(11):2395, November 1971.

[21] R. Ulrich and R. Torge. Measurement of Thin Film Parameters with a Prism Coupler. *Appl. Opt.*, 12(12):2901, December 1973.

[22] P. K. Tien, R. J. Martin, S. L. Blank, S. H. Wemple, and L. J. Varnerin. Optical waveguides of single-crystal garnet films. *Appl. Phys. Lett.*, 21(5):207–209, September 1972.

[23] Y. C. Wu, C. Garapon, R. Bazzi, A. Pillonnet, O. Tillement, and J. Mugnier. Optical and fluorescent properties of Y2O3 sol–gel planar waveguides containing Tb3+ doped nanocrystals. *Appl. Phys. A*, 87(4):697–704, March 2007.

[24] Daniel W. Hewak and John W. Y. Lit. Generalized dispersion properties of a four-layer thin-film waveguide. *Appl. Opt.*, 26(5):833, March 1987.

[25] Douglas A. Christensen, Shellee Dyer, James N. Herron, and Vladimir Hlady. Comparison of robust coupling techniques for planar waveguide immunosensors. volume 1796, pages 20–25, 1993.

[26] William L. Barnes, Alain Dereux, and Thomas W. Ebbesen. Surface plasmon subwavelength optics. *Nature*, 424(6950):824–830, 2003.

[27] Thomas W. Ebbesen, Cyriaque Genet, and Sergey I. Bozhevolnyi. Surface-plasmon circuitry. *Phys. Today*, 61(5):44, 2008.

[28] J. C. Maxwell Garnett. Colours in Metal Glasses and in Metallic Films. [Abstract]. *Proceedings of the Royal Society of London*, 73:443–445, 1904.

[29] R. W. Wood. On a Remarkable Case of Uneven Distribution of Light in a Diffraction Grating Spectrum. *Proc. Phys. Soc. London*, 18(1):269, 1902.

[30] R. W. Wood. XXVII. Diffraction gratings with controlled groove form and abnormal distribution of intensity. *Philos. Mag. Ser. 6*, 23(134):310–317, February 1912.

[31] Lord Rayleigh. On the Dynamical Theory of Gratings. *Proceedings of the Royal Society of London. Series A, Containing Papers of a Mathematical and Physical Character*, 79(532):399–416, 1907.

[32] U. Fano. The Theory of Anomalous Diffraction Gratings and of Quasi-Stationary Waves on Metallic Surfaces (Sommerfeld's Waves). *J. Opt. Soc. Am.*, 31(3):213, March 1941.

[33] Gustav Mie. Beiträge zur Optik trüber Medien, speziell kolloidaler Metallösungen. *Ann. Phys.*, 330(3):377–445, January 1908.

[34] R. H. Ritchie. Plasma Losses by Fast Electrons in Thin Films. *Phys. Rev.*, 106(5):874–881, June 1957.

[35] David Pines and David Bohm. A Collective Description of Electron Interactions: II. Collective vs Individual Particle Aspects of the Interactions. *Phys. Rev.*, 85(2):338–353, January 1952.

[36] J. J. Hopfield. Theory of the Contribution of Excitons to the Complex Dielectric Constant of Crystals. *Phys. Rev.*, 112(5):1555–1567, December 1958.

[37] Andreas Otto. Excitation of nonradiative surface plasma waves in silver by the method of frustrated total reflection. *Z. Physik*, 216(4):398–410, August 1968.

[38] E. Kretschmann and H. Raether. Notizen: Radiative Decay of Non Radiative Surface Plasmons Excited by Light. *Z. Für Naturforschung A*, 23(12):2135–2136, 1968.

[39] M. Fleischmann, P. J. Hendra, and A. J. McQuillan. Raman spectra of pyridine adsorbed at a silver electrode. *Chemical Physics Letters*, 26(2):163–166, May 1974.

[40] Alan Campion and Patanjali Kambhampati. Surface-enhanced Raman scattering. *Chem. Soc. Rev.*, 27(4):241, 1998.

[41] Junichi Takahara, Suguru Yamagishi, Hiroaki Taki, Akihiro Morimoto, and Tetsuro Kobayashi. Guiding of a one-dimensional optical beam with nanometer diameter. *Opt. Lett.*, 22(7):475, April 1997.

[42] T. W. Ebbesen, H. J. Lezec, H. F. Ghaemi, T. Thio, and P. A. Wolff. Extraordinary optical transmission through sub-wavelength hole arrays. *Nature*, 391(6668):667–669, February 1998.

[43] Edward S. Barnard, Justin S. White, Anu Chandran, and Mark L. Brongersma. Spectral properties of plasmonic resonator antennas. *Opt. Express*, 16(21):16529, October 2008.

[44] Yun-Feng Xiao, Yong-Chun Liu, Bei-Bei Li, You-Ling Chen, Yan Li, and Qihuang Gong. Strongly enhanced light-matter interaction in a hybrid photonic-plasmonic resonator. *Phys. Rev. A*, 85(3):031805, March 2012.

[45] Robert W. Boyd. *Nonlinear Optics*. Academic Press, January 2003.

[46] Lukas Novotny and Bert Hecht. *Principles of Nano-Optics*. Cambridge University Press, September 2012.

[47] P. B. Johnson and R. W. Christy. Optical Constants of the Noble Metals. *Phys. Rev. B*, 6(12):4370–4379, December 1972.

[48] P. G. Etchegoin, E. C. Le Ru, and M. Meyer. An analytic model for the optical properties of gold. *J. Chem. Phys.*, 125(16):164705, October 2006.

[49] N. F. Mott. The Basis of the Electron Theory of Metals, with Special Reference to the Transition Metals. *Proc. Phys. Soc. A*, 62(7):416, 1949.

[50] D. G. Pettifor. Theory of energy bands and related properties of 4d transition metals. I. Band parameters and their volume dependence. *J. Phys. F: Met. Phys.*, 7(4):613, 1977.

[51] F. Bassani. OPTICAL TRANSITIONS IN SOLIDS. 1975.

[52] Heinz Raether. *Surface Plasmons on Smooth and Rough Surfaces and on Gratings*, volume 111 of *Springer Tracts in Modern Physics*. Springer Berlin Heidelberg, 1988.

[53] O. Marti, H. Bielefeldt, B. Hecht, S. Herminghaus, P. Leiderer, and J. Mlynek. Near-field optical measurement of the surface plasmon field. *Optics Communications*, 96(4):225–228, February 1993.

[54] Jung-Hoon Song, Tolga Atay, Sufei Shi, Hayato Urabe, and Arto V. Nurmikko. Large Enhancement of Fluorescence Efficiency from CdSe/ZnS Quantum Dots Induced by Resonant Coupling to Spatially Controlled Surface Plasmons. *Nano Lett.*, 5(8):1557–1561, August 2005.

[55] A. V. Akimov, A. Mukherjee, C. L. Yu, D. E. Chang, A. S. Zibrov, P. R. Hemmer, H. Park, and M. D. Lukin. Generation of single optical plasmons in metallic nanowires coupled to quantum dots. *Nature*, 450(7168):402–406, November 2007.

[56] Hong Wei, Daniel Ratchford, Xiaoqin (Elaine) Li, Hongxing Xu, and Chih-Kang Shih. Propagating Surface Plasmon Induced Photon Emission from Quantum Dots. *Nano Lett.*, 9(12):4168–4171, December 2009.

[57] Igor Aharonovich, Andrew D. Greentree, and Steven Prawer. Diamond photonics. *Nat Photon*, 5(7):397–405, July 2011.

[58] Andreas W. Schell, Günter Kewes, Tobias Hanke, Alfred Leitenstorfer, Rudolf Bratschitsch, Oliver Benson, and Thomas Aichele. Single defect centers in diamond nanocrystals as quantum probes for plasmonic nanostructures. *Opt. Express*, 19(8):7914, April 2011.

[59] Martin Berthel, Oriane Mollet, Géraldine Dantelle, Thierry Gacoin, Serge Huant, and Aurélien Drezet. Photophysics of single nitrogen-vacancy centers in diamond nanocrystals. *Phys. Rev. B*, 91(3):035308, January 2015.

[60] E. Hutter and J. H. Fendler. Exploitation of Localized Surface Plasmon Resonance. *Adv. Mater.*, 16(19):1685–1706, October 2004.

[61] Amanda J. Haes and Richard P. Van Duyne. A unified view of propagating and localized surface plasmon resonance biosensors. *Anal Bioanal Chem*, 379(7-8):920–930, July 2004.

[62] Eleonora Petryayeva and Ulrich J. Krull. Localized surface plasmon resonance: Nanostructures, bioassays and biosensing—A review. *Analytica Chimica Acta*, 706(1):8–24, November 2011.

[63] Erwin Kretschmann. Die Bestimmung optischer Konstanten von Metallen durch Anregung von Oberflächenplasmaschwingungen. *Z. Physik*, 241(4):313–324, August 1971.

[64] H. Ditlbacher, J. R. Krenn, N. Felidj, B. Lamprecht, G. Schider, M. Salerno, A. Leitner, and F. R. Aussenegg. Fluorescence imaging of surface plasmon fields. *Appl. Phys. Lett.*, 80(3):404–406, January 2002.

[65] Suntak Park, Gwansu Lee, Seok Ho Song, Cha Hwan Oh, and Pill Soo Kim. Resonant coupling of surface plasmons to radiation modes by use of dielectric gratings. *Opt. Lett.*, 28(20):1870, October 2003.

[66] R. B. Pettit, J. Silcox, and R. Vincent. Measurement of surface-plasmon dispersion in oxidized aluminum films. *Phys. Rev. B*, 11(8):3116–3123, April 1975.

[67] B. Hecht, H. Bielefeldt, L. Novotny, Y. Inouye, and D. W. Pohl. Local Excitation, Scattering, and Interference of Surface Plasmons. *Phys. Rev. Lett.*, 77(9):1889–1892, August 1996.

[68] Shuiyan Cao, Eric Le Moal, Elizabeth Boer-Duchemin, Gérald Dujardin, Aurélien Drezet, and Serge Huant. Cylindrical vector beams of light from an electrically excited plasmonic lens. *Appl. Phys. Lett.*, 105(11):111103, September 2014.

[69] H. J. Lezec, A. Degiron, E. Devaux, R. A. Linke, L. Martin-Moreno, F. J. Garcia-Vidal, and T. W. Ebbesen. Beaming Light from a Subwavelength Aperture. *Science*, 297(5582):820–822, August 2002.

[70] F. J. Garcia-Vidal, H. J. Lezec, T. W. Ebbesen, and L. Martin-Moreno. Multiple Paths to Enhance Optical Transmission through a Single Subwavelength Slit. *Phys. Rev. Lett.*, 90(21):213901, May 2003.

[71] L. Martin-Moreno, F. J. Garcia-Vidal, H. J. Lezec, A. Degiron, and T. W. Ebbesen. Theory of Highly Directional Emission from a Single Subwavelength Aperture Surrounded by Surface Corrugations. *Phys. Rev. Lett.*, 90(16):167401, April 2003.

[72] J. Bravo-Abad, L. Martin-Moreno, and F. J. Garcia-Vidal. Transmission properties of a single metallic slit: From the subwavelength regime to the geometrical-optics limit. *Phys. Rev. E*, 69(2):026601, February 2004.

[73] Tineke Thio, K. M. Pellerin, R. A. Linke, H. J. Lezec, and T. W. Ebbesen. Enhanced light transmission through a single subwavelength aperture. *Opt. Lett.*, 26(24):1972, December 2001.

[74] H. L. Offerhaus, B. van den Bergen, M. Escalante, F. B. Segerink, J. P. Korterik, and N. F. van Hulst. Creating Focused Plasmons by Noncollinear Phasematching on Functional Gratings. *Nano Lett.*, 5(11):2144–2148, November 2005.

[75] W. L. Barnes, T. W. Preist, S. C. Kitson, and J. R. Sambles. Physical origin of photonic energy gaps in the propagation of surface plasmons on gratings. *Phys. Rev. B*, 54(9):6227–6244, September 1996.

[76] F. Lopez-Tejeira, Sergio G. Rodrigo, L. Martin-Moreno, F. J. Garcia-Vidal, E. Devaux, T. W. Ebbesen, J. R. Krenn, I. P. Radko, S. I. Bozhevolnyi, M. U. Gonzalez, J. C. Weeber, and A. Dereux. Efficient unidirectional nanoslit couplers for surface plasmons. *Nat. Phys.*, 3(5):324–328, May 2007.

[77] A Drezet, A. L Stepanov, A Hohenau, B Steinberger, N Galler, H Ditlbacher, A Leitner, F. R Aussenegg, J. R Krenn, M. U Gonzalez, and J.-C Weeber. Surface plasmon interference fringes in back-reflection. *Europhys. Lett. EPL*, 74(4):693–698, May 2006.

[78] Aurelien Drezet, Daniel Koller, Andreas Hohenau, Alfred Leitner, Franz R. Aussenegg, and Joachim R. Krenn. Surface plasmon polariton microscope with parabolic reflectors. *Opt. Lett.*, 32(16):2414, August 2007.

[79] A. Drezet, A. Hohenau, J. R. Krenn, M. Brun, and S. Huant. Surface plasmon mediated near-field imaging and optical addressing in nanoscience. *Micron*, 38(4):427–437, June 2007.

[80] Alexandre Baron, Eloïse Devaux, Jean-Claude Rodier, Jean-Paul Hugonin, Emmanuel Rousseau, Cyriaque Genet, Thomas W. Ebbesen, and Philippe Lalanne. Compact Antenna for Efficient and Unidirectional Launching and Decoupling of Surface Plasmons. *Nano Lett.*, 11(10):4207–4212, October 2011.

[81] Francisco J. Rodríguez-Fortuno, Giuseppe Marino, Pavel Ginzburg, Daniel O'Connor, Alejandro Martínez, Gregory A. Wurtz, and Anatoly V. Zayats. Near-Field Interference for the Unidirectional Excitation of Electromagnetic Guided Modes. *Science*, 340(6130):328–330, April 2013.

[82] Yuri Gorodetski, Aurélien Drezet, Cyriaque Genet, and Thomas W. Ebbesen. Generating Far-Field Orbital Angular Momenta from Near-Field Optical Chirality. *Phys. Rev. Lett.*, 110(20):203906, May 2013.

[83] D. O'Connor, P. Ginzburg, F. J. Rodríguez-Fortuño, G. A. Wurtz, and A. V. Zayats. Spin–orbit coupling in surface plasmon scattering by nanostructures. *Nat Commun*, 5:5327, November 2014.

[84] K. Y. Bliokh, F. J. Rodríguez-Fortuño, F. Nori, and A. V. Zayats. Spin-orbit interactions of light. *Nat Photon*, 9(12):796–808, December 2015.

[85] C. Sayrin, C. Junge, R. Mitsch, B. Albrecht, D. O'Shea, P. Schneeweiss, J. Volz, and A. Rauschenbeutel. Optical diode based on the chirality of guided photons. *Phys. Rev. X*, 5(4), December 2015.

[86] Hannes Pichler, Tomás Ramos, Andrew J. Daley, and Peter Zoller. Quantum optics of chiral spin networks. *Phys. Rev. A*, 91(4):042116, April 2015.

[87] Ling Lu, John D. Joannopoulos, and Marin Soljačić. Topological photonics. *Nat Photon*, 8(11):821–829, November 2014.

[88] Maurizio Righini, Anna S. Zelenina, Christian Girard, and Romain Quidant. Parallel and selective trapping in a patterned plasmonic landscape. *Nat Phys*, 3(7):477–480, July 2007.

[89] Kai Wang, Ethan Schonbrun, Paul Steinvurzel, and Kenneth B. Crozier. Trapping and rotating nanoparticles using a plasmonic nano-tweezer with an integrated heat sink. *Nat Commun*, 2:469, September 2011.

[90] Akira Fujishima, Xintong Zhang, and Donald A. Tryk. TiO2 photocatalysis and related surface phenomena. *Surface Science Reports*, 63(12):515–582, December 2008.

[91] Ludvik Martinu and Daniel Poitras. Plasma deposition of optical films and coatings: A review. *J. Vac. Sci. Technol. A*, 18(6):2619–2645, November 2000.

[92] Bin Peng, Gert Jungmann, Claus Jäger, Dietrich Haarer, Hans-Werner Schmidt, and Mukundan Thelakkat. Systematic investigation of the role of compact TiO2 layer in solid state dye-sensitized TiO2 solar cells. *Coordination Chemistry Reviews*, 248(13–14):1479–1489, July 2004.

[93] J. D. B. Bradley, C. C. Evans, F. Parsy, K. C. Phillips, R. Senaratne, E. Marti, and E. Mazur. Low-loss TiO2 planar waveguides for nanophotonic applications. In *23rd Annual Meeting of the IEEE Photonics Society*, pages 313–314, 2010.

[94] Clément Bonnand. *Couplage fort entre plasmons de surface et excitons de semiconducteur organique*. PhD thesis, Université Claude Bernard - Lyon I, October 2006.

[95] Lin Yang, S. Scott Saavedra, Neal R. Armstrong, and John Hayes. Fabrication and Characterization of Low-Loss, Sol-Gel Planar Waveguides. *Anal. Chem.*, 66(8):1254–1263, April 1994.

[96] Larry L. Hench and Jon K. West. The sol-gel process. *Chem. Rev.*, 90(1):33–72, January 1990.

[97] C. Jeffrey Brinker and George W. Scherer. *Sol-Gel Science: The Physics and Chemistry of Sol-Gel Processing*. Academic Press, October 2013.

[98] A. Bahtat, M. Bouazaoui, M. Bahtat, C. Garapon, B. Jacquier, and J. Mugnier. Up-conversion fluorescence spectroscopy in Er3+: TiO2 planar waveguides prepared by a sol-gel process. *Journal of Non-Crystalline Solids*, 202(1):16–22, July 1996.

[99] Go Sakai, Naoki Matsunaga, Kengo Shimanoe, and Noboru Yamazoe. Theory of gas-diffusion controlled sensitivity for thin film semiconductor gas sensor. *Sensors and Actuators B: Chemical*, 80(2):125–131, November 2001.

[100] Philip W. Baumeister. *Optical Coating Technology*. SPIE, 1000 20th Street, Bellingham, WA 98227-0010 USA, April 2004.

[101] Sang-Hee Ko Park, Minki Ryu, Chi-Sun Hwang, Shinhyuk Yang, Chunwon Byun, Jeong-Ik Lee, Jaeheon Shin, Sung Min Yoon, Hye Yong Chu, Kyoung Ik Cho, Kimoon Lee, Min Suk Oh, and Seongil Im. 42.3: Transparent ZnO Thin Film Transistor for the Application of High Aperture Ratio Bottom Emission AM-OLED Display. *SID Symp. Dig. Tech. Pap.*, 39(1):629–632, May 2008.

[102] Hsiao-chu Tsai and D. B. Bogy. Characterization of diamondlike carbon films and their application as overcoats on thin-film media for magnetic recording. *J. Vac. Sci. Technol. A*, 5(6):3287–3312, November 1987.

[103] Kayano Sunada, Yoshihiko Kikuchi, Kazuhito Hashimoto, and Akira Fujishima. Bactericidal and Detoxification Effects of TiO2 Thin Film Photocatalysts. *Environ. Sci. Technol.*, 32(5):726–728, March 1998.

[104] C. Jeffrey Brinker. Dip Coating. In Theodor Schneller, Rainer Waser, Marija Kosec, and David Payne, editors, *Chemical Solution Deposition of Functional Oxide Thin Films*, pages 233–261. Springer Vienna, 2013.

[105] Mohammed Bahtat, Jacques Mugnier, Liren Lou, and Jean Serughetti. Planar TiO2 waveguides by the sol-gel process: The relationship of structure to properties. volume 1758, pages 173–183, 1992.

[106] J. Mugnier, B. Varrel, M. Bahtat, C. Bovier, and J. Serughetti. Effect of annealing temperature on TiO2 monolayer thin films as studied by waveguide raman spectroscopy and electron microscopy. *J Mater Sci Lett*, 11(12):875–877, January 1992.

[107] Michel Olivier and Jean-Claude Peuzin. Characterization of silicon layers via guided wave optics. *Appl. Phys. Lett.*, 32(6):386–388, March 1978.

[108] Emile Pelletier, F. Flory, and Y. Hu. Optical characterization of thin films by guided waves. *Appl. Opt.*, 28(14):2918, July 1989.

[109] Ralf Mollenhauer and Emile Pelletier. Etude de la propagation guidée dans les multicouches optiques : Mesures d'atténuation et localisation des pertes dans l'empilement = Guided light propagation in optical multilayers : Attenuation measurements and localization of losses in the stack. http://cat.inist.fr/?aModele=afficheN&cpsidt=159465, 1994.

[110] Yu-Chun Wu, Maricela Villanueva-Ibañez, Cécile Le Luyer, Jun Shen, and Jacques Mugnier. Application of multi-wavelength m-lines spectroscopy for optical analysis of sol-gel prepared waveguide thin films. In *SPIE*, volume 5946, pages 59461E–59461E–12, 2005.

[111] Meltem Sezen. Focused Ion Beams (FIB) — Novel Methodologies and Recent Applications for Multidisciplinary Sciences. In Milos Janecek and Robert Kral, editors, *Modern Electron Microscopy in Physical and Life Sciences*. InTech, February 2016.

[112] Cynthia A. Volkert and Andrew M. Minor. Focused ion beam microscopy and micromachining. *MRS Bull.*, 32(05):389–399, 2007.

[113] L. A. Giannuzzi and F. A. Stevie. A review of focused ion beam milling techniques for TEM specimen preparation. *Micron*, 30(3):197–204, June 1999.

[114] M. W Phaneuf. Applications of focused ion beam microscopy to materials science specimens. *Micron*, 30(3):277–288, June 1999.

[115] Ampere A. Tseng. Recent developments in micromilling using focused ion beam technology. *J. Micromech. Microeng.*, 14(4):R15, 2004.

[116] L. R. Harriott, A. Wagner, and F. Fritz. Integrated circuit repair using focused ion beam milling. *J. Vac. Sci. Technol. B*, 4(1):181–184, January 1986.

[117] John Melngailis. Focused ion beam technology and applications. *J. Vac. Sci. Technol. B*, 5(2):469–495, March 1987.

[118] Shinji Matsui, Takashi Kaito, Jun-ichi Fujita, Masanori Komuro, Kazuhiro Kanda, and Yuichi Haruyama. Three-dimensional nanostructure fabrication by focused-ion-beam chemical vapor deposition. *J. Vac. Sci. Technol. B*, 18(6):3181–3184, November 2000.

[119] R. L. Seliger, J. W. Ward, V. Wang, and R. L. Kubena. A high-intensity scanning ion probe with submicrometer spot size. *Appl. Phys. Lett.*, 34(5):310–312, March 1979.

[120] Steve Reyntjens and Robert Puers. A review of focused ion beam applications in microsystem technology. *J. Micromech. Microeng.*, 11(4):287, 2001.

[121] Adnan Latif. *Nanofabrication Using Focused Ion Beam*. PhD thesis, University of Cambridge, 2000.

[122] C. Vieu, F. Carcenac, A. Pépin, Y. Chen, M. Mejias, A. Lebib, L. Manin-Ferlazzo, L. Couraud, and H. Launois. Electron beam lithography: Resolution limits and applications. *Applied Surface Science*, 164(1–4):111–117, September 2000.

[123] P. Rai-Choudhury. *Handbook of Microlithography, Micromachining, and Microfabrication: Microlithography*. IET, January 1997.

[124] Joe Nabity, Lesely Anglin Compbell, Mo Zhu, and Weilie Zhou. E-beam Nanolithography Integrated with Scanning Electron Microscope. In Weilie Zhou and Zhong Lin Wang, editors, *Scanning Microscopy for Nanotechnology*, pages 120–151. Springer New York, 2006.

[125] Aline Cerf and Christophe Vieu. *Soft Lithography, a Tool to Address Single-Objects Investigations.* INTECH Open Access Publisher, 2010. OCLC: 884029513.

[126] D. L. Olynick, B. Cord, A. Schipotinin, D. F. Ogletree, and P. J. Schuck. Electron-beam exposure mechanisms in hydrogen silsesquioxane investigated by vibrational spectroscopy and in situ electron-beam-induced desorption. *J. Vac. Sci. Technol. B*, 28(3):581–587, May 2010.

[127] Martin Berthel. *Plasmonique classique et quantique sous pointe optique par microscopie en champ proche*. PhD thesis, Université Grenoble Alpes, March 2016.

[128] A. T. O'Neil, I. MacVicar, L. Allen, and M. J. Padgett. Intrinsic and Extrinsic Nature of the Orbital Angular Momentum of a Light Beam. *Phys. Rev. Lett.*, 88(5):053601, January 2002.

[129] M. Specht, J. D. Pedarnig, W. M. Heckl, and T. W. Hänsch. Scanning plasmon near-field microscope. *Phys. Rev. Lett.*, 68(4):476–479, January 1992.

[130] Alain Dereux, Christian Girard, and Jean-Claude Weeber. Theoretical principles of near-field optical microscopies and spectroscopies. *J. Chem. Phys.*, 112(18):7775–7789, May 2000.

[131] A. Drezet, Daniel Koller, Andreas Hohenau, Alfred Leitner, Franz R. Aussenegg, and Joachim R. Krenn. Plasmonic Crystal Demultiplexer and Multiports. *Nano Lett.*, 7(6):1697–1700, June 2007.

[132] M. Fujihira, H. Monobe, N. Yamamoto, H. Muramatsu, N. Chiba, K. Nakajima, and T. Ataka. Selected Papers from the 3rd International Conference on Near-Field Optics and Related TechniquesScanning near-field optical microscopy of fluorescent polystyrene spheres with a combined SNOM and AFM. *Ultramicroscopy*, 61(1):271–277, December 1995.

[133] P. Dawson, F. de Fornel, and J-P. Goudonnet. Imaging of surface plasmon propagation and edge interaction using a photon scanning tunneling microscope. *Phys. Rev. Lett.*, 72(18):2927–2930, May 1994.

[134] A. Drezet, A. Hohenau, D. Koller, A. Stepanov, H. Ditlbacher, B. Steinberger, F. R. Aussenegg, A. Leitner, and J. R. Krenn. Leakage radiation microscopy of surface plasmon polaritons. *Materials Science and Engineering: B*, 149(3):220–229, April 2008.

[135] Luis Grave de Peralta. Study of interference between surface plasmon polaritons by leakage radiation microscopy. *J. Opt. Soc. Am. B*, 27(8):1513, August 2010.

[136] J-Y Laluet, A Drezet, C Genet, and T W Ebbesen. Generation of surface plasmons at single subwavelength slits: From slit to ridge plasmon. *New J. Phys.*, 10(10):105014, October 2008.

[137] Aurélien Drezet and Cyriaque Genet. Imaging Surface Plasmons: From Leaky Waves to Far-Field Radiation. *Phys. Rev. Lett.*, 110(21):213901, May 2013.

[138] Min Hu, Carolina Novo, Alison Funston, Haining Wang, Hristina Staleva, Shengli Zou, Paul Mulvaney, Younan Xia, and Gregory V. Hartland. Dark-field microscopy studies of single metal nanoparticles: Understanding the factors that influence the linewidth of the localized surface plasmon resonance. *J. Mater. Chem.*, 18(17):1949, 2008.

[139] D. J. Norris and M. G. Bawendi. Measurement and assignment of the size-dependent optical spectrum in CdSe quantum dots. *Phys. Rev. B*, 53(24):16338–16346, June 1996.

[140] Samuel Aberra Guebrou. *Influence des plasmons de surface propagatifs sur la cohérence de systèmes optiques*. PhD thesis, Université Claude Bernard - Lyon I, November 2012.

[141] Xavier Brokmann. *Propriétés de Fluorescence de Nanocristaux de CdSe Individuels*. PhD thesis, Université Pierre et Marie Curie-Paris VI, 2004.

[142] Mohammadhassan Valadan. Revealing Biomolecules Dynamics by UV Ultrafast Spectroscopy. *PhD Thesis*, 2015.

[143] K. C. Benny Lee, J. Siegel, S. E. D. Webb, S. Lévêque-Fort, M. J. Cole, R. Jones, K. Dowling, M. J. Lever, and P. M. W. French. Application of the Stretched Exponential Function to Fluorescence Lifetime Imaging. *Biophysical Journal*, 81(3):1265–1274, September 2001.

[144] Olivier Labeau, Philippe Tamarat, and Brahim Lounis. Temperature Dependence of the Luminescence Lifetime of Single CdSe/Zns Quantum Dots. *Phys. Rev. Lett.*, 90(25):257404, June 2003.

[145] Grant R. Fowles. *Introduction to Modern Optics*. Courier Corporation, April 2012.

[146] Eugene Hecht. *Optics*. Addison-Wesley, 2002. Google-Books-ID: 7aG6QgAACAAJ.

[147] A. L. Bloom, W. E. Bell, and F. O. Lopez. Laser Spectroscopy of a Pulsed Mercury-Helium Discharge. *Phys. Rev.*, 135(3A):A578–A579, August 1964.

[148] H. Gordon Berry, G. Gabrielse, and A. E. Livingston. Measurement of the Stokes parameters of light. *Appl. Opt.*, 16(12):3200–3205, 1977.

[149] Quanbo Jiang, Aline Pham, Martin Berthel, Serge Huang, Joel Bellessa, Cyriaque Genet, and Aurelien Drezet. Directional and Singular Surface Plasmon Generation in Chiral and Achiral Nanostructures Demonstrated by Leakage Radiation Microscopy. *ACS Photonics*, 3(6):1116–1124, 2016.

[150] Martin Berthel, Quanbo Jiang, Camille Chartrand, Joel Bellessa, Serge Huant, Cyriaque Genet, and Aurélien Drezet. Coherence and aberration effects in surface plasmon polariton imaging. *Phys. Rev. E*, 92(3):033202, September 2015.

[151] Miles Padgett, Johannes Courtial, and Les Allen. Light's Orbital Angular Momentum. *Phys. Today*, January 2007.

[152] E. Lombard, A. Drezet, C. Genet, and T. W. Ebbesen. Polarization control of non-diffractive helical optical beams through subwavelength metallic apertures. *New J. Phys.*, 12(2):023027, 2010.

[153] Clara I. Osorio, Abbas Mohtashami, and A. Femius Koenderink. K-space polarimetry of bullseye plasmon antennas. *Sci. Rep.*, 5:9966, April 2015.

[154] Hwi Kim, Junghyun Park, Seong-Woo Cho, Seung-Yeol Lee, Minsu Kang, and Byoungho Lee. Synthesis and Dynamic Switching of Surface Plasmon Vortices with Plasmonic Vortex Lens. *Nano Lett.*, 10(2):529–536, February 2010.

[155] Yuanjie Yang, Yuan Dong, Chengliang Zhao, and Yangjian Cai. Generation and propagation of an anomalous vortex beam. *Opt. Lett.*, 38(24):5418, December 2013.

[156] Yuanjie Pang and Reuven Gordon. Optical Trapping of a Single Protein. *Nano Lett.*, 12(1):402–406, January 2012.

[157] Ming Liu, Thomas Zentgraf, Yongmin Liu, Guy Bartal, and Xiang Zhang. Light-driven nanoscale plasmonic motors. *Nat Nano*, 5(8):570–573, August 2010.

[158] T. Tamir. *Integrated Optics*. Springer Science & Business Media, December 2013.

[159] S. T. Peng, T. Tamir, and H. L. Bertoni. Theory of Periodic Dielect Waveguides. *IEEE Trans. Microw. Theory Tech.*, 23(1):123–133, January 1975.

[160] T. Suhara and H. Nishihara. Integrated optics components and devices using periodic structures. *IEEE J. Quantum Electron.*, 22(6):845–867, June 1986.

[161] H. Toda, M. Haruna, and H. Nishihara. Optical integrated circuit for a fiber laser doppler velocimeter. *J. Light. Technol.*, 5(7):901–905, July 1987.

[162] Amnon Yariv and Michiharu Nakamura. Periodic structures for integrated optics. *IEEE J. Quantum Electron.*, 13(4):233–253, April 1977.

[163] T. K. Gaylord and M. G. Moharam. Analysis and applications of optical diffraction by gratings. *Proc. IEEE*, 73(5):894–937, May 1985.

[164] Dirk Taillaert, Frederik Van Laere, Melanie Ayre, Wim Bogaerts, Dries Van Thourhout, Peter Bienstman, and Roel Baets. Grating Couplers for Coupling between Optical Fibers and Nanophotonic Waveguides. *Jpn. J. Appl. Phys.*, 45(8A):6071–6077, August 2006.

[165] Eui-Young Song, Hyeonsoo Park, Sang-Eun Mun, Hyounghan Kwon, and Byoungho Lee. Grating decoupler of channel plasmon polariton waveguide for optical intergrated circuit application. In *SPIE*, volume 9655, pages 965520–965520–4, 2015.

[166] Brent Fisher, Jean Michel Caruge, Don Zehnder, and Moungi Bawendi. Room-Temperature Ordered Photon Emission from Multiexciton States in Single CdSe Core-Shell Nanocrystals. *Phys. Rev. Lett.*, 94(8), March 2005.

[167] P. O. Anikeeva, C. F. Madigan, S. A. Coe-Sullivan, J. S. Steckel, M. G. Bawendi, and V. Bulović. Photoluminescence of CdSe/ZnS core/shell quantum dots enhanced by energy transfer from a phosphorescent donor. *Chemical Physics Letters*, 424(1–3):120–125, June 2006.

[168] P. Spinicelli, S. Buil, X. Quélin, B. Mahler, B. Dubertret, and J.-P. Hermier. Bright and Grey States in CdSe-CdS Nanocrystals Exhibiting Strongly Reduced Blinking. *Phys. Rev. Lett.*, 102(13):136801, March 2009.

[169] Christophe Galland, Yagnaseni Ghosh, Andrea Steinbrück, Jennifer A. Hollingsworth, Han Htoon, and Victor I. Klimov. Lifetime blinking in nonblinking nanocrystal quantum dots. *Nat Commun*, 3:908, June 2012.

[170] Riccardo Scott, Sebastian Kickhöfel, Oliver Schoeps, Artsiom Antanovich, Anatol Prudnikau, Andrey Chuvilin, Ulrike Woggon, Mikhail Artemyev, and Alexander W. Achtstein. Temperature dependent radiative and non-radiative recombination dynamics in CdSe-CdTe and CdTe-CdSe type II hetero nanoplatelets. *Phys Chem Chem Phys*, 18(4):3197–3203, January 2016.

[171] Patrick Rauter, Jiao Lin, Patrice Genevet, Suraj P. Khanna, Mohammad Lachab, A. Giles Davies, Edmund H. Linfield, and Federico Capasso. Electrically pumped semiconductor laser with monolithic control of circular polarization. *Proc. Natl. Acad. Sci. U.S.A.*, 111(52):E5623–5632, December 2014.

[172] Aurélien Cuche, Oriane Mollet, Aurélien Drezet, and Serge Huant. "Deterministic" Quantum Plasmonics. *Nano Lett.*, 10(11):4566–4570, November 2010.

Résumé

Le projet de thèse est divisé en deux parties. D'une part, la génération directionnelle et singulière de plasmons de surface (SPPs) par des ouvertures nanométriques a été réalisé et optimisé par le biais de microscopie de fuites radiatives (LRM). Nous démontrons expérimentalement qu'une structure plasmonique composée de nano-ouvertures en forme de T et Λ permet de contrôler le couplage unidirectionnel et radiales SPPs grâce au spin de la lumière incidente. Pour confirmer nos résultats expérimentaux, nous développons un modèle analytique qui décrit les coupleurs plasmoniques constitués de nano-ouvertures par représentation multidipolaire, permettant ainsi une explication théorique de la directionalité et de la formation de vortex plasmonique. L'optimisation des paramètres géométriques tels que l'angle au sommet des ouvertures en forme de Λ montre la possibilité de maximiser la directivité et le taux d'extinction à la fois pour le couplage directionnel et la génération des vortex dans le champ lointain. Par ailleurs, notre méthode basée sur la détection LRM, permet une analyse quantitative et est avérée être une technique de caractérisation sophistiquée pour cartographier le champ plasmonique. Il fournit également plusieurs nouvelles possibilités pour la focalisation de SPP contrôlée en polarisation.

D'autre part, le couplage spin-orbite de la lumière dans un guide et son effet réciproque sont réalisées et confirmées expérimentalement et théoriquement. Les coupleurs et découpleurs réseaux sur le guide d'ondes sont d'abord développés et étudiés. La sortie parfaite de la lumière confinée par le découpleur nous offre la possibilité de détecter les ondes guidées. La fluorescence des nanocristaux déposés sur la surface de l'échantillon montre une autre possibilité de visualiser directement la propagation de la lumière dans le guide d'onde. Le couplage directionnel contrôlé par spin est réalisé par des antennes en forme de Λ et est confirmé par des images en champ sombre avec des découpleurs et des images de fluorescence. En outre, l'effet réciproque est observé avec une imperfection de polarisation de sortie qui est expliqué théoriquement par le fait que les ordres de diffraction par les antennes en forme de Λ influent sur les états de polarisation finaux. Ainsi, l'effet réciproque est parfaitement réalisé par la sélection d'une région spécifique de diffraction dans le plan de Fourier. La caractérisation quantitative des interactions spin-orbite nous permet d'envisager le développement de nouveaux coupleurs directionnels dans le domaine de la nanophotonique tels que le traitement quantique de l'information.

Mots clés: Plasmon de surface, Microscope de fuites radiatives, Spin-orbite couplage directionnel, Singularité optique et vortex, Coupleurs du guide, L'effet réciproque du spin-orbite couplage, Nanophotonique.

Introduction

La lumière peut être couplée à des ondes électromagnétiques propagatives dans un guide d'onde diélectrique ou le long d'une interface métal-diélectrique. Les premières, appelées ondes guidées, sont connues comme ingrédients indispensables dans le développement de dispositifs optiques intégrés qui permettent à un signal optique de se propager avec une perte d'énergie minimale. Les deuxièmes, appelés Plasmon Polaritons de Surface (SPPs), sont considérés comme des oscillations collectives d'électrons à la surface des métaux qui peuvent confiner l'énergie lumineuse à l'échelle du nanomètres [1]. Les propriétés fortement confinées de ces deux ondes conduisent à de nombreuses avancées dans le contrôle de la lumière à l'échelle du nanomètre qui offrent un moyen prometteur pour le développement de dispositifs dans le domaine de la nanophotonique comme le traitement de l'information quantique [2], le piégeage optique [3] etc. .

Afin de réaliser le contrôle directionnel de la lumière à l'échelle du nanomètre, un grand nombre de structures plasmoniques sont largement proposées et démontrées telles que l'utilisation des antennes Yagi-Uda [4-7], l'éclairage à angle incliné de la fente [8], antennes en V [9], des rainures asymétriques [10], etc. Cependant, dans la plupart de ces méthodes, la direction de propagation est limitée par les structures ou les façons incidents. Ainsi, un dispositif accordable en direction est très demandé. Récemment, une série de structures plasmoniques contrôlées par le spin du photons, telles que des ouvertures de longueur nanométrique en forme de T [11], des fentes en forme de L [10] et des antennes à fente en forme de V [12, 13]. Plus précisément, la direction de propagation peut être commandée par la polarisation circulaire (le spin) de la lumière incidente. Mais la directionnalité n'est pas aussi élevée que nous l'espérons dans de nombreux cas, car le mécanisme concernant le couplage directionnel à base de spin reste encore peu clair.

Motivés par des questions fondamentales ainsi que par leurs potentiels allant des circuits photoniques intégrés à l'optique quantique, nous avons développé nos structures plasmoniques appelées coupleurs Λ pour les deux ondes confinées. Tout d'abord, le couplage directionnel contrôlé par spin a été étudié, y compris la génération directionnelle et radiale des SPPs. Deuxièmement, ces mêmes structures ont été appliquées sur le guide d'ondes afin de contrôler le sens de propagation de la lumière guidée. Pendant mon doctorat de 3 ans, j'ai travaillé à l'Institut Néel à Grenoble sur un projet portant sur la génération directionnelle et singulière des SPPs. Chaque année, j'ai passé trois à quatre mois à l'Institut Lumière Matière (ILM) à Lyon pour le projet sur le couplage directionnel de la lumière dans le guide d'onde.

Dans mon manuscrit, la présentation de mon étude est divisée en 5 chapitres comprenant une introduction générale sur toutes les fondamentaux en plasmoniques et guide ondes, une description de l'élaboration des échantillons, une présentation sur les systèmes d'imagerie pour l'expérience et deux chapitres sur l'explication et la discussion des résultats. Voici une brève introduction de chaque chapitre:

1. Considérations générales: Les connaissances de base sur le guide d'onde diélectrique et les SPPs sont présentées en profondeur dans ce chapitre. Les propriétés des guides d'ondes sont expliquées en optique géométrique et en onde. La compréhension des modes guidés et des techniques de couplage nous aide à concevoir nos structures de coupleurs. Par la suite, on présente d'autres ondes confinées, les SPPs. Les propriétés optiques des métaux nobles sont tout d'abord décrites comme les connaissances préliminaires pour les SPPs. On déduit la relation de dispersion des SPPs se propageant à l'interface métal-diélectrique, puis on résout les équations de Maxwell et les conditions aux limites pour deux milieux. Les propriétés des SPPs obtenues à partir de la relation de dispersion nous offrent plusieurs possibilités pour exciter et détecter les SPPs. Enfin, un état de l'arts sur le contrôle directionnel de la lumière est brièvement revu.

2. Préparation des échantillons: Les méthodes et les processus de fabrication des guides d'ondes et des nanostructures sont expliqués dans ce chapitre. La fabrication du guide d'ondes comporte trois étapes: le processus de sol-gel, le dépôt de couches minces et la caractérisation des guides d'ondes TiO_2. Nous montrons le processus optimal pour la préparation de la solution de TiO_2 et le dépôt de film mince qui est confirmé en caractérisant la qualité du guide d'onde. Ensuite, la nanofabrication des métaux est présentée par deux méthodes qui sont le faisceau d'ions focalisé (FIB) et la lithographie par faisceau d'électrons (EBL). Le FIB est idéal pour graver les nanostructures telles que fentes et rainures sur le film métallique, tandis que le EBL est un moyen précis pour le dépôt de métaux sur le substrat tels que des bandes et des crêtes. Ensuite, une galerie d'échantillons avec toutes les structures fabriquées pendant mon étude de doctorat est montrée à la fin et quelques résultats préliminaires sont mentionnés.

3. Systèmes d'imagerie: La microscopie de fuites radiatives (LRM), l'imagerie par champ sombre et par fluorescence et les méthodes d'analyse de polarisation sont décrites dans ce chapitre. En tant que méthode de champ lointain pour l'imagerie directe de la propagation des SPPs, le LRM est un outil puissant permettant une cartographie précise et une analyse quantitative. Le principe de la détection pour des SPPs sur le plan direct et le plan de Fourier

est expliqué et la configuration expérimentale est expliquée. Ensuite, le système d'imagerie de champ sombre est introduit pour observer le couplage directionnel de lumière dans le guide d'ondes en filtrant la lumière d'excitation incidente. En outre, l'imagerie par fluorescence sert de méthode efficace pour visualiser la propagation des modes guidés car les nanocristaux déposés sur la surface de l'échantillon peuvent être excités par les ondes confinées dans le guide d'ondes. Enfin, la génération et l'analyse de polarisation utilisées dans notre expérience sont expliquées.

4. Génération des SPPs directionnelle et singulière contrôlée par spin: Les résultats de la génération directionnelle et singulière des SPPs contrôlés par spin sont présentés dans ce chapitre. Tout d'abord, le couplage unidirectionnel latéral des SPPs dans un réseau d'ouvertures en forme de T et en forme de Λ est théoriquement simulé par un modèle multidipolaire et ensuite réalisé expérimentalement. Nous introduisons un paramètre appelé directivité pour quantifier la capacité de la directionalité. Par la suite, nous optimisons la directivité par le modèle théorique et les résultats expérimentaux confirment notre attente. Deuxièmement, le couplage directionnel radial des SPPs appelés génération singulière ou vortex des SPPs dans le cercle d'ouvertures en forme de T et en forme de Λ est étendu à l'étude. Les chiralités des structures sont classée en deux types qui sont structures de gauche et de droite. Ensuite, nous définissons un autre paramètre appelé taux d'extinction pour caractériser la capacité de la génération singulière des SPPs. Enfin, le modèle analytique précédent est adapté pour le cercle d'ouvertures, ce qui nous aide à soutenir les résultats expérimentaux et à optimiser le rapport d'extinction de la singularité des SPPs.

5. Système d'émetteurs, de nanostructures et de guides d'ondes: Dans ce chapitre, les systèmes de coupleur et découpleur du guide d'onde sont d'abord introduits et testés. Les réseaux de coupleur et découpleur sont prouvés pour convertir la lumière de l'espace libre en onde confinée ou inversement, qui est la première méthode pour détecter l'onde guidée. De plus, avec la méthode d'imagerie par fluorescence, la propagation des modes guidés peut être visualisée directement par le signal de fluorescence, ce qui nous fournit plus de détails pour l'analyse du couplage directionnel de la lumière dans le guide d'ondes. Deuxièmement, le couplage optique spin-orbite est démontré par les antennes en forme de Λ et mis en évidence par le champ sombre et l'imagerie par fluorescence. Troisièmement, l'effet réciproque du couplage spin-orbite est proposé et étudié expérimentalement et théoriquement. Enfin, l'effet réciproque est réalisé en filtrant la région spécifique sur le plan de Fourier.

Conclusion et perspective

Ce projet sur le contrôle directionnel de la lumière est associé à la recherche fondamentale et aux applications émergentes. Ainsi, l'expérience et les études théoriques sont toutes mises en œuvre au cours de cette études de 3 ans. Les connaissances de base sur les Plasmon Polaritons de Surface (SPPs) et les guides d'ondes diélectriques ont été bien comprises. Les méthodes de nanofabrication telles que le faisceaux d'ions focalisé (FIB), la lithographie par faisceaux d'électrons (EBL) et la préparation de guides d'ondes en couches minces ont été intensivement utilisées et plus de 15 lots d'échantillons ont été développés. En ce qui concerne l'installation expérimentale, la microscopie de fuites radiatives (LRM) a été construite pièce par pièce à l'Institut Néel à Grenoble et la microscopie de champ sombre a été modifiée et alignée sur la base du LRM à l'Institut Lumière Matière (ILM) à Lyon. Travaillé avec deux groupes permet de combiner les avantages de chaque laboratoire et d'obtenir les meilleurs résultats. Pour la conclusion sur les résultats expérimentaux et sur les résultats théoriques, nous parlons d'abord de la génération SPP directionnelle et singulière contrôlée par spin, puis du couplage spin-orbite et de son effet inversé sur le guide d'onde.

Au moyen de LRM, nos structures plasmoniques avec des ouvertures en forme de Λ sur le film d'or sont réalisées la propagation directionnelle des SPPs contrôlée par spin en observant dans le champ lointain. En outre, une comparaison entre la simulation et les données expérimentales montre que notre modèle théorique reproduit bien les résultats expérimentaux et permet une détermination précise des contributions des dipôles dans le champ rayonné des SPPs. Simultanément, la compréhension du mécanisme nous aide à unifier les autres structures plasmoniques telles que les ouvertures en forme de T. De plus, l'optimisation de la directivité basée sur le modèle analytique est réalisée expérimentalement. En outre, dans les cercles d'ouvertures en forme de Λ , la propagation radiale et la formation singulière des SPPs sont démontrées avec LRM. En sélectionnant les états de polarisation d'entrée et de sortie appropriés, nous mettons en correspondance la singularité des SPPs et des vortex de Bessel dans l'espace direct. Nous avons montré que la méthode de caractérisation LRM rend possible l 'analyse quantitative pour la tomographie en polarisation. Enfin, l'optimisation du rapport d'extinction est réalisée en modifiant l'angle d'apex des ouvertures en forme de Λ. Tous ces résultats constituent un moyen prometteur pour le développement de dispositifs dans le domaine de la nanophotonique, comme le traitement de l'information plasmonique, les pinces optiques [88], le piégeage des particules [89], etc.

En ce qui concerne le couplage directionnel de la lumière dans le guide d'ondes, nous avons également obtenu des résultats importants. Tout d'abord, nous signalons que le système à tri-coupleur fonctionne comme un bloc de faisceau pour rayonner toute la lumière confinée hors du guide d'ondes. En introduisant les nanocristaux, la propagation unidirectionnelle des ondes guidées est révélée sous imagerie de fluorescence. Ensuite, les antennes en forme de Λ en or déposées sur le guide d'onde nous aident à réaliser le couplage spin-orbite de la lumière en l'espace libre dans le guide d'ondes comme le couplage des SPPs. En outre, l'effet réciproque est observé et étudié en profondeur. L'imperfection de la polarisation de sortie est due à la présence des différents ordres de diffraction par les antennes. Ainsi, nous analysons les états de polarisation des différents ordres dans le plan de Fourier par les paramètres de Stokes. La polarisation linéaire se trouve dans l'ordre central de diffraction et deux états de polarisation circulaire opposés se situent de chaque côté. A l'aide des résultats expérimentaux et un modèle analytique, on obtient enfin la polarisation quasi-circulaire de sortie en sélectionnant la région attendue sur le plan de Fourier. Cet effet joue un rôle important dans le développement du dispositif optoélectronique pour distinguer la direction du signal dans le guide d'onde en analysant la polarisation de la lumière extraite. Toute l'investigation pour les guides d'ondes devrait avoir un impact dans le domaine émergent de l'optique intégrée, en particulier pour le traitement et l'analyse de l'information.

De plus, l'effet réciproque du couplage spin-orbite est appliqué au cas du découplage des SPPs en photons. Maintenant nous essayons de concevoir un nouveau dispositif pour enlever l'interférence de deux sources qui est appelé "la gomme des franges". Plus précisément, deux matrices constituées ouvertures en forme de Λ sont gravées sur le film d'or et une fente est placée au centre de deux matrices. Lorsqu'un laser éclaire la fente centrale, les SPPs seront excités et se propagent à la place d'ouvertures en forme de Λ de chaque côté. Comme les SPPs se propagent aux mêmes structures à partir de deux directions opposées, la lumière découplée doit avoir la polarisation opposée de chaque côté qui ne peut pas conduire aucune interférence. Ainsi, les franges de chaque ordre sur le plan de Fourier devraient disparaître. Si un émetteur quantique est introduit au centre de deux matrices des ouvertures en forme de Λ au lieu d'une fente, le dispositif sert de la gomme des franges quantique qui peut également éliminer l'interférence de deux plasmons uniques. Par conséquent, notre travail futur se concentrera sur les applications dans le domaine quantique utilisant des photons uniques couplés à l'optique de champ proche [172].